DELFT UNIVERSITY OF TECHNOLOGY

Microstructure for Mid-Infrared Spectroscopy for Biofuel Composition Measurement

Guanchu Wang

Microstructure for Mid-Infrared Spectroscopy for Biofuel Composition Measurement

By

Guanchu Wang

Student Number: 4522796

in partial fulfilment of the requirements for the degree of

Master of Science

in Microelectronics

at the Delft University of Technology,

to be defended publicly on Thursday March 29, 2018 at 11:00 AM.

Supervisor:	Dr. ir. R. F. Wolffenbuttel	
Thesis committee:	Dr. ir. A. Bossche,	TU Delft
	Dr. S. Vollebregt,	TU Delft
	Dr. M. Ghaderi,	TU Delft
	Dr. G. Pandraud,	TU Delft

This thesis is confidential and cannot be made public until March 31, 2019.

TU Delft

Abstract

Biofuel sensors for measuring the ethanol and gasoline concentrations in bio-ethanol blends, have been studied worldwide and currently used in engine management in FlexFuel cars fabricated by amongst others, Ford Motor Company. However, water that results from ethanol sugar cane is inevitably present in the ethanol blend and requires a sensor that is capable of measuring the full ternary ethanol/gasoline/water composition.

This thesis presents the design of biofuel sensors, which can be used for the determination of compositions of liquid mixtures of ethanol and water, combined with the UV sensor, the ternary concentration problem of ethanol, water and gasoline can be solved.

Firstly, the technical background, societal relevance and the purpose of this thesis are given. Subsequently, the spectrum analysis of the infrared range is analyzed, and the ranges of interests are found. As a next step, the technologies which can possibly be applied in our application are analyzed, after that the coupling methods are analyzed. Next, the physical model of the sensor structure is built up in two simulation softwares and it is simulated in detail. After the interpretation of design properties, the fabrication process is introduced in detail and followed by the fabrication results. Finally, measurement setups were built and used for validating the simulations and model and for drawing the final research conclusions.

Acknowledgements

I would like to express my gratitude Dr.ir. R. F. Wolffenbuttel, who introduced me to this project and helped me continuously. He taught me not only the knowledge and skills on sensor design but also the way of researching and solving problems. Also I would like to thank Dr. M. Ghaderi a lot for being my daily supervisor, he taught me every details about the simulation and have done a lot of fabrication for me. I would not have this project done without his help. Also I want to give my thanks to Dr. A. Pelin, she has given me a lot of useful suggestions and help on the measurements.

Moreover, I would like to thank Luke Middelburg for providing some background of this project; Yu Xin for the help on the theories and the measurements; Andre, Sten and Gregory for being my committee. In addition, I would to thank the guys in the master room on 15th floor for reducing my loneliness.

Moreover, I would like to thank my friends in Delft, especially Jiahan, Jinyi, Dezhi and Yang. Finally I would like thank to the many good people that I lucky enough to meet during the two years in Delft.

I would like to express my thanks to my parents, for the selfless and endless love and concern.

Guanchu Wang

Table of contents

Chapter 1. Introduction

This thesis presents the design and fabrication of a new type of optical biofuel sensors, which can be used for determining the concentrations of the biofuel mixture of water, etnanol and gasoline. In this work, a optical sensor which is using absorption spectroscopy in the mid-infrared by evanescent sensing is presented. There are already many researchers using evanescent sensing method to measure biomolecules and cell. And there are also some articles on measuring in gaseous atmosphere. However, most of the evanescent sensing articles are using fibers. This thesis is going to present an optical sensor based on a waveguide to use infrared light to sense the concentrations. Firstly, the absorption spectroscopy of water and ethanol are analyzed. Then some sensing methods are analyzed. After the sensing method is chosen, the final simulations and designs are done.

In this first chapter, the motivation for this thesis is given by stating the problems addressed in this thesis and is followed by the selection of optical domain which could be used to implement the measurement by light-absorption spectroscopy. Subsequently previous research on this topic is presented. Furthermore, some works of state-of-the-art are mentioned.

1.1 Motivation

Nowdays, global warming, also referred to climate change, is becoming a more and more serious problem for human beings. And global warming is the observed century-scale rise in the average temperature of the earth's climate system and its related effects. Mutiple lines of scientific evidence show that the climate system is warming [1]. Global warming is caused by human activities like burning fossil fuels, deforestation and farming. When we burn fossil fuels like coal, oil and gas to create electricity or power our cars, we release CO2 pollution into the atmosphere.

The exhaust emissions of cars and trucks are also playing a big role in discussions about the environment and energy consumption. The principal air-quality pollutant emissions from petrol, diesel, and alternative-fuel engines are carbon monoxide, oxides of nitrogen, un-burnt hydrocarbons and particulate matter. It is emissions of these pollutants that are regulated by the Euro emissions standards. Modern cars, if kept in good condition, produce only quite small quantities of the air quality pollutants, but the emissions from large numbers of cars add to a significant air quality problem.

Motor vehicles emit matter < 2.5μm in diameter ($PM_{2.5}$) , and as a result, PM2.5 concentrations tend to be elevated near busy streets. In an urban area, the use of fossil fuels has caused some environmental problems, and these problems has led to the bad effects on human health [2].

The usage of bio-fuels, fuels that are produced from bio mass, such as sugar cane or corn, is a very clean and sustainable solution for the issues just mentioned above. Nowadays, bio-fuels are widely used in the world. Bio-fuel can be used as a fuel for vehicles in its pure form, but it is usually used as a diesel additive to reduce levels of particulates, carbon monoxide, and hydrocarbons from diesel-

powered vehicles. Bio-fuel is produced from oils or fats using transesterification and is the most common one in Europe.

Bio-fuel, or ethanol from sustainable sources, is produced from bio-mass (organic matter). The two main types of crop used for this bio-mass are sugar cane and corn [3]. Ethanol production from sugar cane results in hydrous ethanol, also called wet-alcohol or AEHC. The wet-ethanol is only used in Brazil, mainly because of their enormous amount of sugar cane production. Apart from this wet-alcohol, also dry alcohol or EACA is used, which is dehydrated and contains maximally 0.7° INMP of water, which corresponds with a volume fraction of 99.7 ◦ GL [4]. This dry-ethanol is usually mixed in different ratio's with regular gasoline and the ethanol fraction is denoted with an E. Some common ratio's are for example E10, E22 and E85. E100 or pure (hydrous) ethanol is mainly used in Brazil, whereas E22 and E85 are more available in the US. E10 does not need sensors to detect the concentrations and now it is commonly used in Europe. The flex fuel cars need to be able to run on as well hydrous ethanol (Brazilian E100) as gasoline-ethanol mixtures where dry-ethanol is applied [5]. E85 fuel needs sensors to detect the concentrations, however, there is only one kind of capacitive probe sensor to detect. And this capacitive probe can only detect ethanol from gasoline but not water.

When adding ethanol to the gasoline, multiple benefitial results are caused such as less CO2 is emitted for the same amount of energy when using ethanol as combustible. In the mixture of bio-fuel, there are mainly three components: ethanol, water and gasoline. There is water existing because sometimes the dry ethanol will absorb some water from the environment, or the ethnaol itself has some water.

Water will also do harm to the engine, if there is a substantial amount of water in the engine, The engine would absolutely refuse to crank. Assuming the water is not enough to prohibit cranking, the fuel injectors would have problems injecting fuel and water at high pressures, due to the higher density of water. Presence of water would also inhibit combustion in the cylinders. This depends on the amount of water present. If the water content is high enough, it would be difficult to initiate combustion. The water present in the fuel+water mixture would also absorb a portion of the heat energy generated by the inhibited combustion, reducing the already low efficiency of the engine. The water would also cool the cylinder walls abnormally, causing non-uniform expansion.

A integratable sensor which can be put into the fuel tank to sense the composition of the fuel needs to be developed. This sensor is needed to monitor the concentration of water, ethnaol and gasoline in real-time. So this thesis is going to discuss about how to built a sensor like this.

1.2 Selection of the Domain

There were studies before this thesis. The first was done by Giuseppe Lacerenca who had investigated the feasibility of using optical spectroscopy or dielectric spectroscopy [6] in 2012. The feasibility of various domains: electrical domain, thermal domain, optical domain and density measurement and surface acoustic waves, are discussed and detailed researched by Luke [7]. The design of thermal domain sensor is finished by Bo Jiang who was in the same group with me.

Luke's work shows that from the final conclusion of the electrical domain it became clear that only one useful independent measurement parameter is delivered by optical domain. At this point a second independent measurement parameter is required. From the feasibility study two domains offer both good selectivity to one of the three components and interesting possibilities for implementation and integration in the final application. When looking at the selectivity aspect, water is dominating the permittivity in the electrical impedance behavior whereas gasoline is comparatively weak. In the thermal domain, water again has the largest values for thermal capacitance and conductance. Simultaneously, gasoline is dominating the absorption behavior in the UV range whereas water and ethanol do not contribute to the optical absorption in this range. So in the LF impedance domain water is the strongest component, but in the optical domain, gasoline seems to be the dominating one.

That is to say we have already found that in the UV range, gasoline is dominating. In order to solve the ternary mixture problem in optical domian, we still need another range to sense water or ethanol. We found that in the near-infrared and mid-infrared range, there are two small bands that water dominates and ethanol dominates accordingly. This thesis is going to use the newly found near-infrared and mid-infrared bands to detect water and ethanol from each other.

1.3 Commercially Available Capacitive Probe

Searching results show that theres is one kind of fuel composition sensor on the market. As shown in Figure 1.1, this product is used most frequently to measure the binary mixtures of gasoline and ethanol by measuring the capacitance at a fixed frequency, and then an electrical signal will be used to get the composition information.

Figure 1.1 Fuel composition (flex fuel) sensor for E85

However, the ternary mixture problem can not be solved by measuring the impedance of the mixture. Because water has a dielectric constant of 80, which is much higher than ethanol's 25 and gasoline's 2. Even though we know the concentration of water, we still can not measure the concentration of ethanol and gasoline precisely.

Currently, no commercial fuel sensor or sensor system is available that is capable to solve the ternary mixture problem. This thesis is focusing on the optical domain to solve this ternary mixture problem.

1.4 Thesis Outline

This thesis design of a sensor structure for infrared optical spectroscopy for measuring the ternsry mixtures.

Chapter 2 analyzes the infrared spectroscopy and the materials. And some major absorbance differences between ethanol and water are found, which could be used to distinguish water with ethanol. This chapter is the bands and materials selection and can be regarded as a feasibility analysis.

Chapter 3 is the optical absorption spectroscopy. In this chapter, three optical sensing methods are analyzed. And finally the waveguide structure is selected to be the design of this thesis. If the waveguide is chosen, then comes a question of how to guide the light. Then the coupling methods are analyzed.

Chapter 4 shows all the simulation results and all the decisions made after analyzing the simulation results. The simulation results include 2D and 3D simulations about the waveguide itself, and 3D simulations about the tapered coupler.

Chapter 5 is about the layout design and the fabrication.

Chapter 6 is the testing results and the analysis about the problems accured during the testing.

Chapter 7 gives the main conclusions of this thesis and the future works based on this thesis.

References

[1] E. K. W. Aikins, "Evidence of climate change (global warming) and temperature increases in Arctic areas," in *Proceedings of World Academy of Science, Engineering and Technology*, 2012, no. 72, p. 1609: Citeseer.

[2] D. L. Buckeridge, R. Glazier, B. J. Harvey, M. Escobar, C. Amrhein, and J. Frank, "Effect of motor vehicle emissions on respiratory health in an urban area," *Environmental health perspectives,* vol. 110, no. 3, p. 293, 2002.

[3] E. L. Keating, *Applied combustion*. CRC press, 2007.

[4] A. Q. DO BRASIL, "Agência Nacional do Petróleo, Gás Natural e Biocombustíveis," 2013.

[5] M. Balat and H. Balat, "Recent trends in global production and utilization of bio-ethanol fuel," *Applied energy,* vol. 86, no. 11, pp. 2273-2282, 2009.

[6] G. LACERENZA, "A feasibility study of a sensor system to detect the amount of water and ethanol in petrol," 2013.

[7] L. M. Middelburg, "Bio-Fuel Composition Sensing," MSc., EEMCS, TU Delft, Delft, NL, 2016.

Chapter 2. Bands and Material Choosing (Mid-Infrared Light)

This chapter is going to introduce how the bands of interests are selected after analysis.

2.1 Motivation of Optical Domain

From Luke's feasibility study, two domains offer both good selectivity to one of the three components and interesting possibilities for implementation and integration in the final application. When looking at the selectivity aspect, water is dominating the permittivity in the electrical impedance behavior whereas gasoline is comparatively weak. In the thermal domain, water again has the largest values for thermal capacitance and conductance. Simultaneously, it is found by Luke that gasoline is dominating the absorption behavior in the UV range whereas water and ethanol does not contribute to the optical absorption in this range, as shown in Figure 2.1[1].

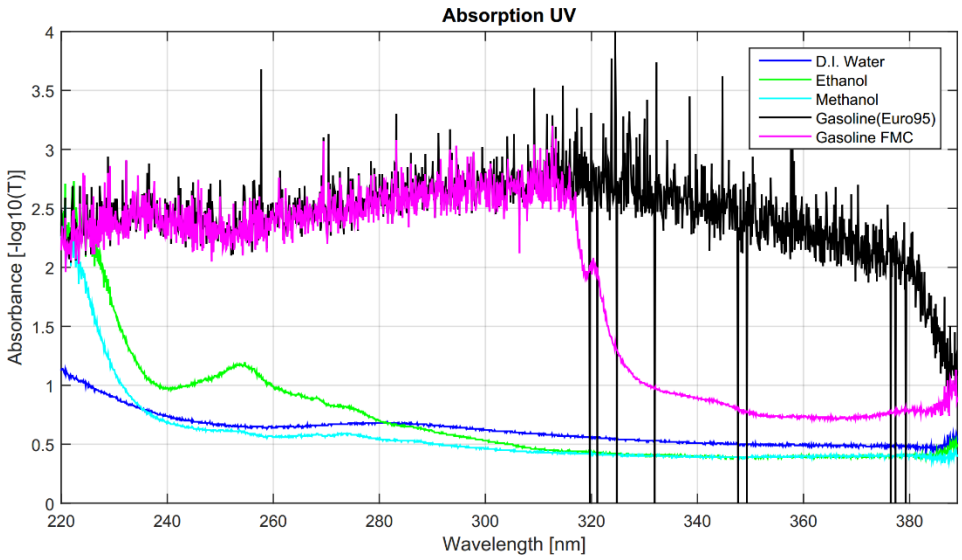

Figure 2.1 The measurement result of the flame Ocean Optics spectrometer [1]

The measured components are D.I. water, pure ethanol, pure methanol, regular Dutch gasoline Euro 95 and Regular American gasoline supplied by Ford Motor Company and therefore denoted as FMC in the figure. It can be clearly seen that the wavelength band around 400nm shows a high absorbance for gasoline, but for water and ethanol the absorbance is very low. That is to say this band can be used to distinguish gasoline from water and ethanol. However, another wavelength band is still needed to distinguish water from ethanol. This idea leads to the IR range.

2.2 Range of Interests

The IR spectra data of water and ethanol are obtained from NIST (National Institute of Standards and Technology[2]). The IR transmittance spectra is made from the data by MATLAB. Figure 2.2 [3, 4]

shows the transmittance of both water and ethanol in the IR range. The orange curve is for ethanol and the blue curve is for water.

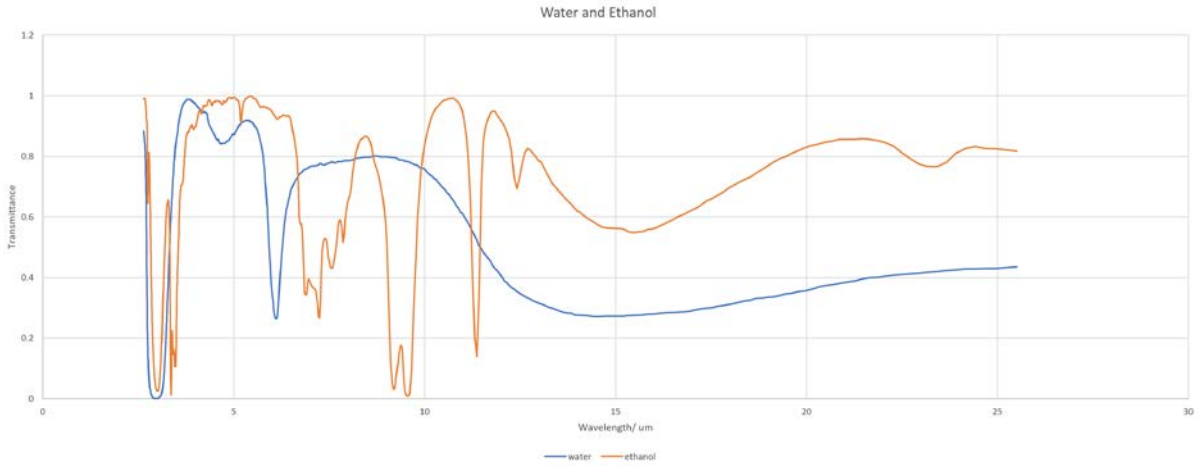

Figure 2.2 IR transmittance spectra of water and ethanol [3, 4]

This data used for making the figure is not the raw data of extinction coefficient. This data is measured by means of transmittance spectroscopy. Table 2.1 and Table 2.2 give the measurement information accordingly [3][4].

Table 2.1 Measurement information for water (transmittance spectroscopy) [3]

Owner	*COBLENTZ SOCIETY* *Collection (C) 2009 copyright by the U.S. Secretary of Commerce on behalf of the United States of America. All rights reserved.*
Origin	DOW CHEMICAL COMPANY
Source reference	COBLENTZ NO. 10116
Date	1969/10/21
State	LIQUID (NEAT)
Data processing	DIGITIZED BY NIST FROM HARD COPY (FROM TWO SEGMENTS)
Instrument	DOW KBr FOREPRISM-GRATING
Instrument parameters	BLAZED AT 3.5, 12.0, 20.0 MICRON, CHANGED AT 5.0, 7.5, 14.9 MICRON
Path length	CAPILLARY, AgCl PLATES
Resolution	4

Sampling procedure	TRANSMISSION

Table 2.2 Measurement information for water (transmittance spectroscopy) [4]

Owner	*COBLENTZ SOCIETY* *Collection (C) 2009 copyright by the U.S. Secretary of Commerce on behalf of the United States of America. All rights reserved.*
Origin	DOW CHEMICAL COMPANY
Source reference	COBLENTZ NO. 10139
Date	1965/10/13
State	SOLUTION (10% IN CCl4 FOR 3800-1340, 10% IN CS2 FOR 1340-400 CM-1)
Data processing	DIGITIZED BY NIST FROM HARD COPY (FROM TWO SEGMENTS)
Instrument	DOW KBr FOREPRISM-GRATING
Instrument parameters	BLAZED AT 3.5, 12.0, 20.0 MICRON, CHANGED AT 5.0, 7.5, 14.9 MICRON
Path length	0.011, 0.010 CM
Resolution	4
Sampling procedure	TRANSMISSION

The path-lengths of the measurements above are both 0.01mm.

From this data, Figure 2.3 shows a range of interests which does not reach the far-infared. Within this range, some ranges of interests are shown in Figure 2.4 to Figure 2.8. They are 1.8μm - 2.1μm, 2.6μm - 2.8μm, 3.25μm – 3.5μm, 3.5μm - 3.8μm and 4.5μm – 5μm accordingly.

the transmittance of water and ethanol shows great differences and this can be used to distinguish water from ethanol. Two seperated linear ranges: 2.6μm – 2.8μm and 3.5μm – 3.8μm, are selected here as targets. These two ranges will be used in the future work.

In range 2.6μm – 2.8μm, the transmittance of ethanol's is higher than water's, on the contrary, in the range of 3.5μm – 3.8μm, the transmittance of water's is higher than ethanol's. And also the trend of

the increasing or descreasing within these ranges are going to be linear. These properties are more than sufficient for measuring the concentrations of the the components.

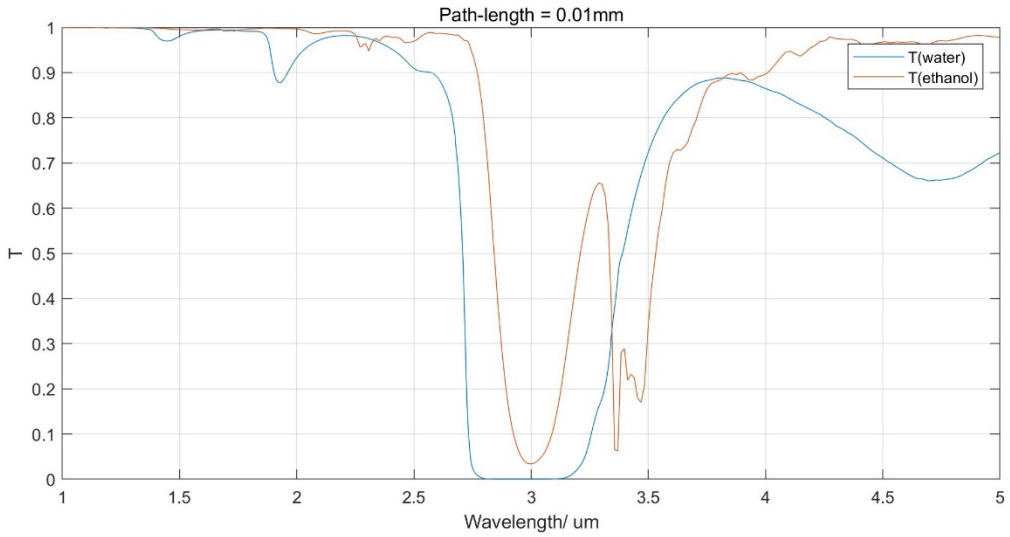

Figure 2.3 IR transmittance spectra of water and ethanol (1μm - 5μm)

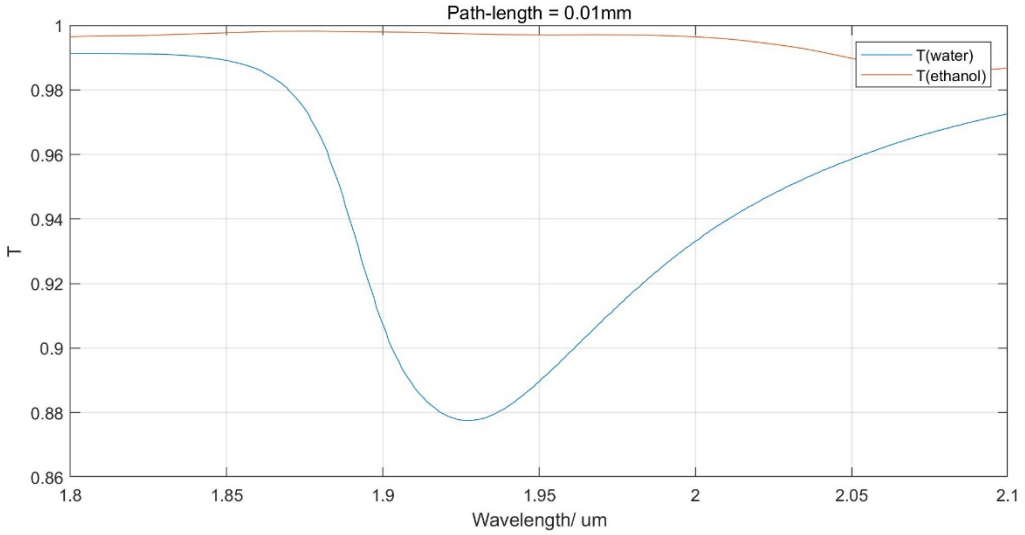

Figure 2.4 IR transmittance spectra of water and ethanol (1.8μm – 2.1μm)

Firstly, the range of 1.8μm – 2.1μm, this small peak of absoption is caused by the hydroxyl (-OH) of ethanol. Although this fact gives the chance to distinguish ethanol from water, the dynamic range of this peak is only about 10 pecent. Also from Luke's work we know that gasoline is going to absorb light during this range.

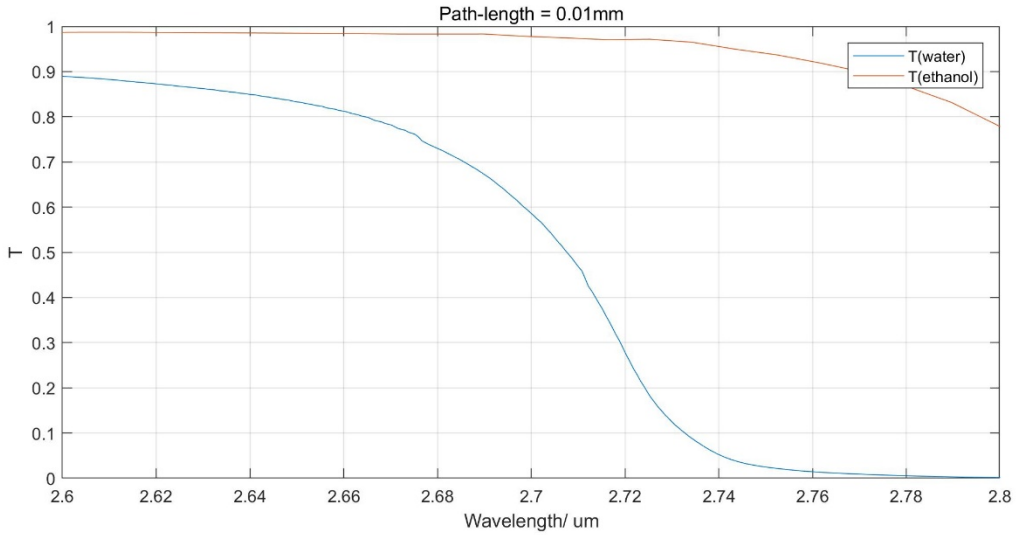

Figure 2.5 IR transmittance spectra of water and ethanol (2.6μm – 2.8μm)

In the range of 2.6μm – 2.8μm, water is dominating because water tends to absorb more light than ethanol. Also the dynamic range in this range is almost 90 percent. Furthermore, the curves for the mixtures must be between these two curves and almost linear. As a conclusion, this range is good to be used.

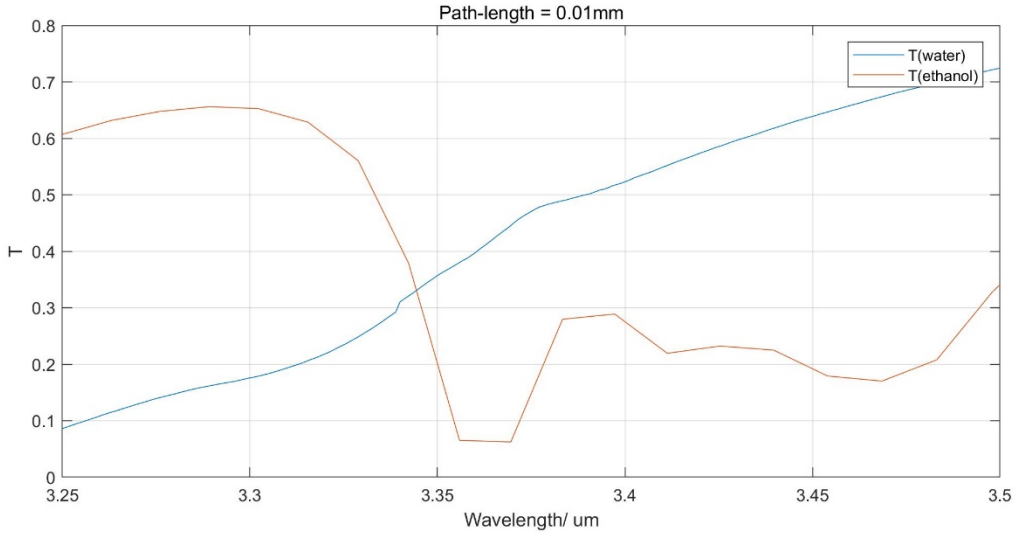

Figure 2.6 IR transmittance spectra of water and ethanol (3.25μm – 3.5μm)

In the range of 3.25μm – 3.5μm, there is a crossing between the two curves. What we want is a linear curve. So the crossing is unwanted. Furthermore, in this range both of water and ethanol dominate part of the range.

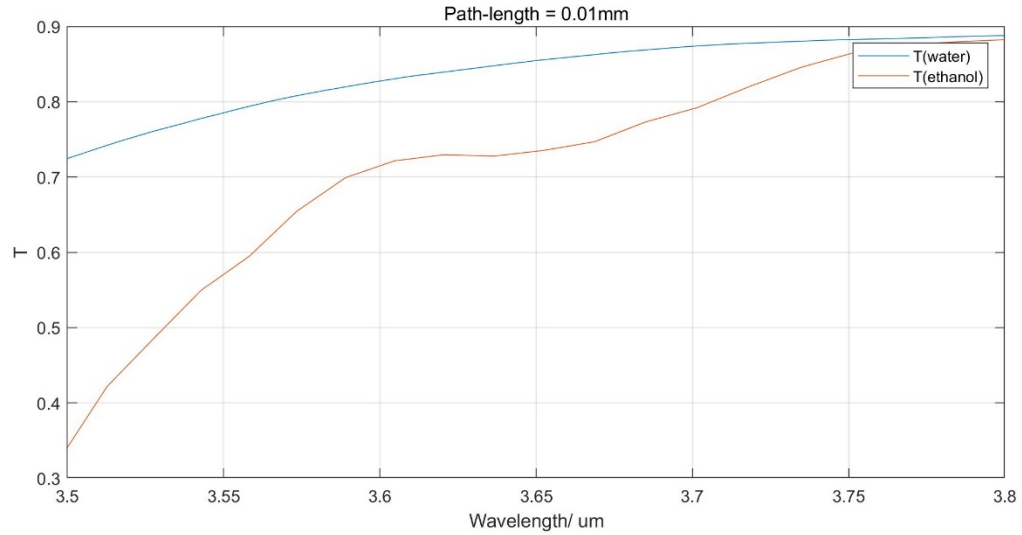

Figure 2.7 IR transmittance spectra of water and ethanol (3.5μm – 3.8μm)

This range of 3.5μm – 3.8μm is an ideal range because both curves are almost linear and the dynamic range is almost 60 percent. Also because the range is over 0.3μm of wavelength, that is to say there are more points can be used.

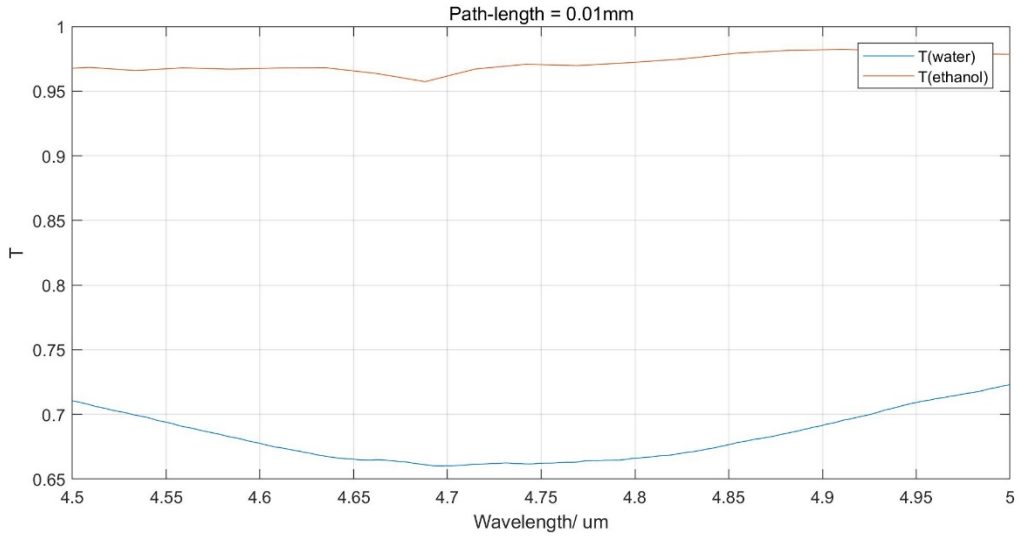

Figure 2.8 IR transmittance spectra of water and ethanol (4.5μm – 5μm)

This range of 4.5μm – 5μm contains the difference between water and ethanol, but there is no difference between the begin and the end of the range. So even though there is difference between the two curves, this range can not be used.

Table 2.3 Summary of the bands

Ranges (μm)	*Disadvantage*	*Feasibility*
1.8 – 2.1	Low Dynamic Range	No
2.6 – 2.8	No	Yes
3.25 – 3.5	Not Linear and Low Dynamic Range	No
3.5 – 3.8	No	Yes
4.5 – 5.0	Not linear and Low Dynamic range	No

Table 2.3 shows the summary of the band, only two ranges of interests can be used in our application: 2.6μm – 2.8μm and 3.5μm – 3.8μm. Range 2.6μm – 2.8μm is water dominating, and range3.5μm – 3.8μm is ethanol dominating. These two ranges are just good to use.

2.3 Material Selection

In chapter 3, it is detailed explained we have to choose a sensing technology of waveguide, and the material of the waveguide core has to be confirmed. This section is going to explain what material is the most suitable one for our application.

In our application, there are many materials which might be suitable for guiding the infrared light such as SiC, Si_3N_4, SiO_2 and poly-silicon.

Figure 2.9 is the refractive index and the extinction coefficient graph for silicon carbide. The refractive index is around 3 and it is very promising. However, from the raw data, the extinction coefficient is almost 0.01. In fact 0.01 is rather high for a waveguide. As a result, silicon carbide is not suitable for our case.

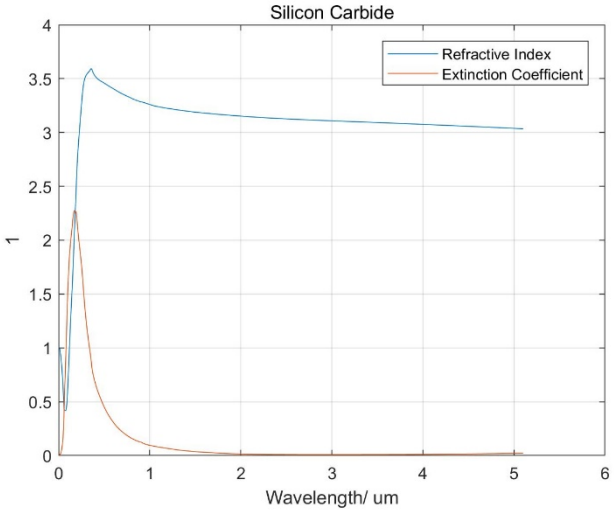

Figure 2.9 Refractive index and the extinction coefficient graph for silicon carbide

Silicon dioxide has a refractive index around 1.4 as shown in Figure 2.10. In our application, the sample's refractive index varies from 1.2 to 1.4. In order to make sure the light can propagate inside of the waveguide, silicon dioxide is abandoned.

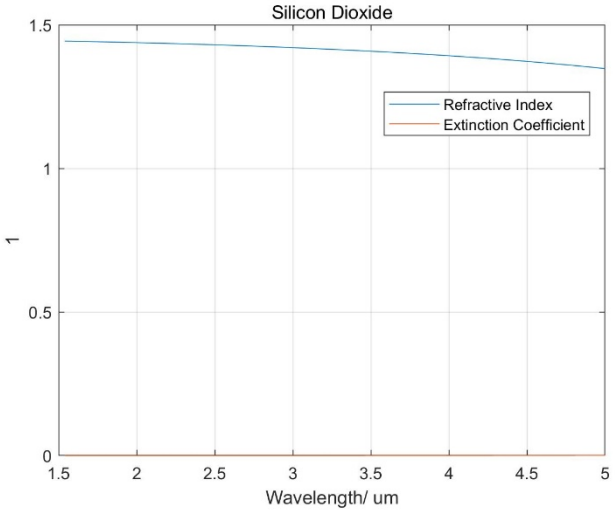

Figure 2.10 Refractive index and extinction coefficient for silicon dioxide

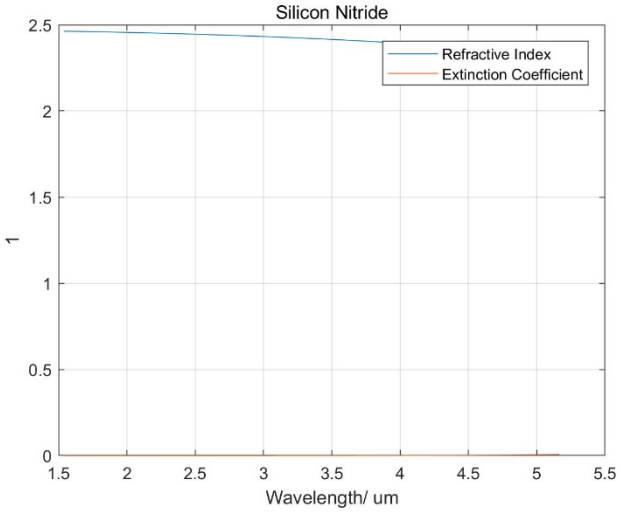

Figure 2.11 Refractive index and extinction coefficient for silicon nitride

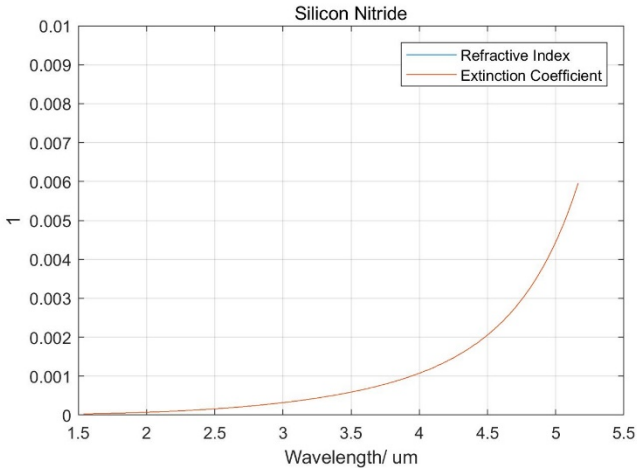

Figure 2.12 Extinction coefficient for silicon nitride

From the refractive index perspective, silicon nitride is a good material, as shown in Figure 2.11. However, the extinction coefficient in Figure 2.12 is around 0.001. As a matter of fact, 0.001 is high for a material to guide infrared light. Mention that 3.5μm to 3.8μm is the range of interests.

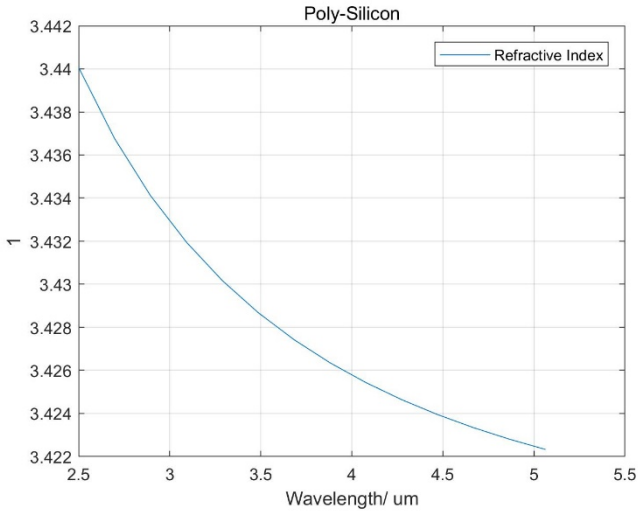

Figure 2.13 Refractive index for poly-silicon

Figure 2.13 shows the refractive index curve of poly-silicon. From this point of view, poly silicon is a good material to use. This material reminds us a special kind of sensor which is called silicon-on-oxide (SOI) structures. There are countless articles to talk about the design and the theory of SOI structures. Here it is not going to be explained.

However after an analysis among these materials. We decide to use poly-silicon on a layer of silicon dioxide.

2.4 Conclusion

From the raw data analysis, the ranges of interests and the material for the waveguide core are confirmed. The ranges are: 2.6μm – 2.8μm and 3.5μm – 3.8μm. Because these two ranges show a

linear property of absorbance. And the first range is water dominating and the second one is ethanol dominating, this property of difference increases the dynamic range.

And for the materials, the waveguide core material's refractive index should be higher than the cladding, and both the core material and the cladding material should be transparent to the wavelength range. Due to these restrictions, the suitable material for the waveguide core is poly-silicon, and for the cladding is silicon oxide.

References

[1] L. M. Middelburg *et al.*, "Optical Spectroscopy for Biofuel Composition Sensing," *Procedia Engineering,* vol. 168, no. Supplement C, pp. 55-58, 2016/01/01/ 2016.

[2] NIST. (2017). *Official Website*. Available: https://www.nist.gov/

[3] NIST Chemistry WebBook. (1969). *Water's Infrared Spectrum*. Available: http://webbook.nist.gov/cgi/cbook.cgi?ID=C7732185&Type=IR-SPEC&Index=1#IR-SPEC

[4] NIST Chemistry WebBook. (1965). *Ethanol's Infrared Spectrum*. Available: http://webbook.nist.gov/cgi/cbook.cgi?ID=C64175&Type=IR-SPEC&Index=3#IR-SPEC

Chapter 3. Optical Absorption Spectroscopy

This chapter is going to introduce the most often used optical technologies. These technologies are used to measure the concentrations of different components under different circumstances. At the end of this chapter why we have chosen that technology is going to be explained.

3.1 Technologies Analyses

In this section, four technologies are going to be analyzed including transmittance spectroscopy, total internal reflection (TIR) using wafer, fiber and structure of waveguide. They are going to be explained later in this chapter.

3.1.1 Transmittance Spectroscopy

Transmittance spectroscopy is used in many areas[1]. And especially the infrared light is often used in food analysis[2]. The principle is that the vibration of C-H, O-H and N-H chemical bonds. IR spectroscopy is used routinely for the compositional, functional and sensory analysis of food ingredients, process intermediates and final products. The major advantage of transmittance spectroscopy is that usually no sample preparation is necessary, hence the analysis is very simple and fast. These are also the advantages of every optical method.

The major disvantage is that transmittance spectroscopy needs a sample container to make light go throught it, which means a cuvette is needed. The light path-length of a cuvette is the distance between the interior walls of a cuvette where the light goes through. On a standard spectrophotometer cuvette, the light path or path length will be the inner distance from the front window to the back window.

Using the method of transmittance spectroscopy means that we need to fill the sample into the small cuvette. The schematic of some standard cuvettes is shown in Figure 3.1.

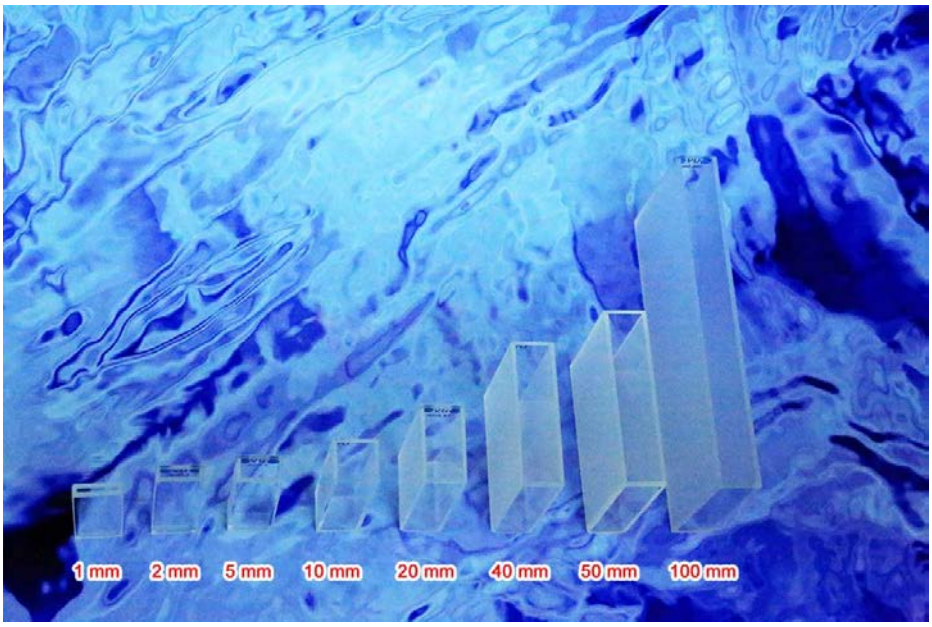

Figure 3.1 Basic cuvettes that path-length varies from 1mm to 100mm[3]

As discussed in last section the ranges of interests were found. However, the path-length the authors used is 0.01mm which is extremely short. So a reliable database needs to be found.

Based on the equation of Beer Lambert Law [4]:

$$\mathrm{T} = \mathrm{e}^{-\alpha \mathrm{L}}, \alpha = \frac{4\pi k}{\lambda}$$

The absorbance (α) and the extinction coefficient (k) present the absorption property of the liquid itself. In the Beer Lambert equation, T is the transmittance which we want to calculate, α is the absorbance under certain wavelength, L is the path-length of a transmittance spectroscopy, and k is the extinction coefficient, and λ is light's wavelength.

In this thesis, all the simulation and analysis are based on the the absorbance data (α) of water is given by Wieliczka, Weng & Querry in 1989 [5] and the extinction coefficient data (k) of ethanol is given by Sani and Dell'Oro in 2016 [6].

The absorbances water and ethanol are calculated and shown in Figure 3.2. And then the transmittances under a path-length of 0.01mm of water and ethanol are calculated and shown in Figure 3.3. The range of interests is zoomed in and shown in Figure 3.4.

Figure 3.4 shows that if we make the path-length as short as 0.01mm, we can get the similar result as [7, 8]. But in practical situation, 0.01 mm path-length is hard to achieve. However, an 1mm-path-length cuvette is the smallest cuvette in the current lab.

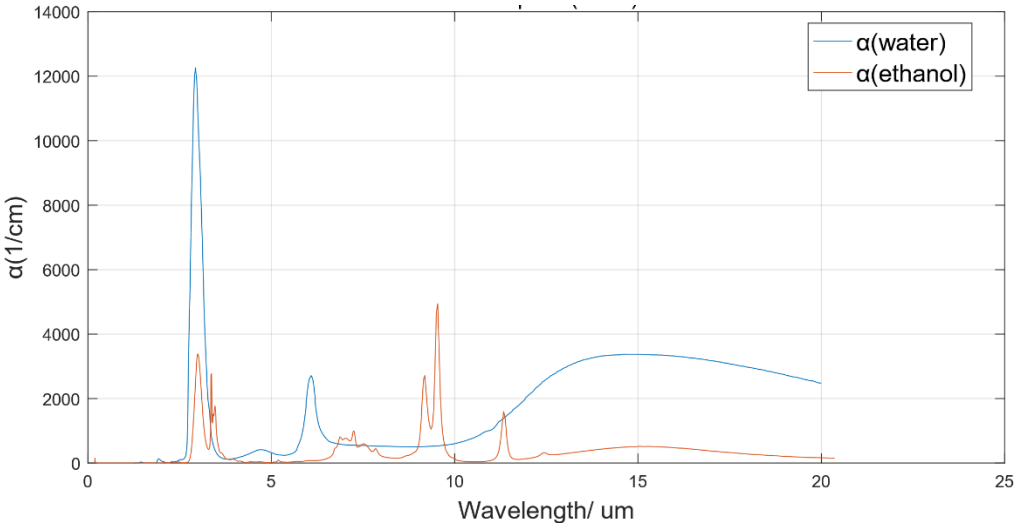

Figure 3.2 Absorbance of Water and Ethanol

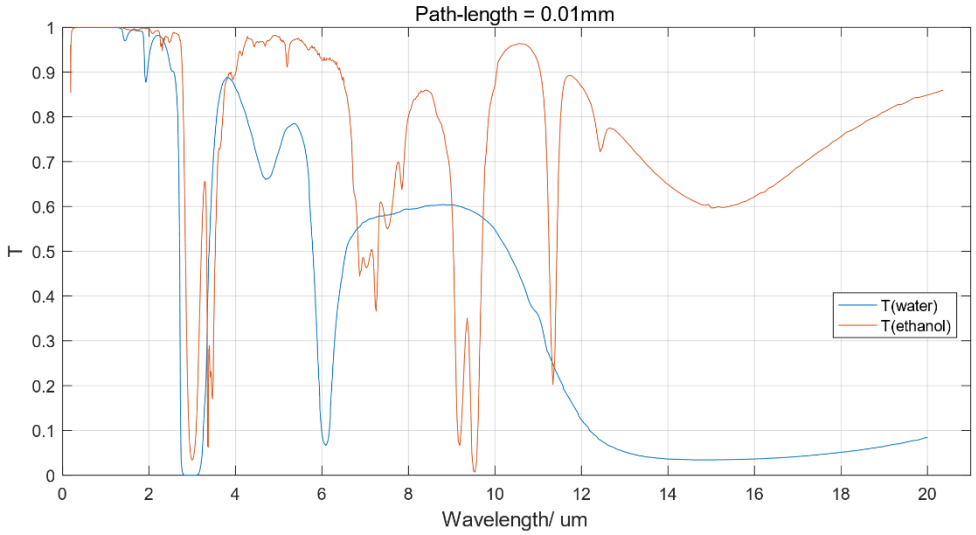

Figure 3.3 IR transmittance spectra of water and ethanol

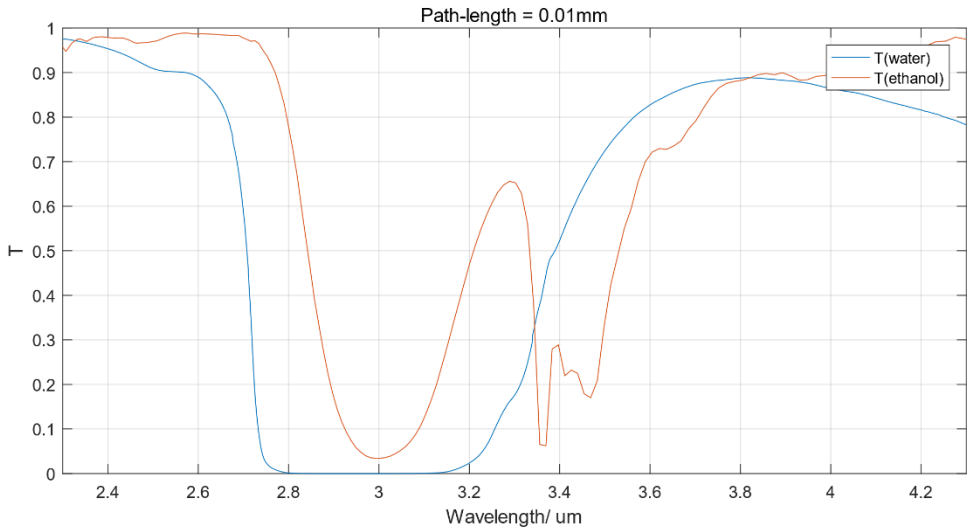

Figure 3.4 IR transmittance spectra of water and ethanol (2.3μm - 4.3μm)

After this, Pelin who is a post-doctor from our group used a 1mm path-length cuvette to do an experiment to test the tansmittance of water. The experimental transmittance data is compared with the original data in Figure 3.5 and Figure 3.6.

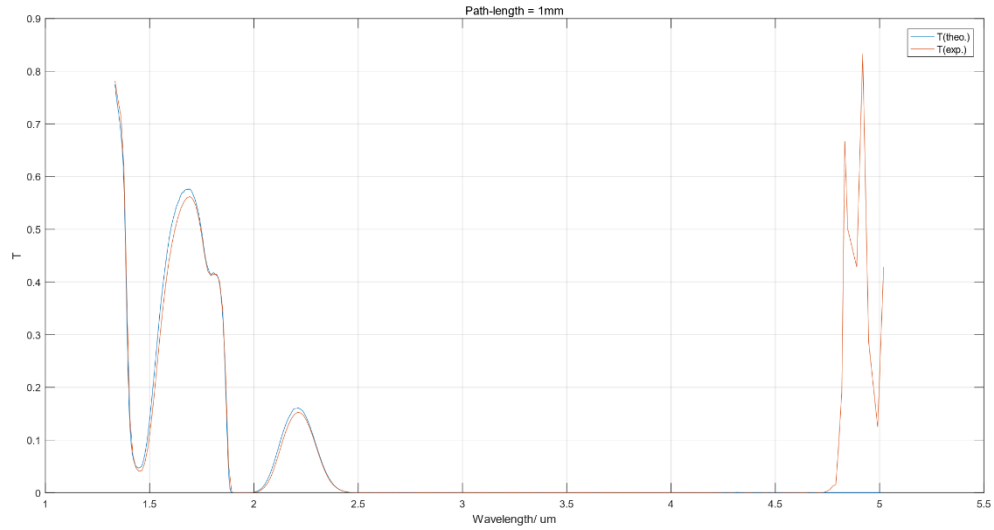

Figure 3.5 Experimental data compared with the theoretical data in 1mm path-length

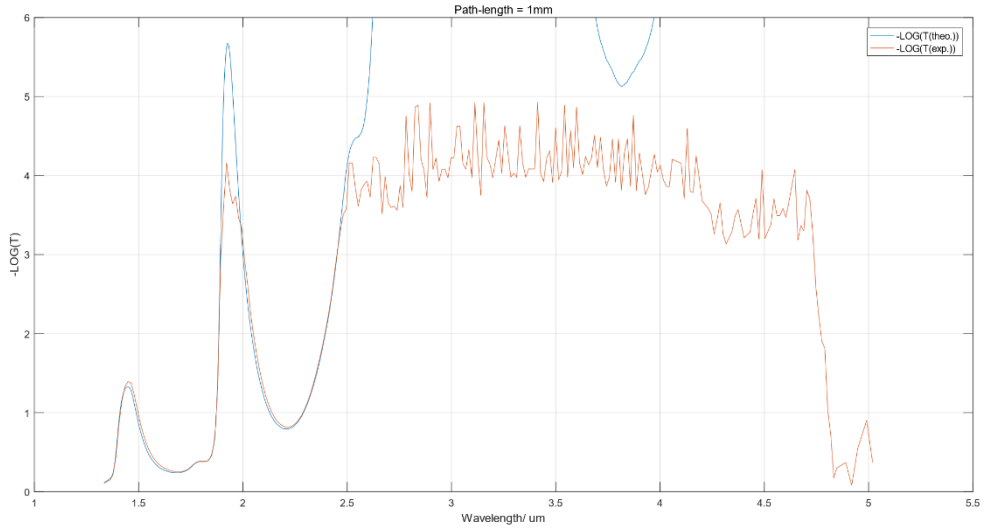

Figure 3.6 Experimental data compared with the theoretical data in 1mm path-length (logarithmic)

The transmittance data in Figure 3.5 seems promising because the experimental data and the theoretical data look almost the same. But when it goes to the logarithmic view, a major distortion happens when the transmittance data is below 10^{-3} scale. That is due to the very high absorption rate of water.

A conclusion is drawn that transmittance spectroscopy would not be helpful in this application if the path-length is 1mm. So another method has to be found. Next chapter will explain Total Internal Reflection.

3.1.2 Total Internal Reflection

The basic schematic of total internal reflection is shown in Figure 3.7 [9]. When the medium's refractive index n_1 is greater than n_2, and the incident angle is greater than the critical angle:

$$\theta_c = \sin^{-1}\frac{n_2}{n_1} \dots [9]$$

Then the light will be totally reflected. However, light has wave–particle duality, and has a wave nature (and vice versa) [10]. Maxwell derived a wave form of the electric and magnetic equations, thus uncovering the wave-like nature of electric and magnetic fields and their symmetry. Because the speed of EM waves predicted by the wave equation coincided with the measured speed of light, Maxwell concluded that light itself is an electromagnetic(EM) wave [11].

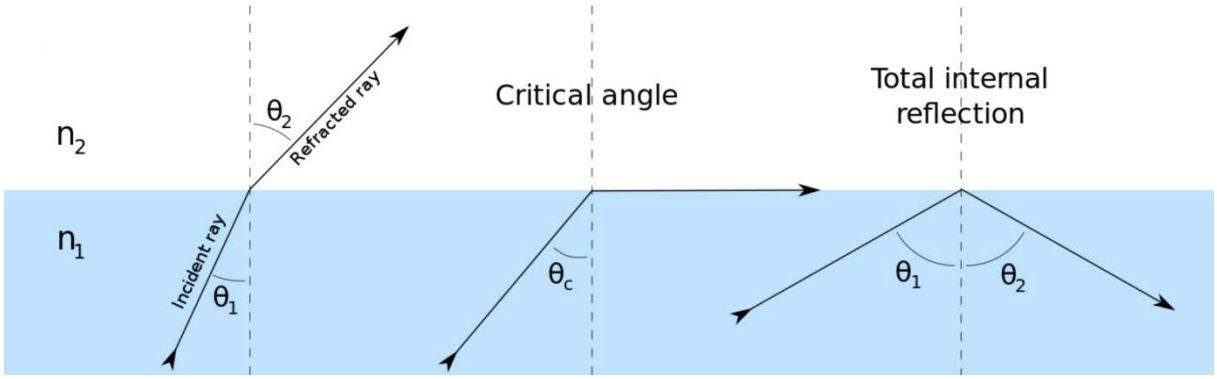

Figure 3.7 Total internal reflection [9]

The evanescent field is well known in optics since it is essential in the transmission light in various materials. The evanescent field can be calculated by solving Maxwell's equations at the boundary interface between two mediums. The decrease of the electric field in the rarer medium is exponentially and is given by:

$$\mathrm{E(y)} = E_0 e^{-y/d_p} \text{ with}$$

$$d_p = \frac{\lambda}{2\pi\sqrt{n_1^2 sin^2\theta - n_2^2}} \text{ ... [12]}$$

The factor d_p is called the penetration depth and depends on the wavelength, the incident angle θ and the refractive indices of the high-density medium n_1 and the lower density medium n_2. Figure 3.8 shows the penetration depth d_p.

Because water and ethanol have no magnetism, here only the electrical field will be concerned. By using this method of sensing the light need to be guided into a medium and in response to the targeted liquid via evanescent wave interactions [13]. Figure 3.9 is the schematic of evanescent sensing [12].

After a short research, it came up with only silicon will not absorb the light of the light in the range of interests. So in the rest of this thesis, the material has a higher refrative index will be silicon.

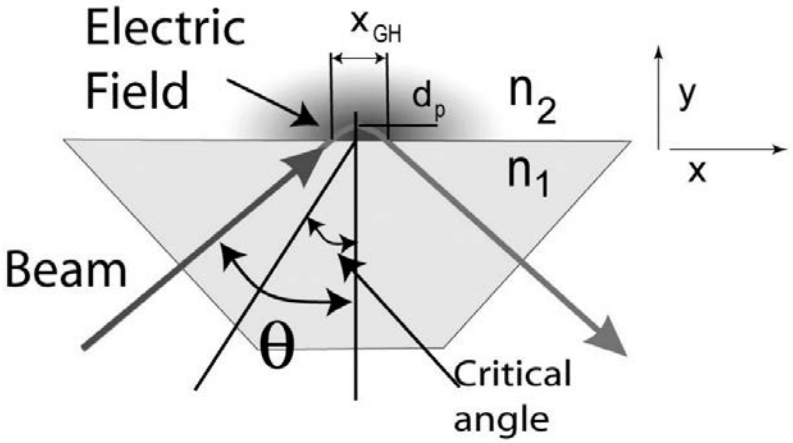

Figure 3.8 Total internal reflection and evanescent field [12]

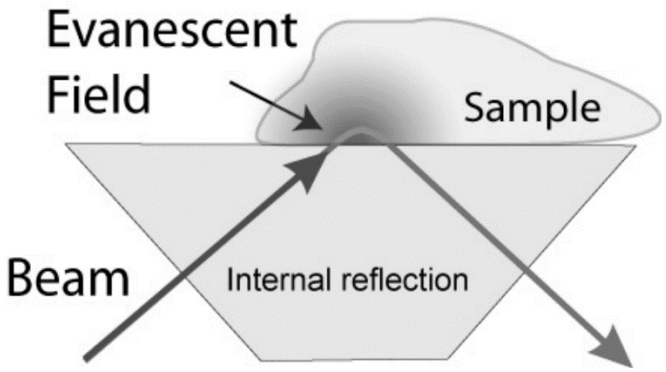

Figure 3.9 Schematic of evanescent sensing [12]

The sample is a mixture of water, ethanol and gasoline as discussed before. Known the database, the refractive index range of ethanol between the wavelengths of 2μm and 5μm is from 1.3 to 1.4 [6], for water it is from 1.15 to 1.5 [5]. And the refractive index of gasoline is around 1.55. The refractive index of silicon in room temperature can be obtained from [14].And the mixture's refractive index can be calculated as:

$$\mathrm{n} = \mathrm{a}_1 * \mathrm{n}_1 + \mathrm{a}_2 * \mathrm{n}_2 \ldots [15]$$

This equation is valid when two kinds of liquids with different refractive indexes of n_1 and n_2 are mixed, the refractive index of the mixture n has a relation with n_1 and n_2, a_1 and a_2 are the concentration percentages of the liquids.

After gaining these information, the penetration depth can be calculated. Because the highest refractive index of the liquid mixture is around 1.55. The critical angle of the incident light can be calculated as:

$$\theta = \sin^{-1} n_2/n_1 \geq \sin^{-1} 1.55/3.43$$

The incident angle has to be above 29 degrees to make sure the total internal reflection happens.

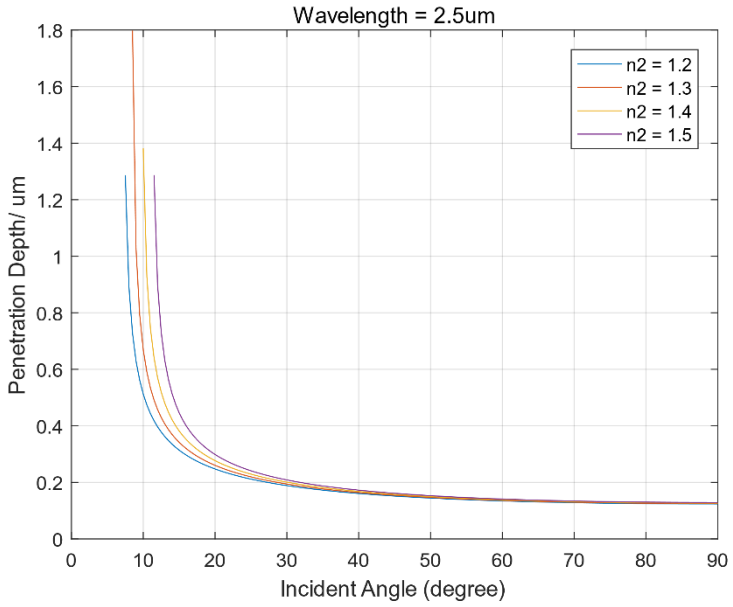

Figure 3.10 Penetration depth vs. incident angle (2.5μm wavelength)

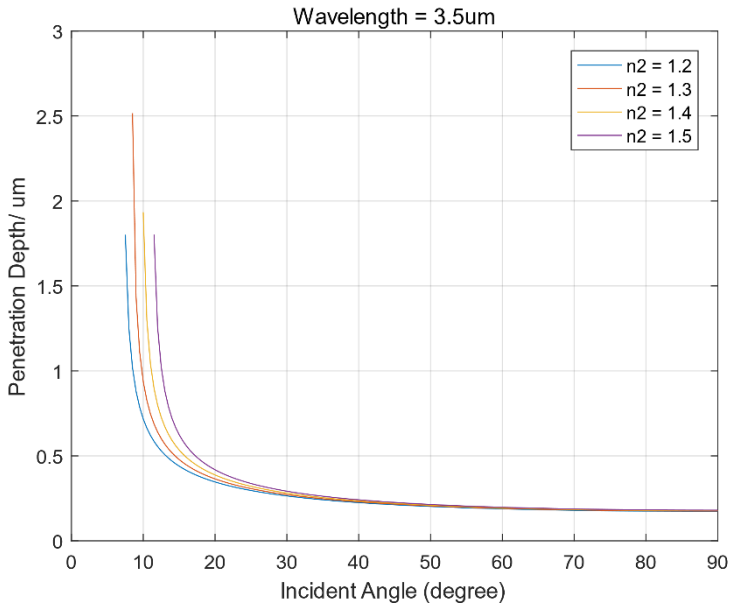

Figure 3.11 Penetration depth vs. incident angle (3.5μm wavelength)

Figure 3.10 and Figure 3.11 give the penetration depth and the incident angle information. When total internal reflection happens, the penetration depth is around 0.25μm. This information is very useful because it gives a view about how deep the effective area is, which will intereact with the sample.

The next step is to see how total internal reflection will work when the sample is added. The relation between the incident and reflected intensity R at a given wavelength depends on the refractive indices of both mediums, the incident angle of the light beam, and also on the polarization of the light, for parallel and perpendicular polarized light the attenuation can be calculated from the Fresnel equation:

$$R_{\parallel} = \left| \frac{n_1 \cos\theta_1 - \sqrt{(n_2 - ik_2)^2 - n_1^2 \sin^2\theta_1}}{n_1 \cos\theta_1 + \sqrt{(n_2 - ik_2)^2 - n_1^2 \sin^2\theta_1}} \right|^2$$

$$R_{\perp} = \left| \frac{(n_2 - ik_2)^2 \cos\theta_1 - n_1\sqrt{(n_2 - ik_2)^2 - n_1^2 \sin^2\theta_1}}{(n_2 - ik_2)^2 \cos\theta_1 + n_1\sqrt{(n_2 - ik_2)^2 - n_1^2 \sin^2\theta_1}} \right|^2$$

In these equations, θ is the incident angle, n_1 and n_2 are the real parts of the refractive index of the high and the lower density medium (sample) and k_2 is the complex part of the refractive index of the lower density medium (sample).

Based on the formulas above, the reflectance of both water and ethanol in the total internal reflection can be simulated. Notice that here only the reflectance figures for the wavelength range of interests will be shown because too many figures will make this section looks redundant. In Figure 3.12 and Figure 3.13, the plots of reflectance of TIR of parallel and perpendicular polarized light with an incident angle of 29 degrees for both ethanol and water are given.

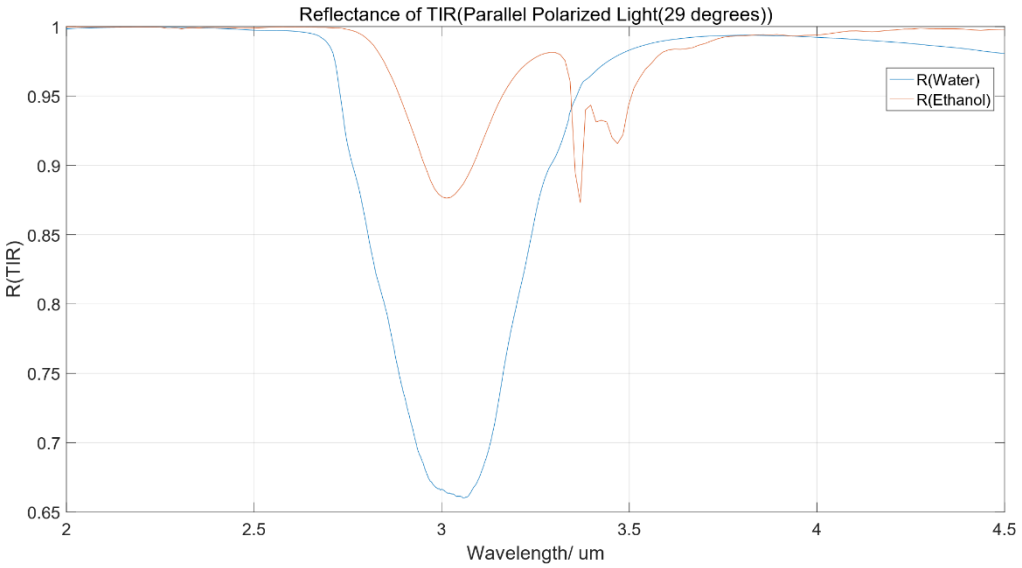

Figure 3.12 Reflectance of TIR (Parallel Polarized Light (29 degrees))

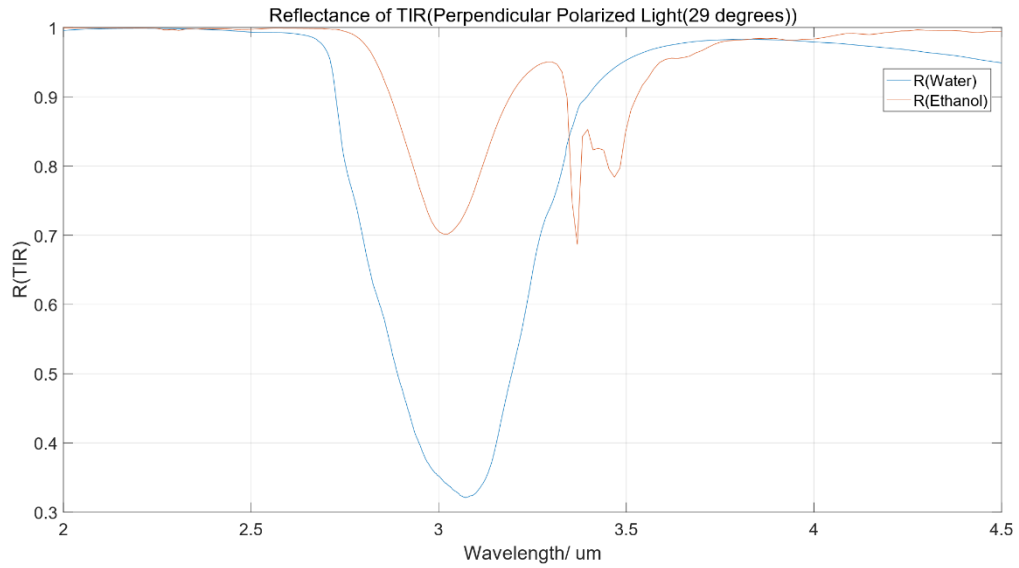

Figure 3.13 Reflectance of TIR (Perpendicular Polarized Light (29 degrees))

In Figure 3.14, the plots of reflectance of TIR of both of ethanol and water with different incident angles are given.

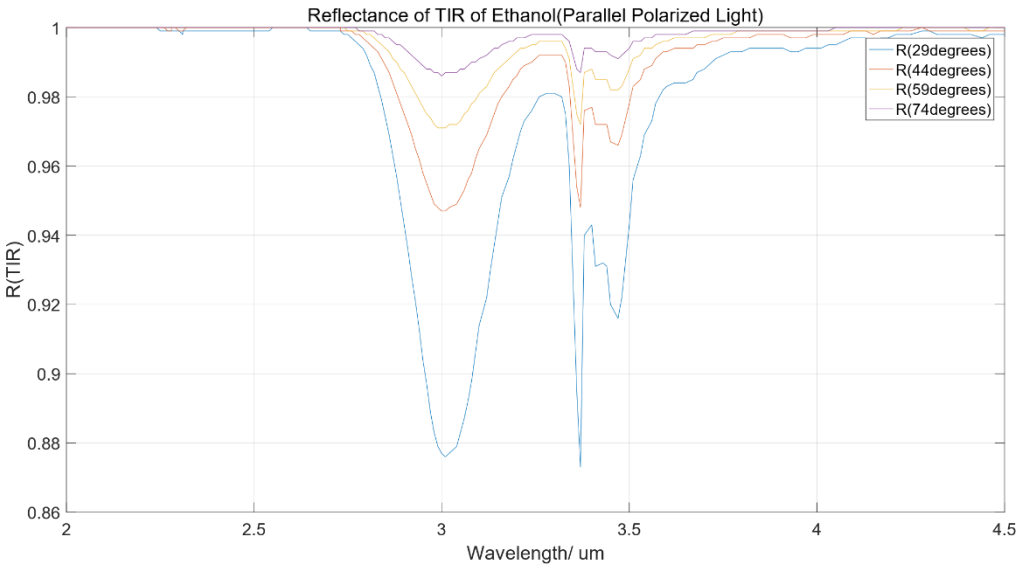

Figure 3.14 Reflectance of TIR of ethanol (parallel polarized light)

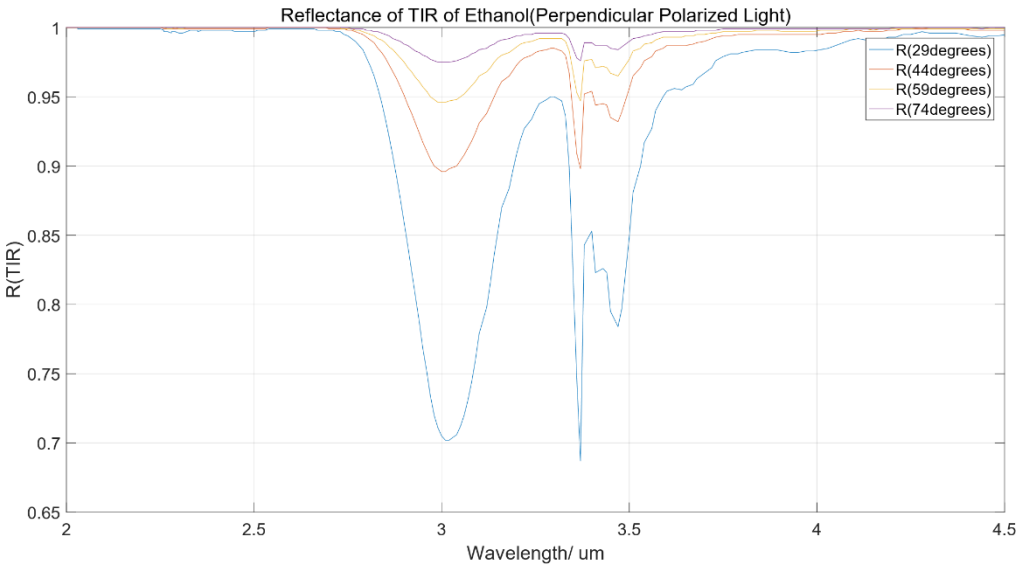

Figure 3.15 Reflectance of TIR of ethanol (perpendicular polarized light)

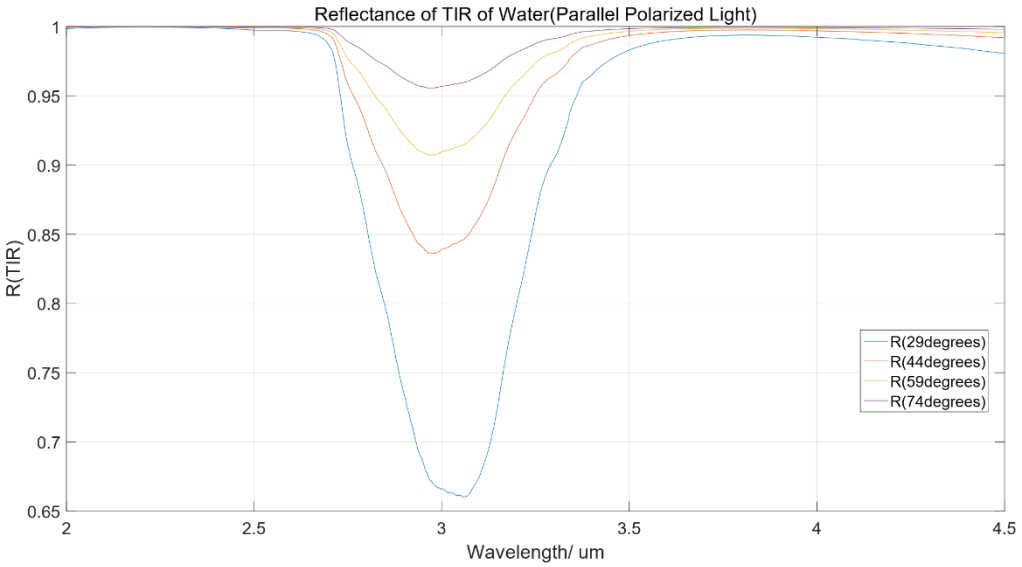

Figure 3.16 Reflectance of TIR of water (parallel polarized light)

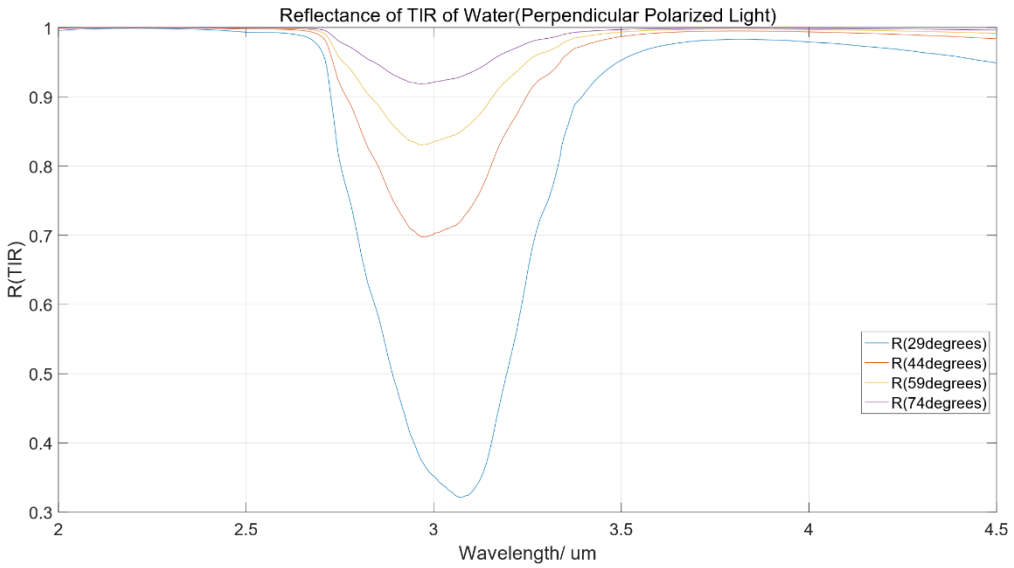

Figure 3.17 Reflectance of TIR of water (perpendicular polarized light)

As can be clearly seen from the figures above, the R value varies significantly when the incident angle changes. For the experimental data, the more distinguishable we want it to be, the greater the incident angle needs to be. Also it needs a very delicate calibration. Figure 3.18 Light paths in the fabricated silicon IRE's (internal reflection elements)Figure 3.18 shows several internal reflection elements which are fabricated by anisotropic etching using KOH on double polished <100> wafers [12].

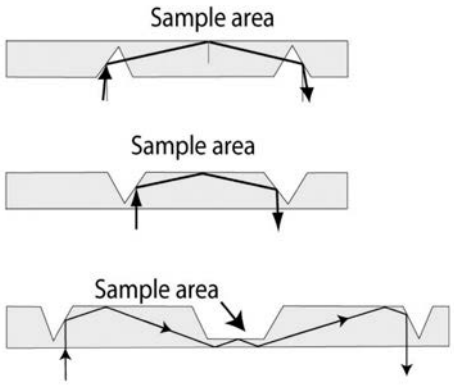

Figure 3.18 Light paths in the fabricated silicon IRE's (internal reflection elements) [12]

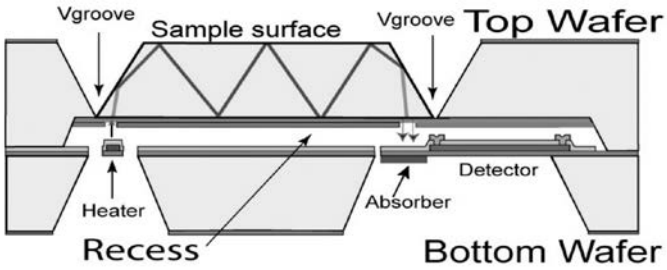

Figure 3.19 Cross-section of the fabricated spectrometer [12]

The high refractive index of silicon ensures that the infrared light can only exit at nearly the normal angle. As a consequence the light will be “trapped” inside of the silicon and multiple reflections can be easily realized. The same KOH etching can be used to fabricate it.

Compared with transmittance spectroscopy, total internal reflection is more feasible. However it still has some drawbacks. TIR requires delicate calibration and sometimes requires 2 wafers which is illustrated in Figure 3.19. That means TIR has a bad IC compatible ability. And it is really hard to control the polarization of the light that means the experimental result is unpredictable.

In next section waveguide devices will be introduced, and the design work and the fabrication will be based on waveguide.

3.1.3 Waveguide Structures

Waveguide structure which is made from a wafer is often called a silicon on oxide (SOI) device. Here in this section a general understanding of the nature of light propagation in an optical waveguide will be explained. Waveguide can be used in the application of measuring the concentrations is due to the fact that it has the similar theory with TIR. Waveguide uses the light’s evanexcent field the intereact with the liquid.

The optical waveguide is also a fundamental element that interconnects the various devices of an optical integrated circuit, just as a metallic strip does in an electrical integrated circuit. However, unlike electrical current that flows through a metal strip according to Ohm’s law, optical waves travel in the waveguide in distinct optical modes. A mode, in this sense, is a spatial distribution of optical energy in one or more dimensions that remains constant in time.

To begin the discussion of optical modes, consider the simple three-layer planar waveguiding structure of Figure 3.20 [16], The layers are all assumed to be infinite in extent in the y and z directions, and layers 1 and 3 are also assumed to be semi-infinite in the x direction. Light waves are assumed to be propagating in the z direction. It has been stated previously that a mode is a spatial distribution of optical energy in one or more dimensions. An equivalent mathematical definition of a mode is that it is an electromagnetic field which is a solution of Maxwell’s wave equation:

$$\nabla^2 E(r,t) = [n^2(r)/c^2]\partial^2 E(r,t)/\partial t^2 \ldots [16]$$

where *E* is the electric field vector, *r* is the radius vector, *n*(*r*) is the index of refraction, and *c* is the speed of light in a vacuum. For monochromatic waves, the solutions of the equation above have the form of:

$$E(r,t) = E(r)e^{i\omega t} \text{ ... [16]}$$

where *ω* is the radian frequency. Combining these two equations together we obtain:

$$\nabla^2 E(r) + k^2 n^2(r) E(r) = 0 \text{ ... [16]}$$

where $\kappa \equiv \omega/c$. If we assume, for convenience, a uniform plane wave propagating in the *z* direction, i.e., $E(r) = E(x,y)\, exp(-i\beta z)$, β being a propagation constant, then it becomes

$$\frac{\partial^2 E(x,y)}{\partial x^2} + \partial^2 E(x,y)\, \partial y^2 + [k^2 n^2(r) \beta^2] E(x,y) = 0 \text{ ... [16]}$$

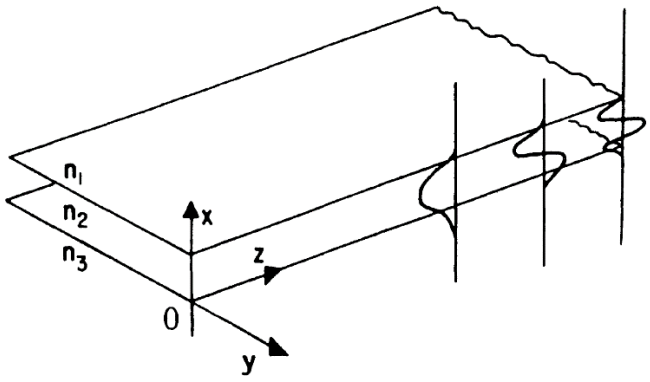

Figure 3.20 Diagram of the basic three-layer planar waveguide structure. Three modes are shown, representing distributions of electric field in the *x* direction [16]

Since the wavguide is assumed infinite in the *y* direction, by writing the equation above separately for the three regions in *x*, we can get:

$$\text{Region 1 } \partial^2 E(x,y)/\, \partial x^2 + (k^2 n_1^2 - \beta^2) E(x,y) = 0$$
$$\text{Region 2 } \partial^2 E(x,y)/\, \partial x^2 + (k^2 n_2^2 - \beta^2) E(x,y) = 0$$
$$\text{Region 3 } \partial^2 E(x,y)/\, \partial x^2 + (k^2 n_3^2 - \beta^2) E(x,y) = 0$$

where *E*(*x*, *y*) is one of the Cartesian components of *E*(*x*, *y*). The solutions of the equation set above are either sinusoidal or exponential functions of *x* in each of the regions, depending on whether $(k^2 n_1^2 - \beta^2)$, *i* = 1, 2, 3, is greater than or less than zero. Of course, *E*(*x*, *y*) and *∂E*(*x*, *y*)/*∂x* must be continuous at the interface between layers. Hence the possible modes are limited to those shown in Figure 3.21 [16],

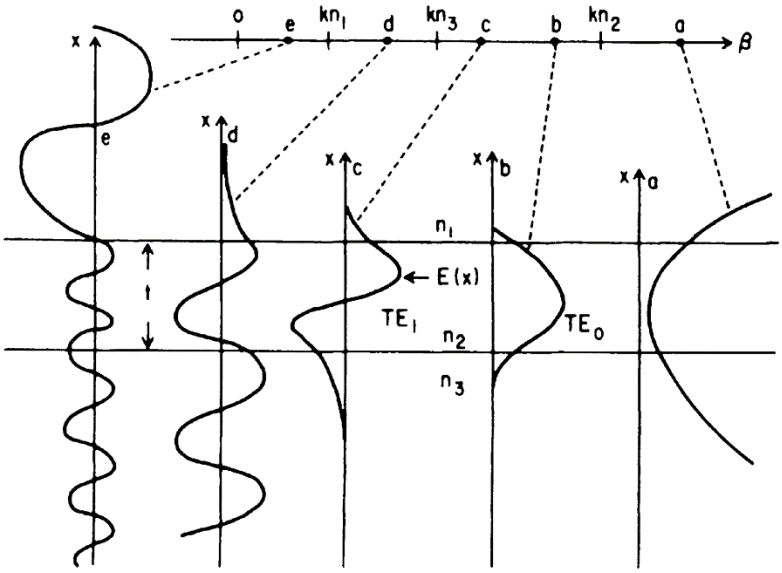

Figure 3.21 Diagram of the possible modes in a planar waveguide [16]

As a conslusion, the mode shape will change as a function of β if the frequency ω is constant and $n_2 > n_3 > n_1$. This ordering of the refractive index is a common case in all the works related to waveguides. The mode shown as (a) in Figure 3.21 is not physically realizable because the field increase unboundedly in the layers above and below, implying ininite energy. However, modes (b) and (c) will be well guided modes, often refered to as zeroth order and first order electric modes: TE_0 and TE_1 [17]. If β is greater than kn_1, mode cases of (d) and (e) will happen, whose electrical field at either the air interface or the substrate interface is sinusoidally varying. That means the light tends to be damped out at the interface, hence the (d) and (e) occasions are not useful in the researches about waveguides, but it will be very useful in coupler applications such as the tapered coupler which will be introduced later.

When designing the true waveguide sensors, people are likely to use a single-mode waveguide [18-21]. A single-mode waveguide is always refered to only TE_0 mode will be propagating inside of the waveguide. Because if only one basic mode is propagating, the penetration depth will be larger which means the light will have a better intereact with the sample. The higher order modes will have a worse intereaction with the sample, that leads to a situation of dynamic range. The dynamic range of the experimental result will be much higher if a single-mode device is used. So a problem of cut-off condition came up.

When the Maxwell's wave equation is fully solved, it can be seen that β can have any value when it is less between kn_3 and kn_2, but only discrete values of β are allowed. These values of β correspond to the various modes. So a cut-off problem has to be solved here. Theoritically this problem can be solved by this equation below:

$$\Delta n = n_2 - n_3 = (2m+1)^2 \lambda_0^2 / (32 n_2 t^2) \text{ ... [16]}$$

Given t is the thickness of the waveguide. The λ_0 is the cut-off wavelength of the light. m is the largest mode order which will propagate inside of the waveguide. When the t value and the wavelength are given, the permitted number of modes can be solved. This equation also means that when the wavelength is larger than λ_0, the light will be able to propagate in the waveguide. Using

this equation has some restrictions, for example the waveguide has to be a so-called asymmetric waveguide, in which n_1 is very much less than n_3. By using this equation above an approximately value of the waveguide's thickness can be obtained and it will be a sub-micron scale. However, the specific size values of the device has to be simulated and the results will be shown in next chapter.

As a conclusion, waveguide structure is much easy to fabricate compared with TIR devices. Also waveguide is IC compatible and standard CMOS process compatible because the KOH etching could be not needed when fabricating a waveguide device.

The only problem for a waveguide device is how to couple the light into the waveguide. Because the single-mode fibers for now available on the market all have a core diameter of around 9 micrometers, however, the size of core of the waveguide could be a sub-micron scale. So the coupling issue will also be considered on this thesis.

A brief introduction for the available coupling technologies will be given in the next section.

3.2 Coupling Technologies

3.2.1 Direct Focusing

The first coupling technology is going to be introduced here is direct focusing. It is the simplest method of transverse coupling of a laser beam to a waveguide. Direct focusing is also called end-fire approach, the schematic is shown in Figure 3.22 [16]. The waveguide structure could be a planar waveguide or a channel waveguide. The coupling efficiency can be caldulated, but here it is not going to be deduced.

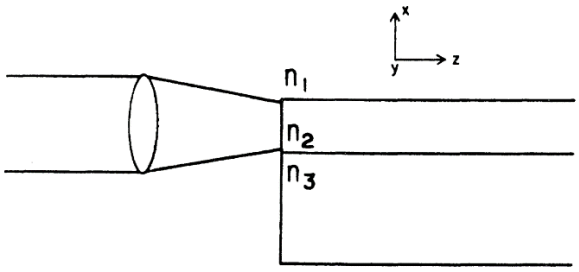

Figure 3.22 The transverse coupling method, which is sometimes reffered to as end-fire coupling [16]

This end-fire method is often used for coupling gas-laser beams to the fundamental waveguide mode because of the relatively good match between the Gaussian beam profile and the TE_0 waveguide mode shape.

The beam diameter must be close to the waveguide size so that the mode will match and the light can be coupled. Theoritically the coupling efficiency could be near to 100% if the the beam and the waveguide are optimally matched. However, efficiencies of from 50% to 70% are achieved [22-24]. End-fire coupling is often used in the laboratory because of its convenience.

3.2.2 End-Butt Coupling

Another transverse coupling method in the case of which couple a waveguide to a semiconductor laser, or to another waveguide. A parallel end-butt approach can be used, as shown in Figure 3.23 [16]. A very high coupling efficiency can be achieved by end-butt coupling if the thickness of waveguide layer is very close to the light emitting layer. This method is especially useful for coupling a laser diode to a planar waveguide.

If the laser diode operates in the fundamental TE0 mode and is coupled to a planar waveguide, as shown in Figure 3.23, the coupling efficiency for it can be deduced and calculated. This efficiency is hard to achieve by using either a presm, grating, or a tapered film coupler. The reason for this is that prism, grating and tapered film couplers are all very angle sensitive. The angle indicates the incident angle of the input light beam. It will be discussed later in this chapter.

Theoretical efficiency for end-butt coupling is around 90%, but in often an efficiency of from 40% to 60% is achieved [25, 26].

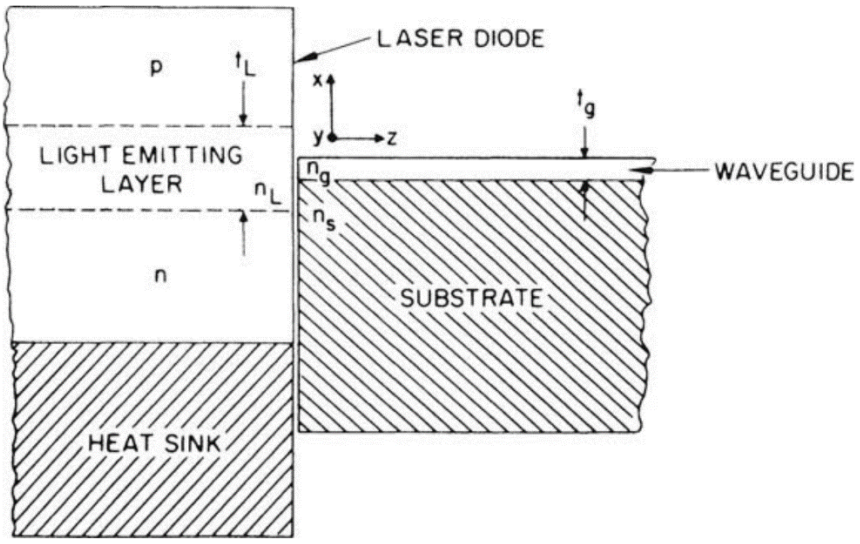

Figure 3.23 Parallel end-butt coupling of a laser diode and thin-film waveguide [16]

3.2.3 Prism Couplers

Transverse coupling can only be used when the end of the waveguide is exposed. Sometimes on an optical integrated circuit, only the surface of the optical device is exposed. As shown in Figure 3.24, it is the basic schematic of an attempt to couple light into a waveguide from a prism.

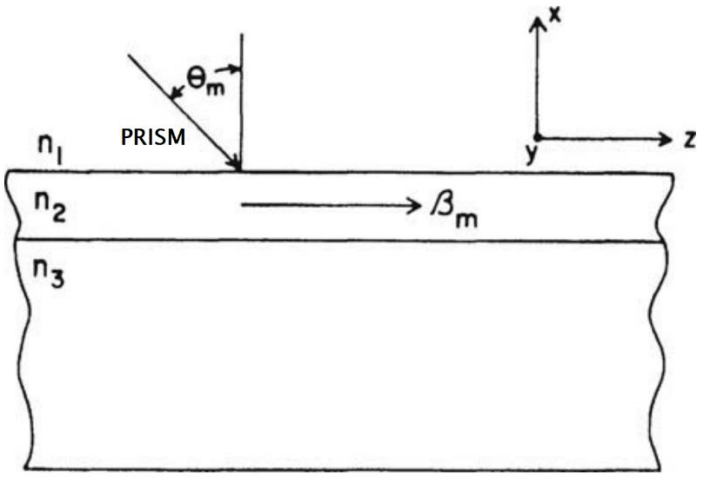

Figure 3.24 Diagram of an attempt to obliquely couple light into a waveguide through its surface [16]

If a prism is going to be used, a ohase-match condition must be satisfied, which requires:

$$\beta_m = kn_1 sin\theta_m = \frac{2\pi}{\lambda_0} n_1 sin\theta_m \text{ ... [16]}$$

As discuessed in the previous section, for a waveguide mode, should have $\beta_m > kn_1$.

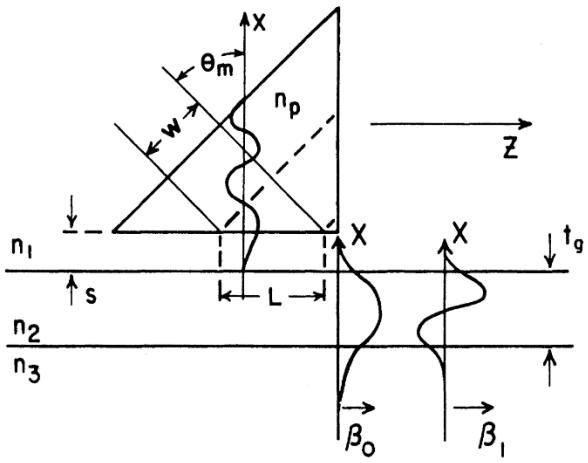

Figure 3.25 Diagram of a prism coupler. The electric field distributions of the prism mode and the *m* = 0, 1 waveguide modes in the *x* direction are shown [16]

One solution to the problem of phase matching is to use a prism, as shown in Figure 3.25. A beam of light of width *W* is directed into the face of the prism, which has $n_p > n_1$. The beam is totally internally reflected at the $n_p - n_1$ interface, setting up a standing wave mode in the prism, as shown in Figure 3.25. This mode is stationary in the *x* direction, but moves in the *z* direction with a phase constant β_p. In the waveguide, various guided modes can exist, moving in the *z* direction with phase constants β_m. All of these guided modes have an evanescent tail extending slightly beyond the $n_1 - n_2$ interface. If the prism spacing *s* is small enough so that the tails of the waveguide modes overlap the tail of the prism mode, there is coherent coupling of energy from the prism mode to the *m*th waveguide mode when θ_m is chosen so that $\beta_p = \beta_m$. The condition for matching of the β terms is given by:

$$\frac{2\pi n_p}{\lambda_0} sin\theta_m = \beta_m \dots [16]$$

The coupling efficiency of prism coupling can be deduced, but here it is not going to be discussed. However, for a Gaussian beam shape, it results that the maximum coupling efficiency is about 80%. The details were discussed in [27, 28]. And the formulas show that there are some constraints when using a prism as a input or output coupler. Firstly, in order to get a higher coupling efficiency with a uniform beam, the trailing edge of the beam must exactly intersect the right-angle corner of the prism. Another disadvantage of the prism coupler is that n_p must be not only greater than n_1 but also greater than n_2. In the case of glass waveguide, with indices around 1.5, it is easy to find suitable prism material with n_p greater than n_2. However, semiconductor waveguides, which typically have indices around 3 or 4, are more diffcult to couple with prisms. Both the index and the transparency of the prism material must be considered at the wavelength of interest. Another disadvantage of the prism coupler is that the incident beam must be highly collimated because of the critical angular dependence of the coupling efficiency into a given mode.

Prism couplers are very useful in laboratory applications where flexibility is desired regarding the position of the incident beam. However, the requirement of a stable mechanical pressure to hold the prism in place makes it less useful in practical applications, in which vibration and temperature variations are usually encountered. The grating coupler can be used to avoid this problem, without giving up the advantage of mode selectivity.

An interesting approach finished by Xin Yu which was published in 2016 [29]. There are many layers shown in Figure 3.26. The 6μm thick SiC acts as the tapered coupler. The 145nm SiC acts as a waveguide. The mechanism of this coupler is the same to the prism coupler but it was integrated on the wafer. It is a method between prism coupler and the tapered coupler. We decide not to use this method because we are using a wavelength range between 2.6μm and 3.8μm, the materials limit our device. We do not have several transparent materials to use under wavelength range of 2.6μm – 2.8μm.

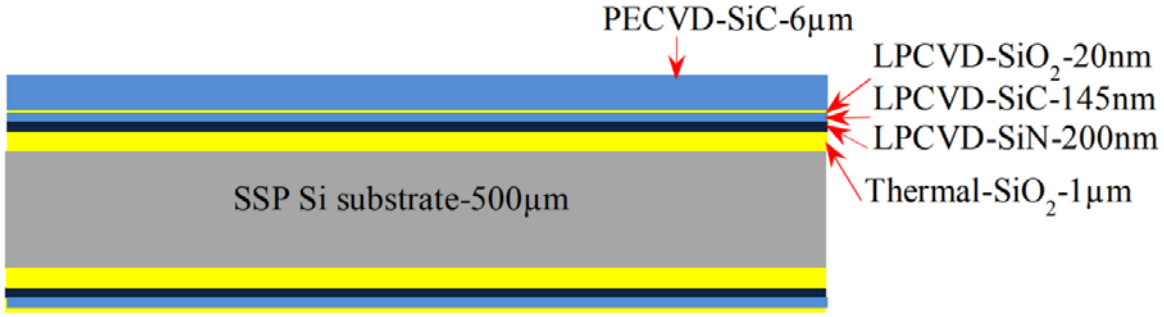

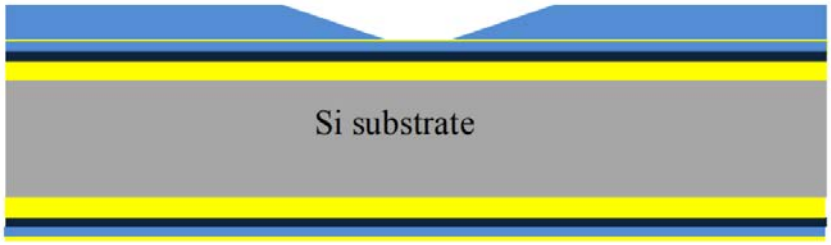

Figure 3.26 3D tapered coupler fabrication process [29]

3.2.4 Grating Couplers

Like the prism coupler, grating coupler is designed to produce a phase matching between a particular waveguide mode and an unguided optical beam which is incident at an oblique angle to the surface of the waveguide [16], the diagram of a grating coupler is shown in Figure 3.27.

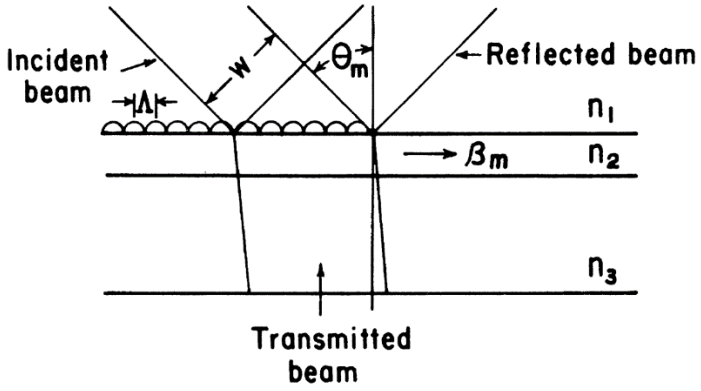

Figure 3.27 Diagram of a grating coupler [16]

Theoritically, an efficiency of approximately 80% is possible when coupling a Gaussian beam with a grating coupler. However, typical unblazed gratings (with symmetric profiles) generally have efficiencies of 10–30%.

The principal advantage of the grating coupler is that, once fabricated, it is an integral part of the waveguide structure. Hence, its coupling efficiency remains constant and is not altered appreciably by vibration or ambient conditions. Also, the grating coupler can be used on high-index semiconductor waveguides for which it is difficult to obtain a suitable prism material. However, since it is highly angle dependent, the grating coupler cannot be used effectively with the relatively divergent beam of a semiconductor laser. Perhaps the greatest disadvantage of the grating coupler is that it is difficult to fabricate, requiring the use of sophisticated masking and etching techniques.

3.2.5 Tapered Couplers

A basic cross-section schematic of a tapered coupler is shown in Figure 3.28 [16]. The coupling mechanism can be conveniently visualized be using the ray-optic approach. A guided light incident onto the end of a tapered coupler and bounces with the angle of incidence. When the angle of incidence becomes less than the critical angle for total internal reflection, the energy is refracted into the substrate.

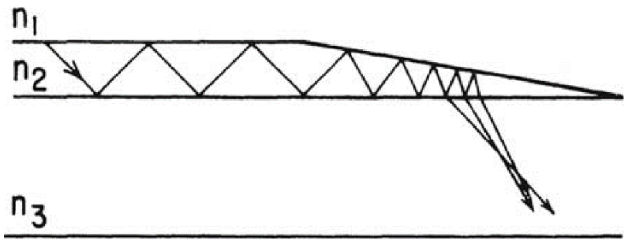

Figure 3.28 Diagram of a tapered coupler [16]

The greatest advantage of the tapered coupler is that it is simple to fabricate and functions reasonably well as an output coupler. However, it forms a divergent beam, as shown in Figure 3.28, which spreads over an angle of 1–20◦, depending on the taper. This divergent beam is somewhat inconvenient to use, but can be tolerated in many applications in which the form of the output beam is not a critical factor.

In principle, the tapered coupler can also be used as an input coupler. However, in order to obtain high efficiency, one would have to construct a converging input beam which was the reciprocal of the diverging beam shown in Figure 3.28. Since this is practically an impossibility, only very low efficiencies are usually observed when tapered waveguides are used as input couplers.

3.2.6 Tapered Mode Size Converters

Many different geometries can be used to either expand or contract the mode. A review of various taper designs that have been used has been done by Moerman et al. [30]. Some of the lateral tapers that they considered are show.n in Figure 3.29.

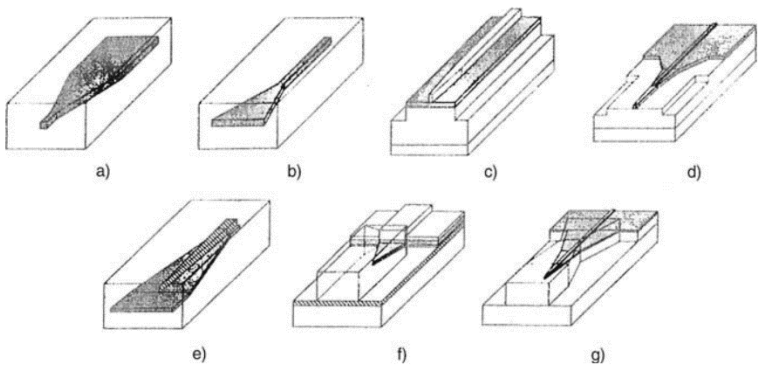

Figure 3.29 a-g Lateral taper designs [30]

In Figure 3.29, Figure **a-g** are: **a** Lateral down-tapered buried waveguide. **b** Lateral up-tapered buried waveguide. **c** Single lateral taper transition from a ridge waveguide to a fibermatched waveguide. **d** Multisection taper transition from a ridge waveguide to a fiber-matched waveguide. **e** Dual lateral overlapping buried waveguide taper. **f** Dual lateral overlapping ridge waveguide taper. **g** Nested waveguide taper transition from a ridge waveguide to a fiber-matched waveguide [30].

Vertical tapers, in which the thickness of the waveguiding layer is changed, can also be used to make mode size converters. However, special growth and etching techniques are required to change the thickness along the taper [30].

3.3 Conclusion

After the discussion of the technologies and methods, the waveguide seems to be the most suitable method for the application. Thus a most suitable way of coupling must to be confined. Considering the fabrication of the waveguide and coupler, and the equipments in the cleanroom in the EEMCS building. We decided to choose a both vertical and lateral mode size converter to couple the light. Accidentally, we have the suitable fabrication technique to fabricate a vertical coupler. As discussed before the material for the waveguide core and the coupler are chosen to be poly-silicon. And there needs to be a substrate layer of silicon oxide to confine the light. The feasibility of this structure and the detialed design will be decided after several sets of simulation. These will be shown in the next chapter.

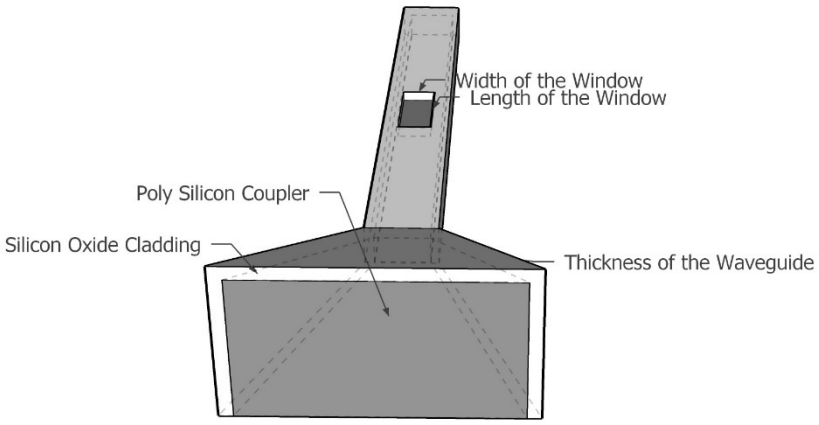

Figure 3.30 Schematic of the waveguide design

The final waveguide design will look like the structure in Figure 3.30, a tapered structure is connected with the waveguide core and a silicon oxide cladding is covered on the whole structure. A window will be etched to make a interreaction field. The reason of adding a cladding is that the sample's absorbance is too high and will be explained in the next chapter.

References

[1] F. E. Dowell, T. C. Pearson, E. B. Maghirang, F. Xie, and D. T. Wicklow, "Reflectance and Transmittance Spectroscopy Applied to Detecting Fumonisin in Single Corn Kernels Infected with Fusarium verticillioides," *Cereal Chemistry Journal,* vol. 79, no. 2, pp. 222-226, 2002/03/01 2002.

[2] B. G. Osborne, T. Fearn, and P. H. Hindle, *Practical NIR spectroscopy with applications in food and beverage analysis*. Longman scientific and technical, 1993.

[3] F. C. SHOP. (2015). *CUVETTES*. Available: https://www.fireflysci.com/news/2015/9/8/cuvette-path-length

[4] T. G. Mayerhöfer, H. Mutschke, and J. Popp, "Employing Theories Far beyond Their Limits—The Case of the (Boguer -) Beer – Lambert Law," *ChemPhysChem,* vol. 17, no. 13, pp. 1948-1955, 2016.

[5] D. M. Wieliczka, S. Weng, and M. R. Querry, "Wedge shaped cell for highly absorbent liquids: infrared optical constants of water," *Applied optics,* vol. 28, no. 9, pp. 1714-1719, 1989.

[6] E. Sani and A. Dell'Oro, "Spectral optical constants of ethanol and isopropanol from ultraviolet to far infrared," *Optical Materials,* vol. 60, pp. 137-141, 2016.

[7] NIST Chemistry WebBook. (1969). *Water's Infrared Spectrum*. Available: http://webbook.nist.gov/cgi/cbook.cgi?ID=C7732185&Type=IR-SPEC&Index=1#IR-SPEC

[8] NIST Chemistry WebBook. (1965). *Ethanol's Infrared Spectrum*. Available: http://webbook.nist.gov/cgi/cbook.cgi?ID=C64175&Type=IR-SPEC&Index=3#IR-SPEC

[9] WIKIPEDIA. (2017). *Total Internal Reflection*. Available: https://en.wikipedia.org/wiki/Total_internal_reflection

[10] W. Greiner, *Relativistic quantum mechanics*. Springer, 1990.

[11] J. C. Maxwell, *A dynamical theory of the electromagnetic field*. The Society, 1864.

[12] G. De Graaf, "Mid-infrared microspectrometer systems," Ph.D, EEMCS, TU Delft, Delft, 2008.

[13] A. W. Snyder and J. Love, *Optical waveguide theory*. Springer Science & Business Media, 2012.

[14] H. Li, "Refractive index of silicon and germanium and its wavelength and temperature derivatives," *Journal of Physical and Chemical Reference Data,* vol. 9, no. 3, pp. 561-658, 1980.

[15] W. Heller, "Remarks on refractive index mixture rules," *The Journal of Physical Chemistry,* vol. 69, no. 4, pp. 1123-1129, 1965.

[16] R. G. Hunsperger and J. R. Meyer-Arendt, "Integrated optics: theory and technology," *Applied Optics,* vol. 31, p. 298, 1992.

[17] R. G. Hunsperger, "Theory of optical waveguides," in *Integrated Optics*: Springer, 2009, pp. 33-52.

[18] R. Horváth, H. C. Pedersen, and N. B. Larsen, "Demonstration of reverse symmetry waveguide sensing in aqueous solutions," *Applied physics letters,* vol. 81, no. 12, pp. 2166-2168, 2002.

[19] J. Vörös *et al.*, "Optical grating coupler biosensors," *Biomaterials,* vol. 23, no. 17, pp. 3699-3710, 2002.

[20] R. Horvath, L. R. Lindvold, and N. B. Larsen, "Reverse-symmetry waveguides: theory and fabrication," *Applied Physics B: Lasers and Optics,* vol. 74, no. 4, pp. 383-393, 2002.

[21] R. Kunz, "Miniature integrated optical modules for chemical and biochemical sensing," *Sensors and Actuators B: Chemical,* vol. 38, no. 1-3, pp. 13-28, 1997.

[22] M. Haruna, Y. Segawa, and H. Nishihara, "Nondestructive and simple method of optical-waveguide loss measurement with optimisation of end-fire coupling," *Electronics Letters,* vol. 28, no. 17, pp. 1612-1613, 1992.

[23] H. Hsu, A. Milton, and W. Burns, "Multiple fiber end fire coupling with single - mode channel waveguides," *Applied Physics Letters,* vol. 33, no. 7, pp. 603-605, 1978.

[24] G. Stegeman, R. Wallis, and A. Maradudin, "Excitation of surface polaritons by end-fire coupling," *Optics letters,* vol. 8, no. 7, pp. 386-388, 1983.
[25] R. G. Hunsperger, A. Yariv, and A. Lee, "Parallel end-butt coupling for optical integrated circuits," *Applied optics,* vol. 16, no. 4, pp. 1026-1032, 1977.
[26] S. K. Sheem and T. G. Giallorenzi, "Two-dimensional silicon grooves for altitudinal alignment in fiber end-butt coupling," *Optics letters,* vol. 3, no. 3, pp. 73-75, 1978.
[27] T. Tamir, "Beam and waveguide couplers," in *Integrated Optics*: Springer, 1975, pp. 83-137.
[28] M. Klimov, V. Sychugov, A. Tishchenko, and O. Parriaux, "Optimization of optical waveguide grating couplers," *Fiber & Integrated Optics,* vol. 11, no. 1, pp. 85-90, 1992.
[29] Y. Xin, G. Pandraud, L. S. Pakula, B. Morana, and P. J. French, "Combination of LPCVD and PECVD SiC in fabricating evanescent waveguides," in *Nano/Micro Engineered and Molecular Systems (NEMS), 2016 IEEE 11th Annual International Conference on*, 2016, pp. 549-552: IEEE.
[30] I. Moerman, P. P. Van Daele, and P. M. Demeester, "A review on fabrication technologies for the monolithic integration of tapers with III-V semiconductor devices," *IEEE Journal of Selected Topics in Quantum Electronics,* vol. 3, no. 6, pp. 1308-1320, 1998.

Chapter 4. Simulation and Structure Design

Based on the theory discussed before, a waveguide is chosen to realize the liquid composition analysis. This chapter is going to explain how the waveguide is designed under simulation results. The schematic of the device is shown in Figure 4.1, and it is a typical silicon on insulator (SOI) device.

Figure 4.1 Cross section schematic of a waveguide

The structure design is based on a design procedure as follow:

- Firstly, the thickness of the silicon oxide layer should be confirmed.
- Secondly, the sizes of the waveguide should be confirmed.

This whole design is based on several sets of simulations. Different configurations of the silicon oxide layer and the waveguide and the liquid are introduced to give initial idea of the design. Besides, the mode of the light is also an important issue to be concerned.

4.1 Simulation Method

Part of the simulations of this design are completed by COMSOL, a platform for physics-based modelling and simulation. And there are two ways to simulate the whole structure: 2D simulation and 3D simulation.

A 2D simulation structure is shown in Figure 4.1. In this 2D simulation, the length and the thickness of the waveguide can be set. But the width of the waveguide is assumed to be infinitely large.

A 3D simulation structure is shown in Figure 4.2, and the configurations of parameters are illustrated in Figure 4.3 and Figure 4.4. Every parameter can be set differently in a 3D simulation.

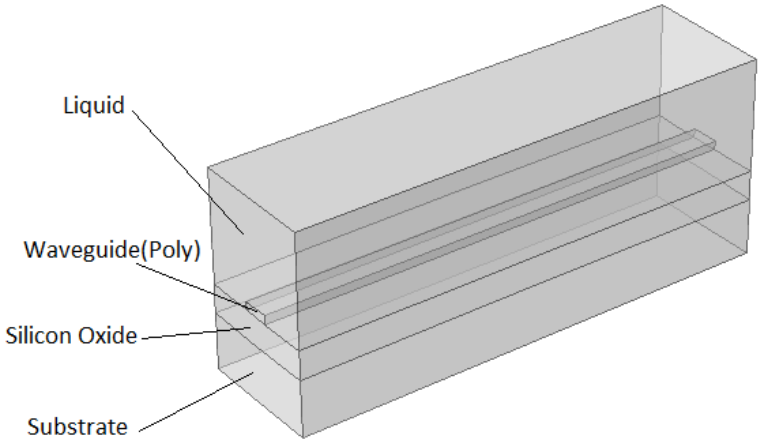

Figure 4.2 Schematic of 3D waveguide

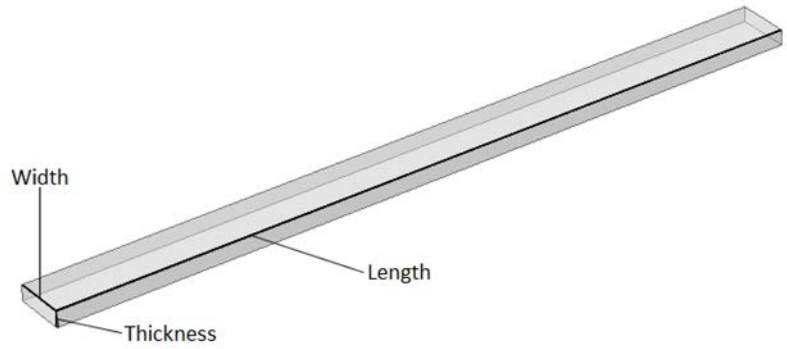

Figure 4.3 Waveguide core (poly-silicon)

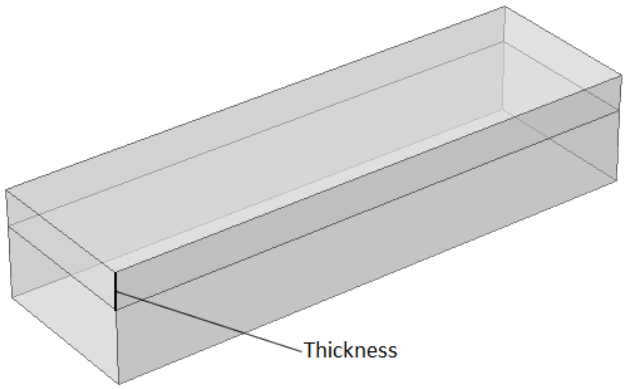

Figure 4.4 Silicon oxide and substrate

The parameters are going to be confirmed are shown in Figure 4.3 and Figure 4.4, including the thickness of the silicon oxide layer and thickness, width, and length of the waveguide.

As discussed in last chapter, a single mode light is desired to propagate in the waveguide. Therefore, the simulation must be able to analysis each different mode. A preliminary simulation tells that the 3D simulation does not have the ability to analysis a single mode light except the basic mode TE0. An

example is shown in Figure 4.5 which does not make any sense. However, a 2D simulation has its shortage of an infinite large dimension which makes it unable to analysis the width of the core and has many approximations.

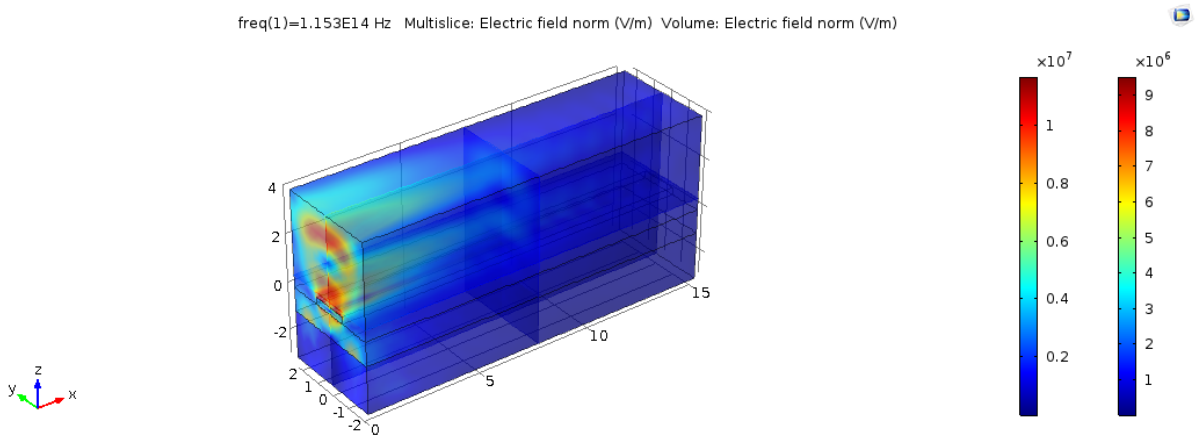

Figure 4.5 A Preliminary simulation of analysing TE1 mode in 3D simulation

In a word, the 2D simulation and 3D simulation must be combined to design the structure.

The simulating and design sequence is: Firstly, the thickness of the silicon oxide layer should be confirmed to make sure the light is not going to leak into another layer. Secondly, the thickness of the waveguide should be confirmed to make sure a single mode light is propagating inside of the waveguide because the thickness limits the mode. Thirdly, the width of the waveguide should be confirmed to make sure most of the light can go into the waveguide. Finally, the length of the waveguide should be confirmed to make sure the time of the interaction between the light and the liquid is long enough to detect the optical properties of the liquid. After these steps, the design of the structure will be finished.

However, COMSOL is not enough for our application because the calculation workload is too much for a long 3D structure to give a 'out of memory' result. Another alternative simulation method is needed. Hence, a MATLAB® toolbox called BeamLab will be used in the later simulation. BeamLab is an award-winning set of simulation tools for beam propagation through optical devices and waveguides in your familiar MATLAB® environment.

4.2 2D Simulations

2D simulation can be used to analysis the modes of light, so it can be a direct method to design the thicknesses of the silicon oxide layer and the waveguide. Both two wavelength ranges of interests will be simulated in this chapter. In these simulations, the absorption rate of the liquid will be set as zero.

4.2.1 Silicon Oxide Layer Thickness

Firstly, the thickness of the oxide layer will be simulated in a 2D simulation, three occasions are shown in Figure 4.6, Figure 4.7 and Figure 4.8: the light will be leaked when the oxide layer is too thin, light leaking when the oxide layer is not thick enough, and no light leaked when the layer is thick enough.

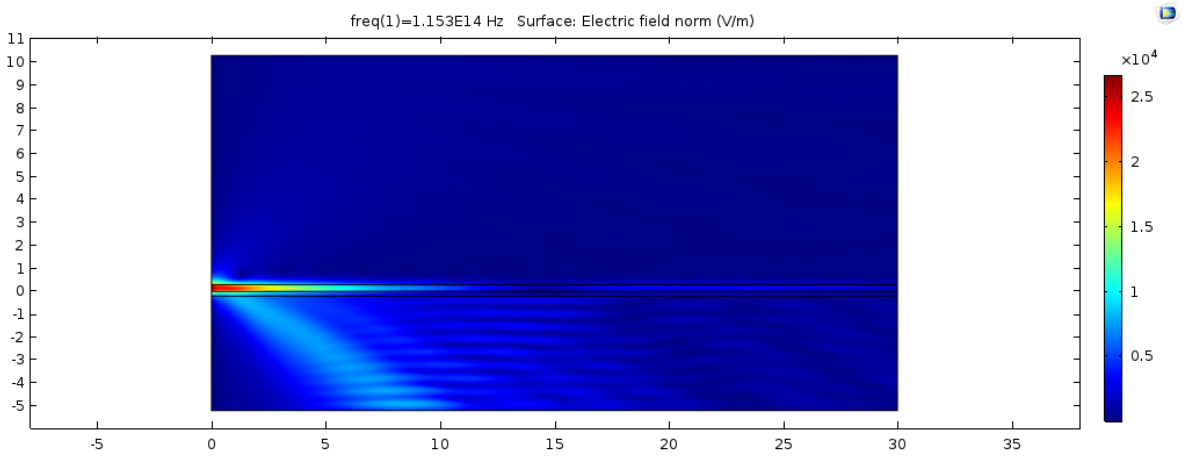

Figure 4.6 Leaking light when the oxide layer is too thin (0.2 μm)

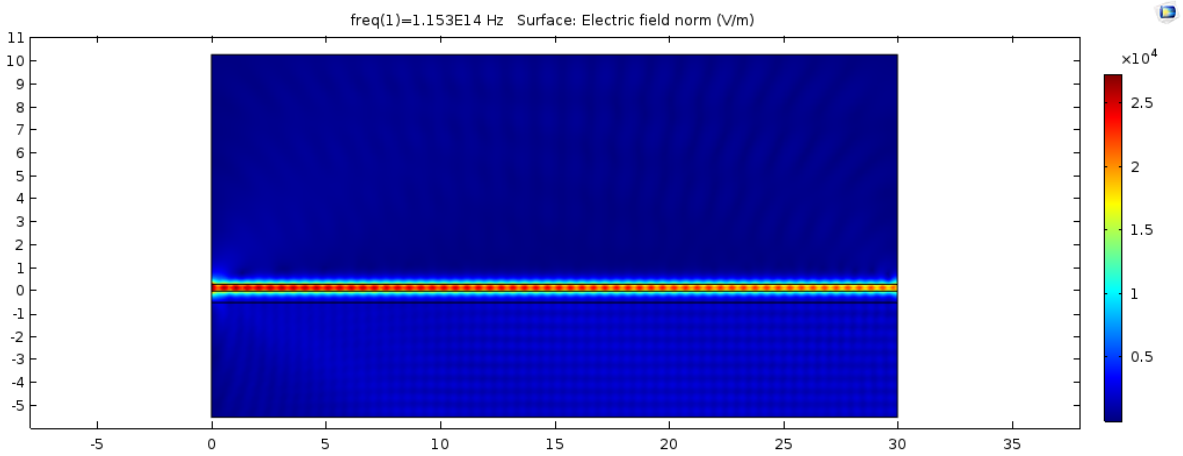

Figure 4.7 Leaking light when the oxide layer is not thick enough (0.5 μm)

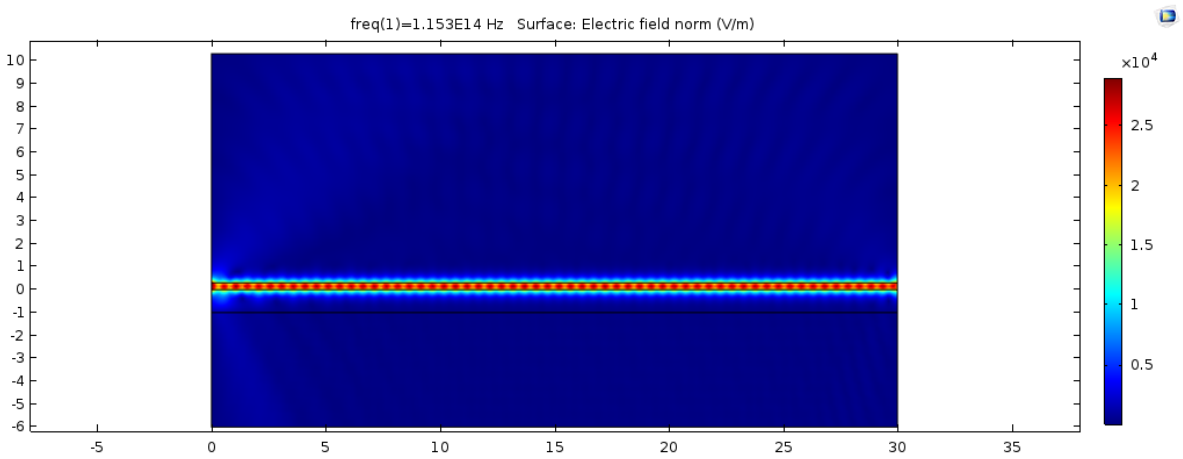

Figure 4.8 No light is leaking when the oxide layer is thick Enough (1 μm)

Occasion in Figure 4.6 happens because the oxide layer is too thin and light prefers to propagate in a thicker medium, and also the substrate is made of silicon, the mechanism was discussed in Chapter 3 and is illustrated in Figure 3.21. In Figure 4.7, the light gets weaker at the end of the waveguide, this also can be explained by Figure 3.21. However, the light in Figure 4.8 propagates well.

As discussed in last chaper, there are two wavelength ranges of interests: 2.6μm - 2.8μm and 3.5μm - 3.8μm. Two summary figures of efficiencies vs. thicknesses of oxide layer for both wavelength ranges are made as below in Figure 4.9 and Figure 4.10.

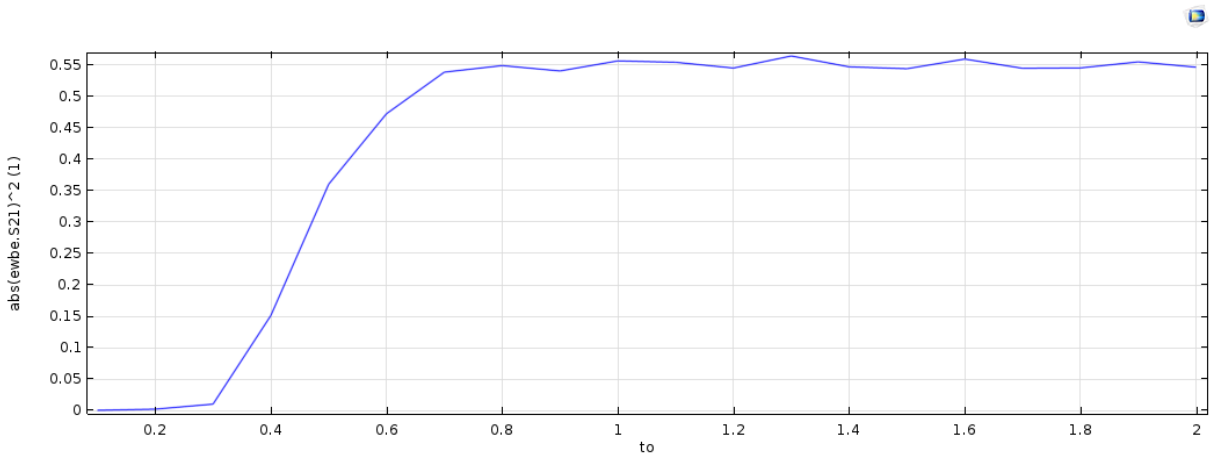

Figure 4.9 Efficiency vs. thickness of oxide layer (2.6μm - 2.8μm)

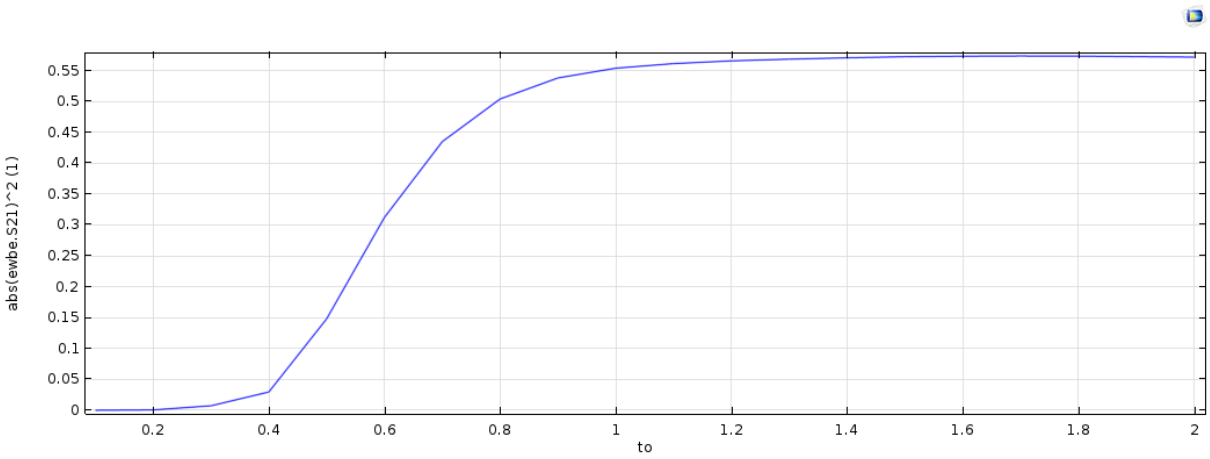

Figure 4.10 Efficiency vs. thickness of oxide layer (3.5μm - 3.8μm)

For wavelength range 2.6μm - 2.8μm, Figure 4.9 shows from 0.8μm on, the efficiency tends to be steady which means there is very little light leak from the waveguide. For wavelength range 3.5μm - 3.8μm, the situation is the same and is shown in Figure 4.10. As a conclusion, an 1-μm-thick oxide layer is enough for the practical use. But in the simulations after, the thickness of the oxide layer will be set as 2μm for safety reason.

4.2.2 Waveguide Thickness

In this section, both two wavelength ranges will be analysed. Simulation in 2D can analysis any single mode of light, both highest order mode and lowest order mode can be analysed in one simulation. A basic knowledge is that when the thickness of the waveguide is increasing, the number of modes will also be increasing, this can explain from Figure 3.21. So Figure 4.11 shows when the thickness of the wabeguide goes up, how the efficiencies of the highest order mode light changes.

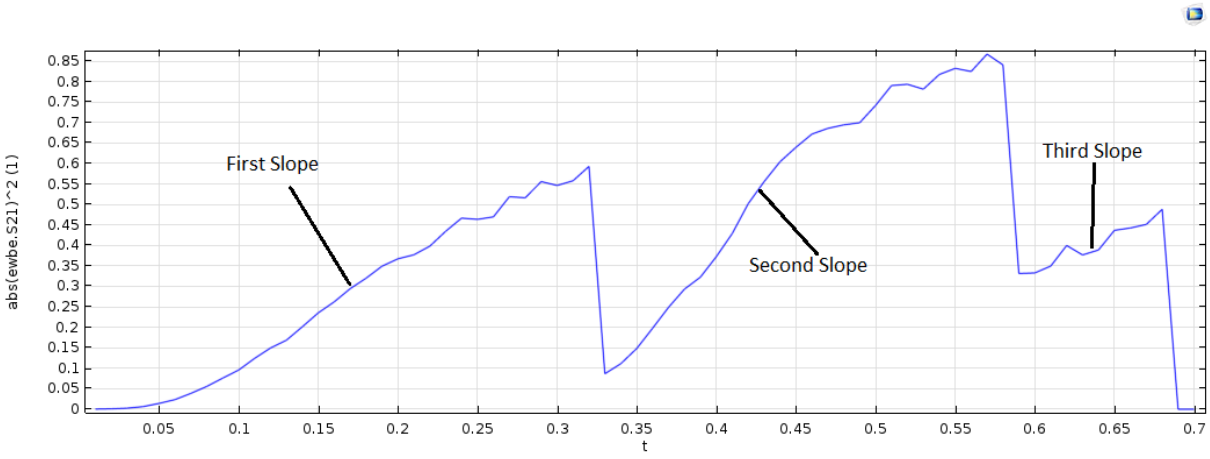

Figure 4.11 Efficiency of highest order mode (2.6μm - 2.8μm)

The first slope in Figure 4.11 is the efficiency curve for TE0 mode, the second slope is for TE1 mode and the third slope is for the TE2 mode. Note that while the TE1 and TE2 modes are propagating, the TE0 mode is also propagating but the curve is not shown in the figure, only the highest order mode's

efficiency curve is shown in the Figure. As a conclusion, the TE1 mode starts to propagate from the thickness of 0.33μm. That is to say the thickness of the waveguide has to be limited within 0.33μm.

Figure 4.12 shows a single TE0 mode analysis run for this wavelength range (only TE0 mode is shown in this figure). Part of this curve is the same with the first slope in Figure 4.11.

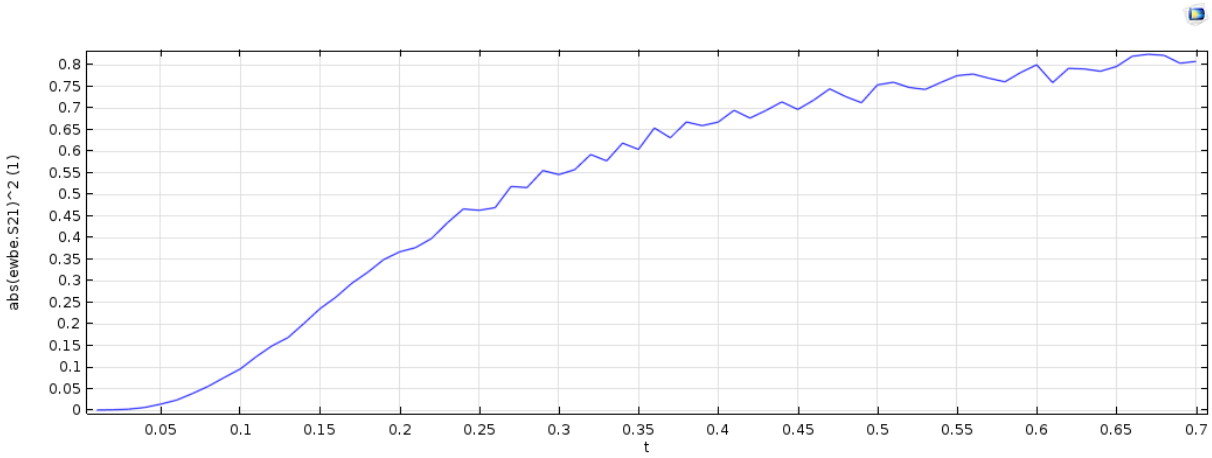

Figure 4.12 Efficiency of lowest order mode (2.6μm - 2.8μm)

As for the other wavelength range 3.5μm - 3.8μm, similar simulation results are gained. Figure 4.13 shows the efficiencies of the highest order mode light when the thickness of waveguide is changing. And Figure 4.14 is for the lowest mode light which means TE0 mode only. These two figures are similar with Figure 4.11 and Figure 4.12.

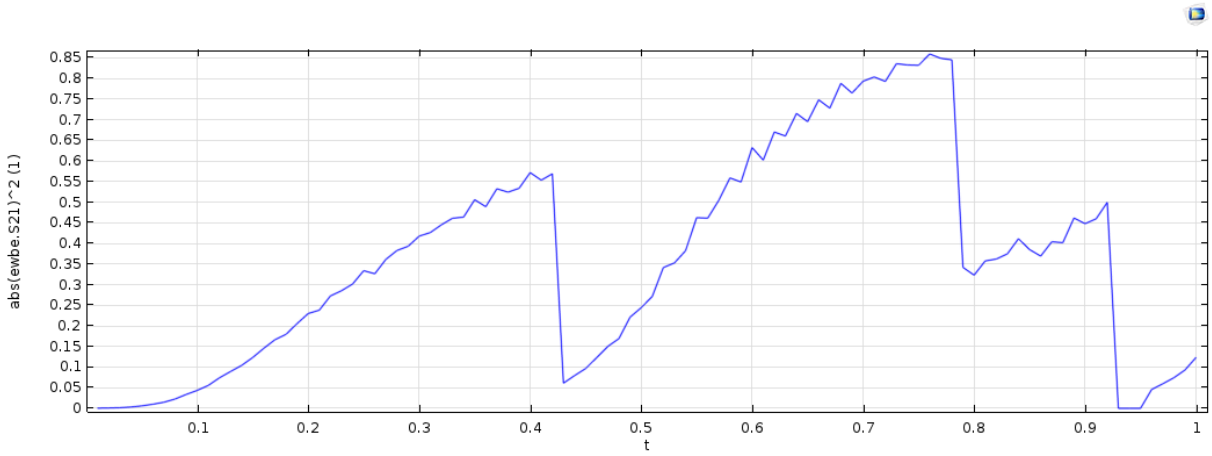

Figure 4.13 Efficiency of highest order mode (3.5μm - 3.8μm)

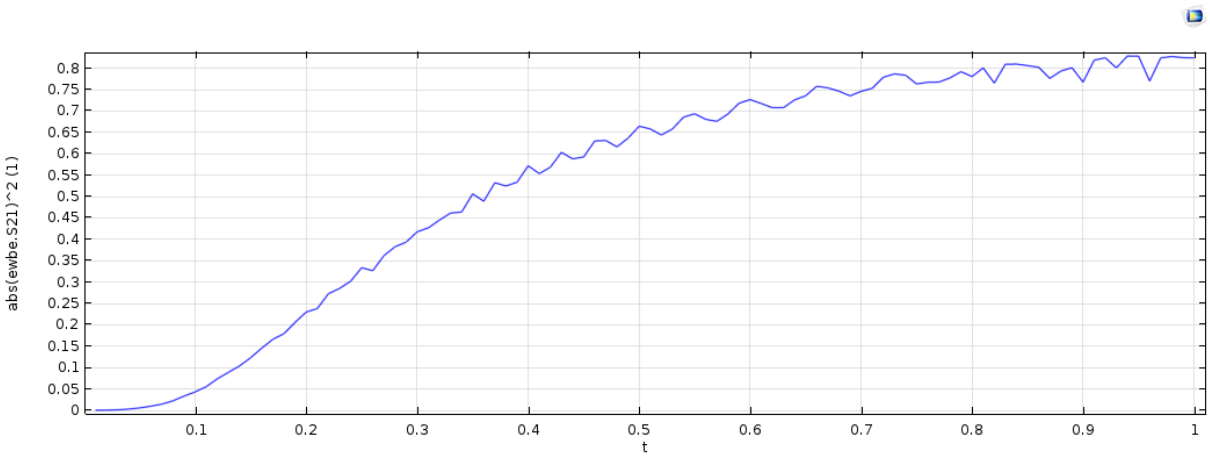

Figure 4.14 Efficiency of lowest order mode (3.5μm - 3.8μm)

The conclusion is similar with the other range of interests. The thickness of the waveguide should be limited within 0.41μm.

Concerning about the refractive index of the liquid is always changing when the concentration of each different composision is changing, far safety reason, the thicknesses of the waveguides for both wavelength ranges will be limited as 0.3μm and 0.4μm. However, the 2D simulations assume the waveguide is a planar waveguide so they have many constraints. COMSOL is a trustable simulation tool, so this set of simulations can be regarded as reference simulations for the next step simulations.

The best case for our design is that two designs with two different sets of structures are designed for each range of interests. However, we still have the possibility to make one set of structures to make it is capable of guide the two wavelength ranges of light.

4.3 3D Simulations

After the approximate thickness is found, several sets of 3D simulations are needed to determined the widths and the lengths. At the beginning COMSOL is used and then it is found to be not capable to simulate a longer structure. Then a MATLAB toolbox called Beamlab is used to finish the simulations.

4.3.1 3D COMSOL Simulations

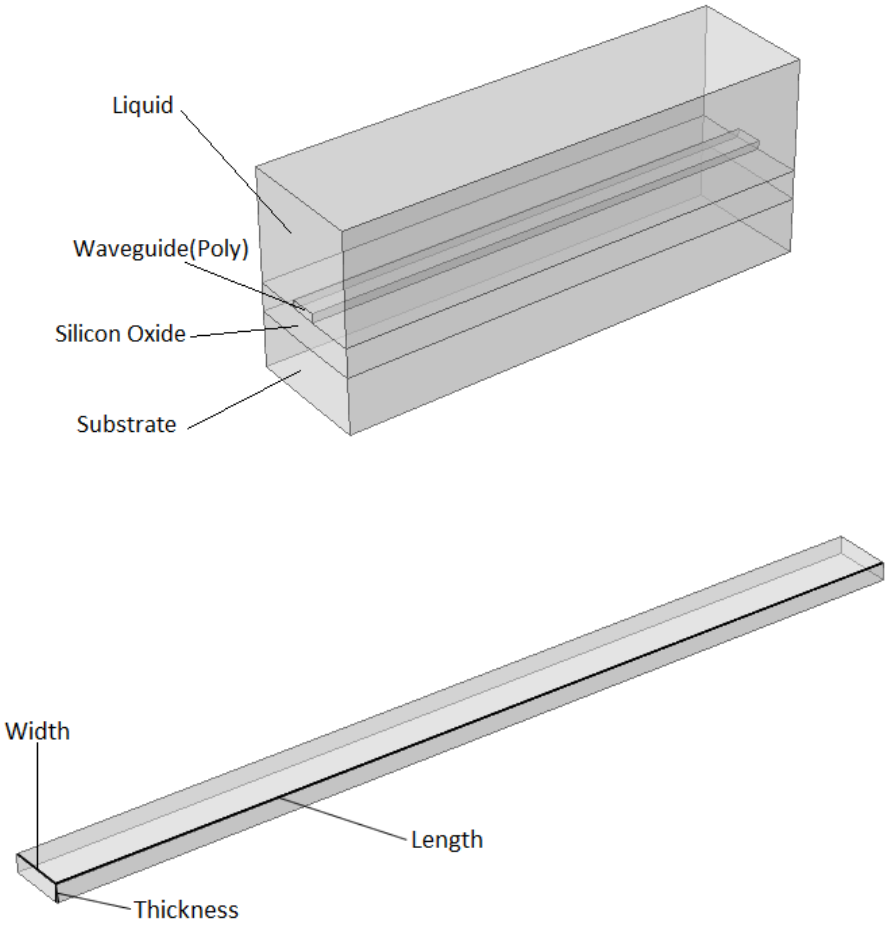

Figure 4.15 Schematic of the waveguide model

Figure 4.15 shows the schematic of the built waveguide in COMSOL. The mesh should be set very small to make sure the accuracy of the simulation high enough, at the same time the calculation workload becomes too much for the server to run. Hereby, the length of the waveguide is set as 15μm to make sure the simulation could be successfully run.

The widths should be determined during the 3D simulating. So the absorption of the liquid above the waveguide will not be applied.

Details of the simulation setups are: the thicknesses are fixed and set as 0.3μm for range 2.6μm - 2.8μm and 0.4μm for range 3.5μm - 3.8μm. Physic of electromagnetic waves, beam envelopes is used. Port input power is 1W. Study is set with two boundary mode analysises and one frequency domain. Then a parametric sweep is applied to sweep the width.

Figure 4.16 and Figure 4.17 show two cases of which the width is too small and the width is large enough. The different colors shown in these figures give an intuitive impression of the intensity of light. And it is clear that in Figure 4.16 the light is getting weaker during propagation while Figure 4.17 shows that the light is propagating very steady. When the width is too small, the light will be lost

during propagation because the waveguide is not capable of hold that mode of light. And also the width should not be too large because the light's modes should be limited when propagating inside the waveguide. If the waveguide is too wide, then it will be capable of guiding other modes of light.

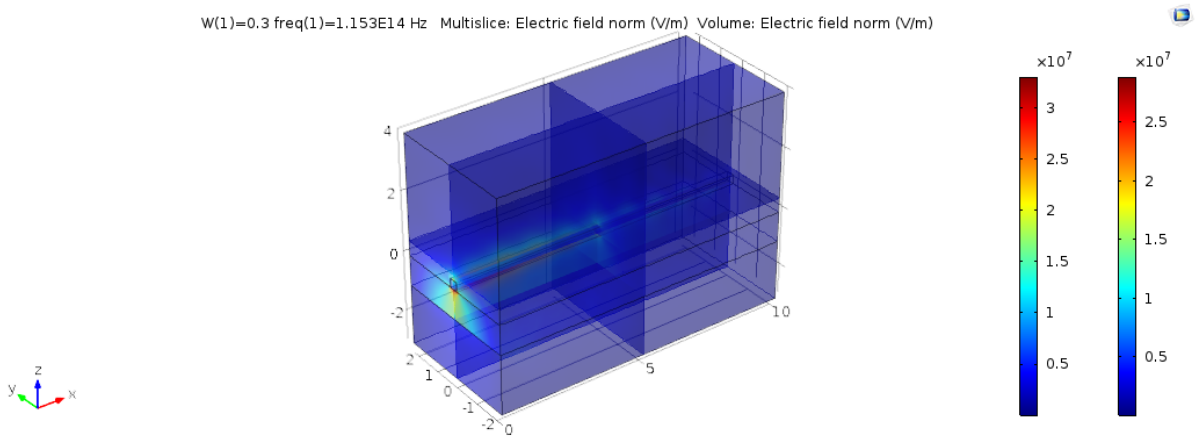

Figure 4.16 Light inside of the waveguide when width is too small

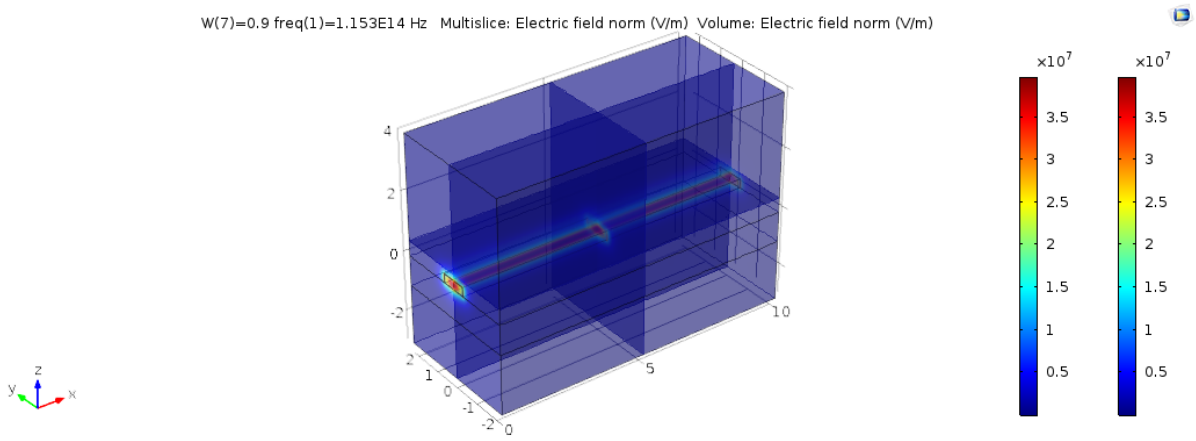

Figure 4.17 Light inside of the waveguide when width is large enough

In order to see how the both two ranges will perform, the boundary values: 2.6μm, 2.8μm, 3.5μm, 3.8μm should be analyzed seperately.

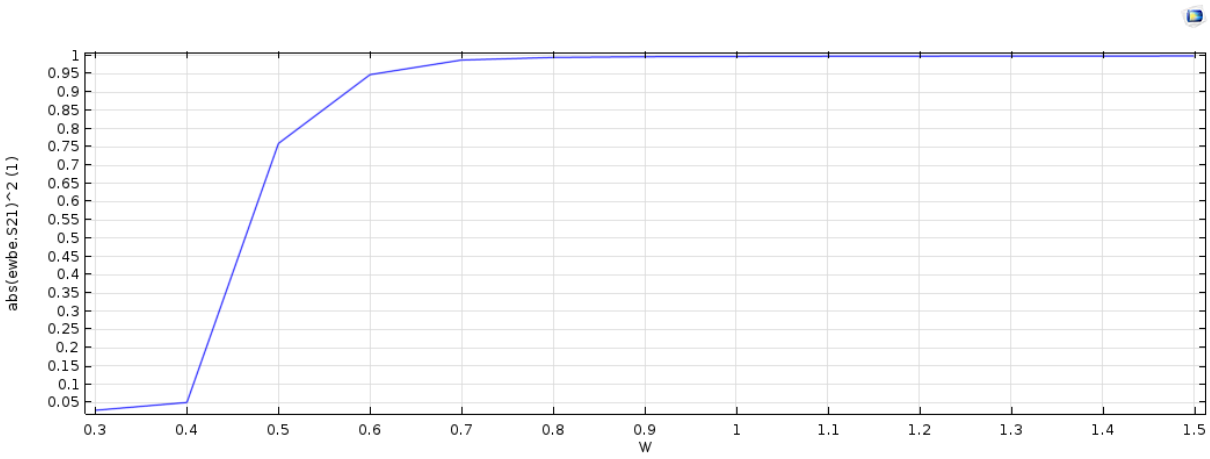

Figure 4.18 Width vs. transmitted power (2.6µm wavelength)

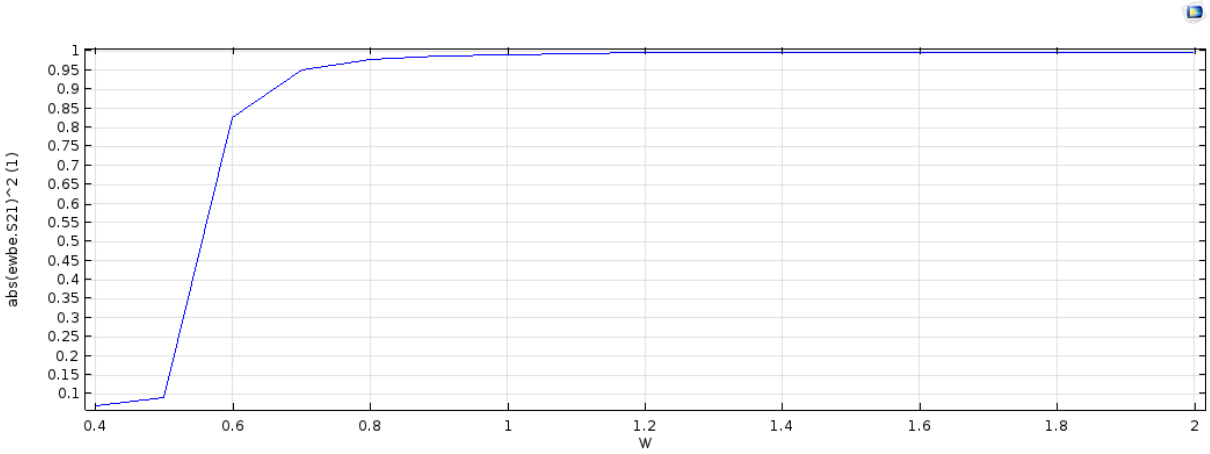

Figure 4.19 Width vs. transmitted power (2.8µm wavelength)

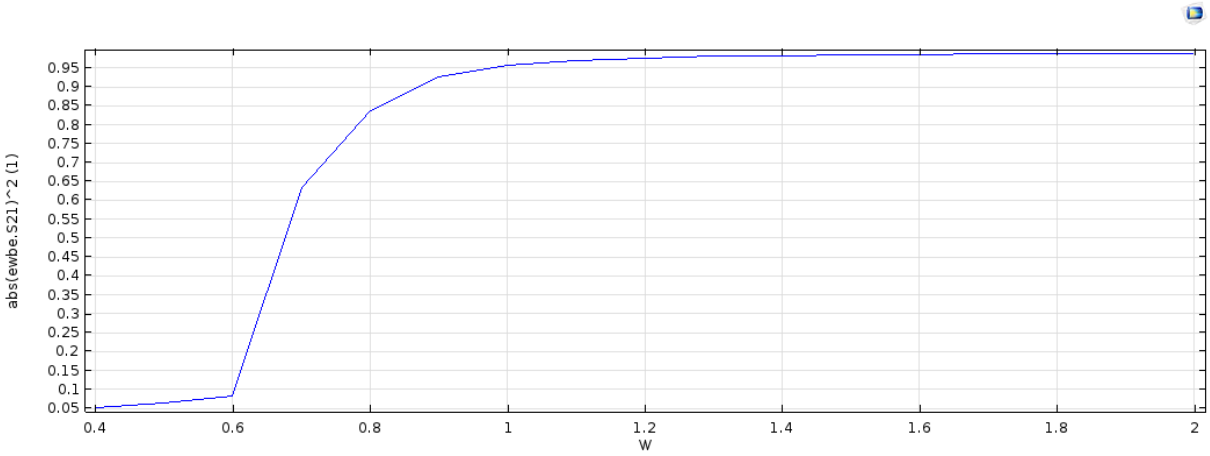

Figure 4.20 Width vs. transmitted power (3.5µm wavelength)

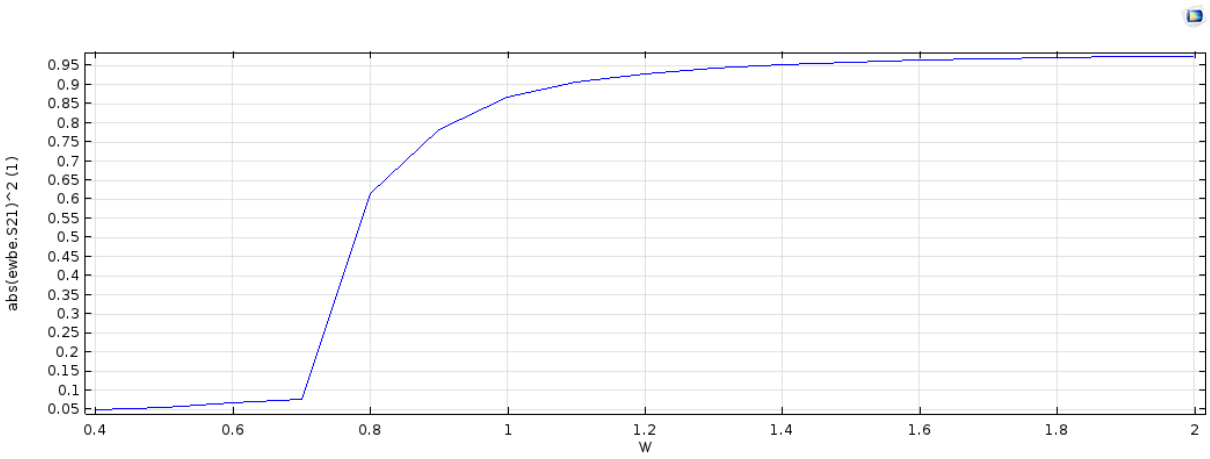

Figure 4.21 Width vs. transmitted power (3.8μm wavelength)

The width vs. transmitted power figures for the boundary values are Figure 4.18, Figure 4.19, Figure 4.20 and Figure 4.21. And the steady values of the thickness are 0.7μm, 1μm, 1.4μm and 1.8μm respectively. The curves in these figures give the information that when the width value is large enough, the light can be propagating steady and no light is leaking. Under this premise, the width should be as small as possible. Also for one range, the highest value of the thickness should be chosen in case of light leaking.

The conclusion is that the widths value for the both ranges can be roughly estimated as 1μm and 1.8μm.

4.3.2 3D MATLAB Simulations

In this set of simulations, the width should firstly be tested. The purpose of this simulation is to see how the light's power is changing when the light is propagating in the waveguide. The details of the settings are: thickness is fixed as 0.3μm and 0.4μm, light's input power is 1W, resolution of x and y direction is 0.02μm, resolution for z is 1μm, length is set as 100μm and the width is changeable.

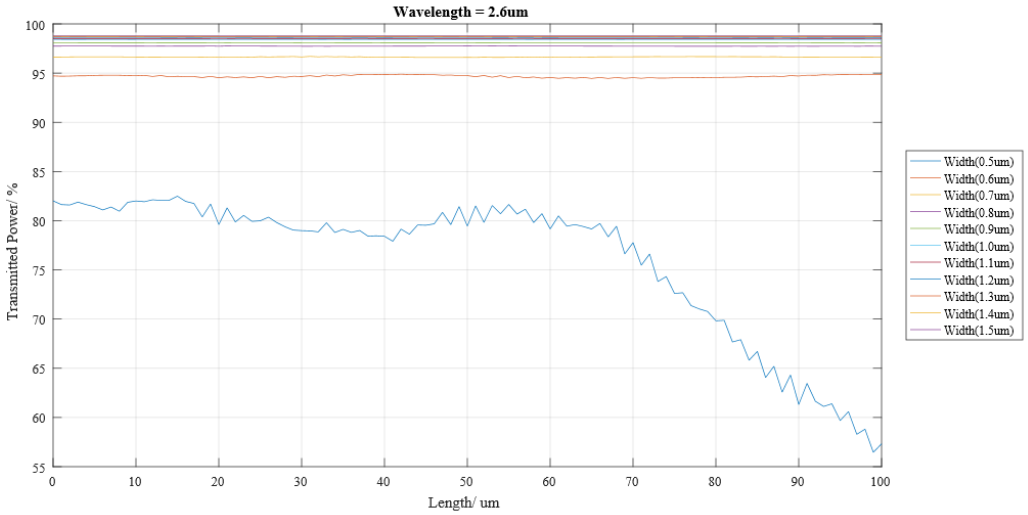

Figure 4.22 Light power along the waveguide of differernt widths(2.6μm wavelength)

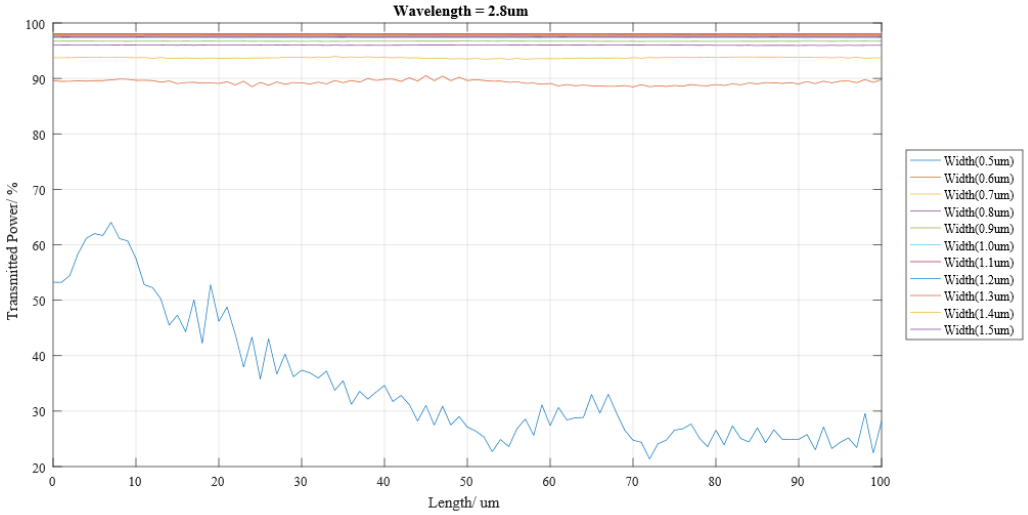

Figure 4.23 Light power along the waveguide of differernt widths(2.8μm wavelength)

Figure 4.22, Figure 4.23, Figure 4.24 and Figure 4.25 are the light power values inside of the waveguide and at every micrometer during propagation, and each curve is under different width value. This set of simulation is to see if the light propagates steady under different width values. Then a reasonable width value can be chosen for the width. Further on simulations for lengths can be set based on the chosen width and thickness.

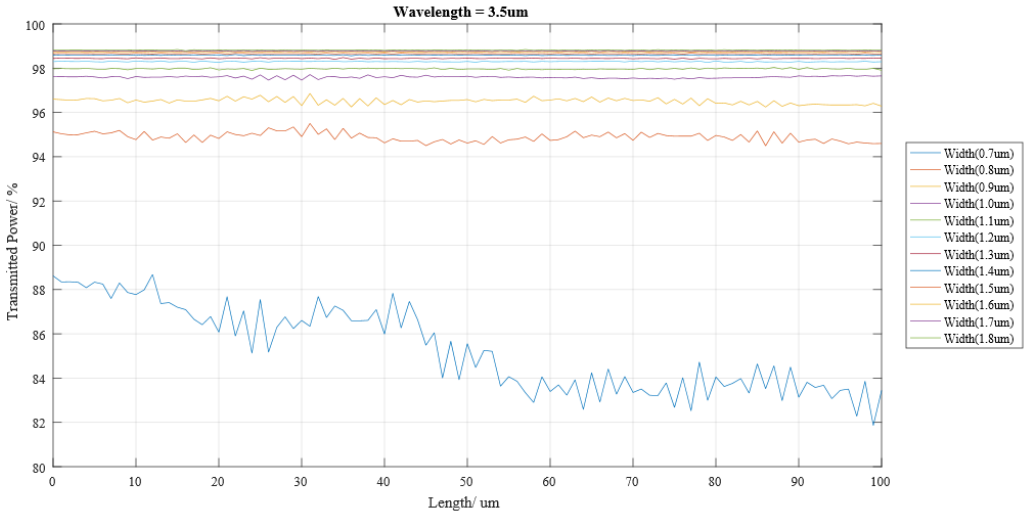

Figure 4.24 Light power along the waveguide of differernt widths(3.5μm wavelength)

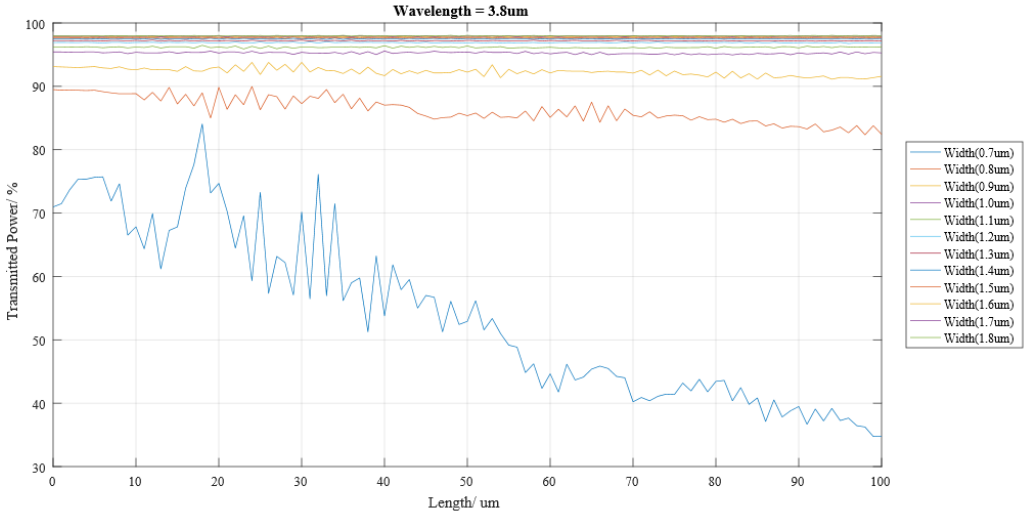

Figure 4.25 Light power along the waveguide of differernt widths(3.8μm wavelength)

The curves in Figure 4.22, Figure 4.23, Figure 4.24 and Figure 4.25 from bottom to top are under lowest to highest width values respectively. It is clear that when the width is too small the light's power is going to lose during propagating. Also the light's power is not steady during the whole propagation.

Combine Figure 4.22 with Figure 4.23, the light's propagation is steady and has a high transmitted power rate from the width value of 1.0μm.

Combine Figure 4.24 with Figure 4.25, the light's propagation is steady and has a high transmitted power rate from the width value of 1.5μm.

The simulation result from this MATLAB toolbox is similar with the result of COMSOL's. During the fabrication step, all the values can be used to make difference devices because tens of devices can be made together on a single wafer.

After this set of simulations, the rough width values of the structures can be achieved. The length of the interreacting area and the thickness of oxide cladding still need to be simulated. If we choose to use two different sets of sensors, that is to say, we have to use two sets of masks to fabricate and this will cost us double time to fabricate.

4.3.3 Length Simulations

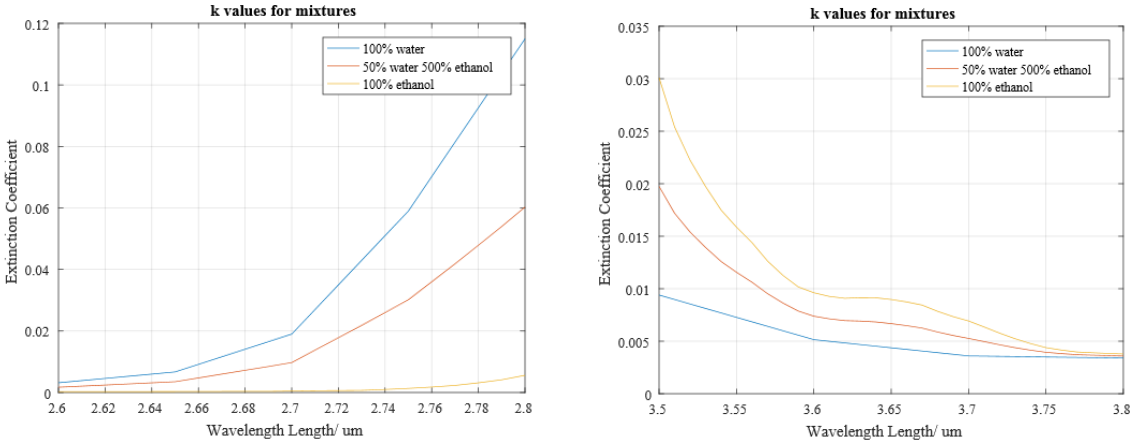

Figure 4.26 Extinction coefficients for different wavelength ranges and different compositions

The extinction coefficients are calculated first for the mixtures. And the curves are shown in Figure 4.26. This figure shows that the absorption difference between water and ethanol and this data will be used in the next step of simulations.

Figure 4.27, Figure 4.28, Figure 4.29 and Figure 4.30 are showing the tansmitted power under different liquid conpositions for different interacting lengths. These three figures are simulated for 20μm, 40μm, 60μm and 100μm length accordingly. These figures are for the first wavelength band: 2.6μm – 2.8μm, thickness was set as 0.3μm and width was set as 1.0μm. Within this range, the absorption rate is quite high, hence the interacting length is quite short. In Figure 4.29 and Figure 4.30, the curves at the bottom have a situation of too much absorbtion. Hence the length of this device should be controlled within 60μm.

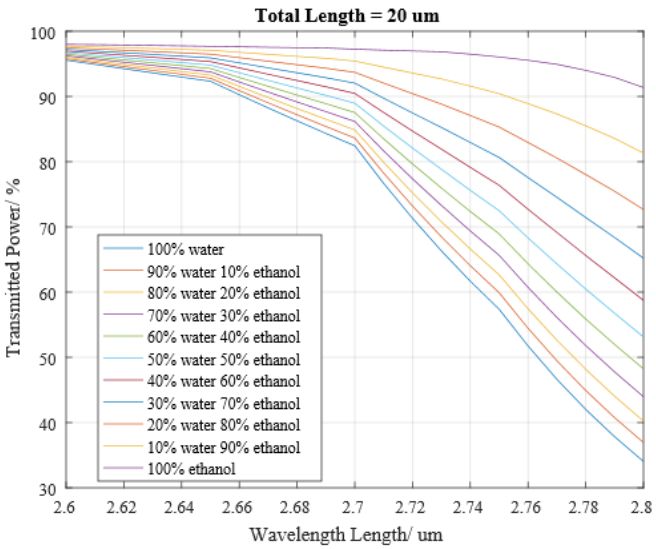

Figure 4.27 Transmitted power under different compositions, total length = 20 µm

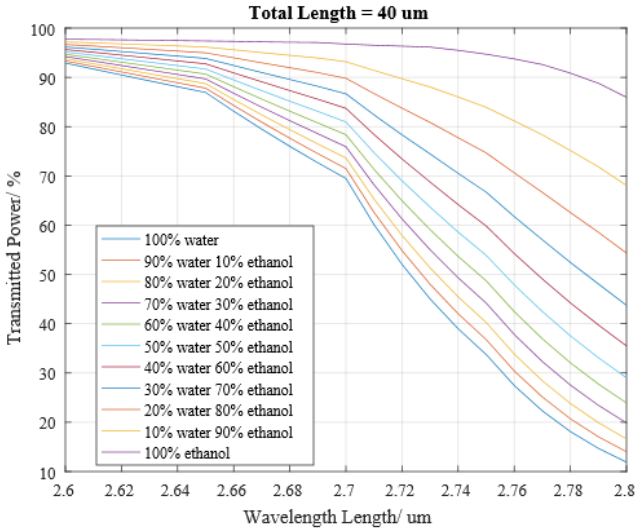

Figure 4.28 Transmitted power under different compositions, total length = 40 µm

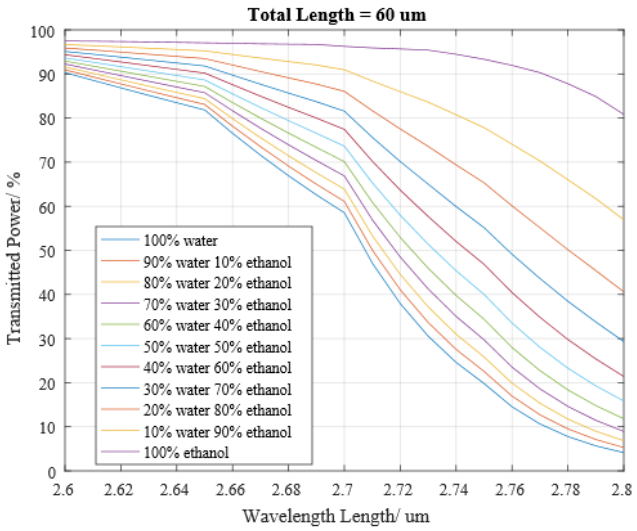

Figure 4.29 Transmitted power under different compositions, total length = 60 μm

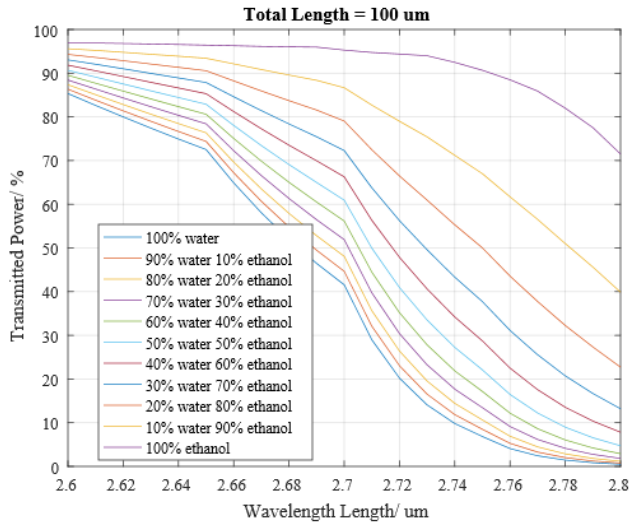

Figure 4.30 Transmitted power under different compositions, total length = 100 μm

Figure 4.31, Figure 4.32 and Figure 4.33 show the curves for different compositions and different lengths of the device. Because of the higher absorption rate of this wavelength range compared with the previous range, the lengths of the devices in the figures are 100μm, 150μm and 200μm accordingly. Thickness was set as 0.4μm, and width was set as 1.5μm.

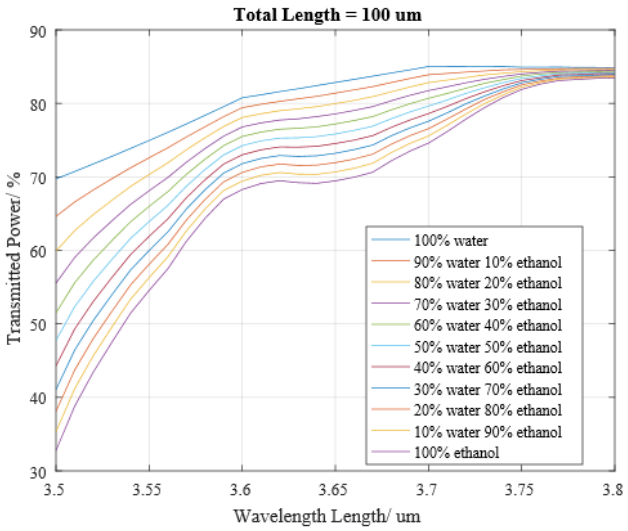

Figure 4.31 Transmitted power under different compositions, total length = 100 µm

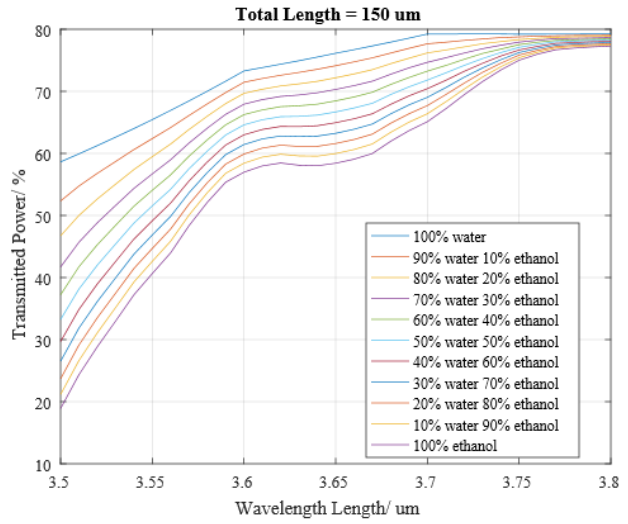

Figure 4.32 Transmitted power under different compositions, total length = 150 µm

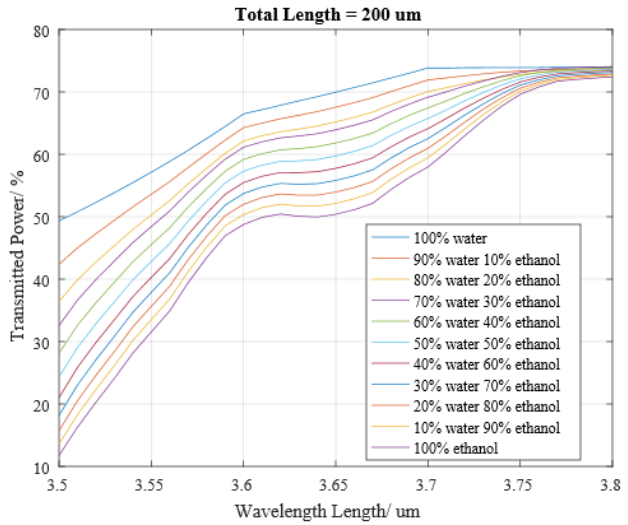

Figure 4.33 Transmitted power under different compositions, total length = 200 µm

In reality, the device will be covered with a oxide layer to prevent interreaction. And a window will be enched to make the light interfering with the liquid. This length which was simulated is actually the length of the window.

COMSOL® was used to simulate the cladding thicknesses. Notice that these simulations for the cladding are simulated under the wavelength of 2.8μm and the liquid is water only because the absorbtion rate is the highest. So this is a worst-case analysis. And also to check if the results from BeamLab toolbox is correct.

Figure 4.34 gives a 200μm length cladding with different thickness. A high absorbtion rate was applied into this simulation. And it is clear that if the thickness of the cladding is too small, some of the light will be absorbed by the liquid.

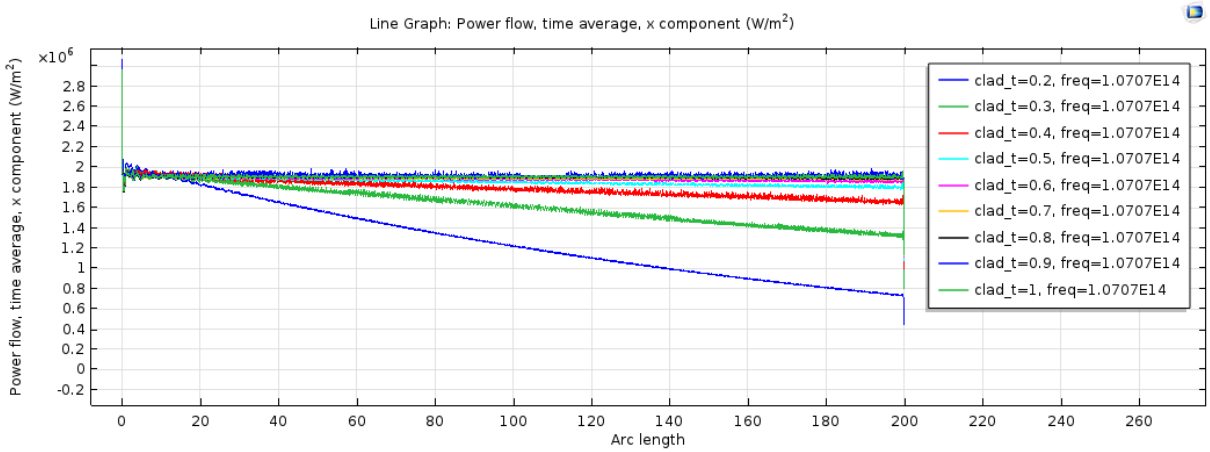

Figure 4.34 Transmitted power of a 200μm cladding without window

Figure 4.35 is the final transmitted power vs. cladding thickness. Above 0.7μm of the thickness, the transmitted power is going to be steady. That is to say a 0.7μm cladding is sufficient.

From Figure 4.34, the power flow values at the end and the beginning are given. So a transmitted power which is the ratio of the power flow velues at the end and the beginning can be calculated. And the equation of abs(ewbe.S21)^2 on the Y axis in Figure 4.35 is the total energy of the light. The values shown in Figure 4.35 are the square values of the transmitted power calculated from Figure 4.34.

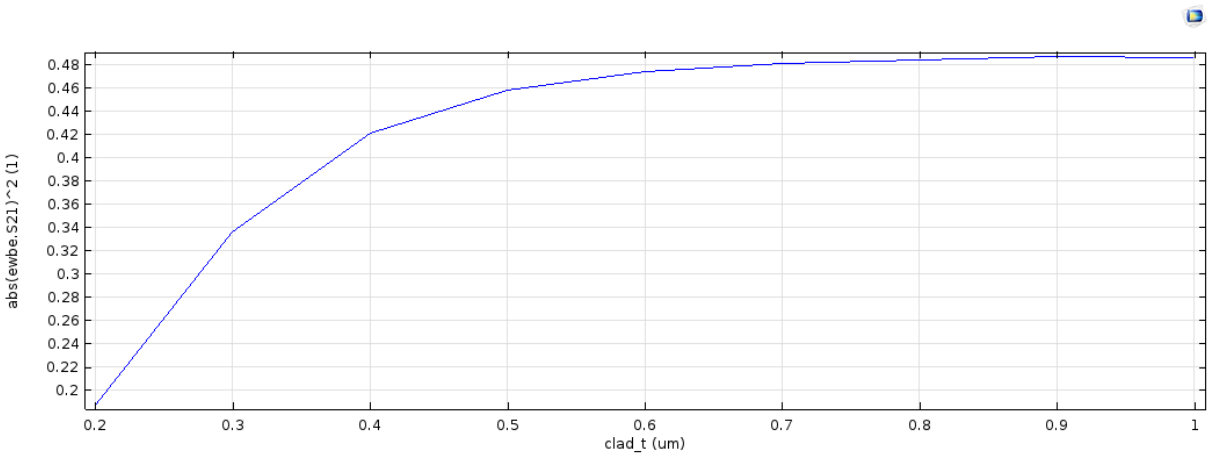

Figure 4.35 Transmitted energy vs. cladding thickness of a 200µm -long cladding without window

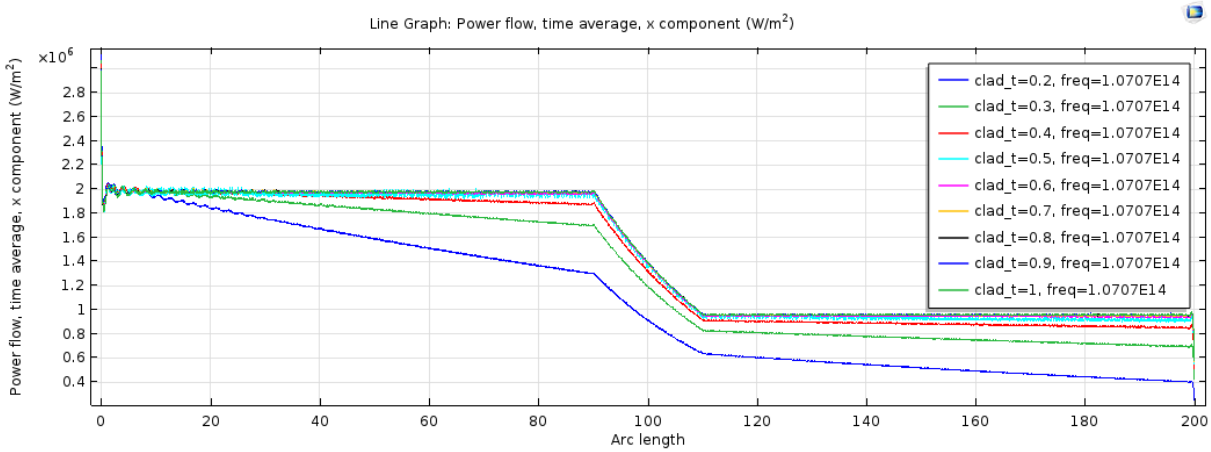

Figure 4.36 Transmitted power of a 200µm cladding with a 20µm window (different thickness)

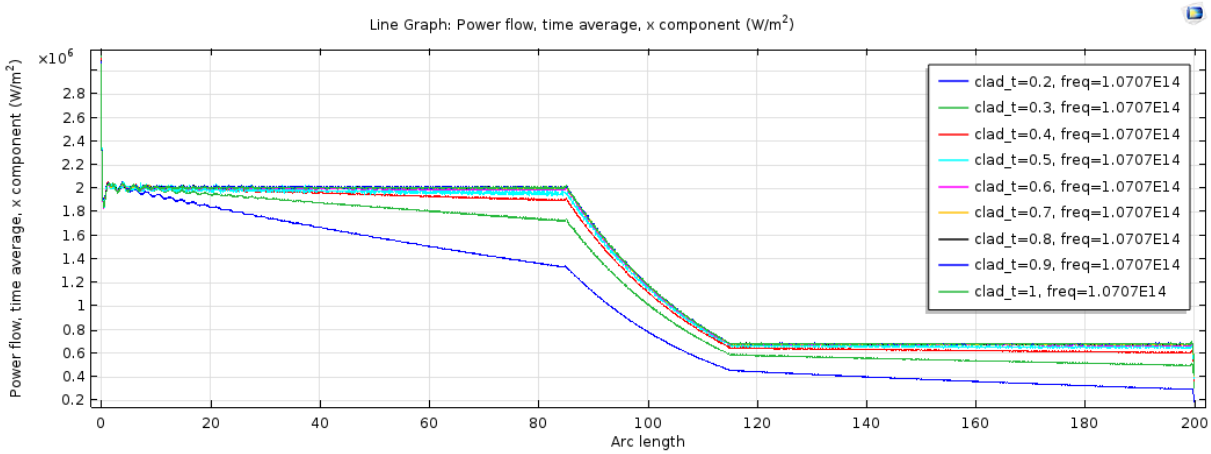

Figure 4.37 Transmitted power of a 200µm cladding with a 30µm window (different thickness)

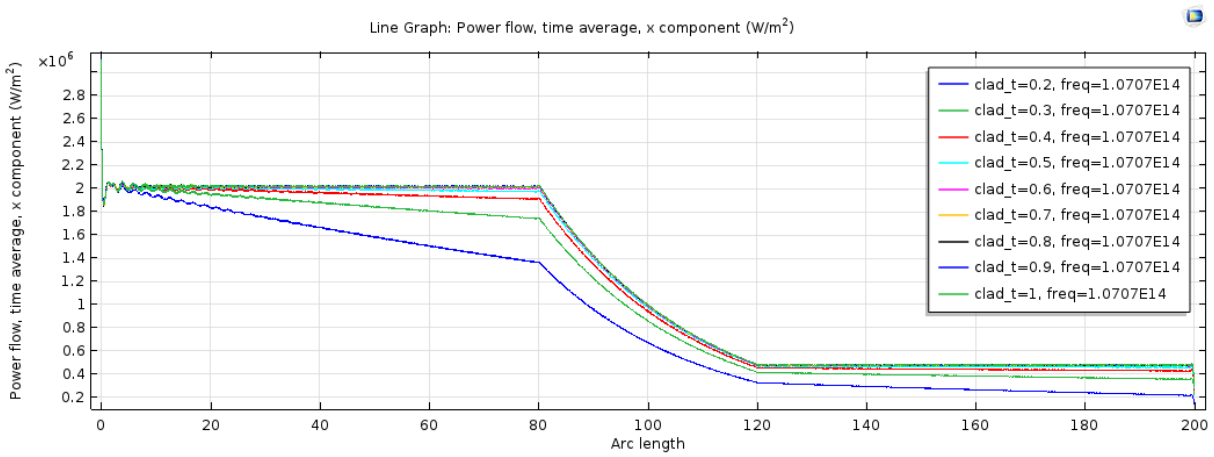

Figure 4.38 Transmitted power of a 200μm cladding with a 40μm window (different thickness)

Figure 4.36, Figure 4.37 and Figure 4.38 show the light's power along the waveguide with a window on the cladding. A conclusion can be drew that a 20μm window is sufficient for this application. Also during the fabrication, different structures with different sizes can be fabricated at the same time.

From Figure 4.36, as can be calculated that the transmitted power is around 40%, compared with the data in Figure 4.27 they are almost the same. Hence, the simulation accuracy of the BeamLab toolbox is almost the same with COMSOL. So a final conclusion of the sizes of the structure can be drew. The values of the final decision are listed in the table below.

Table 4.1 Conclusions about the sizes after the simulations

Range: 2.6μm – 2.8μm	*Values. Unit: μm*
Thickness	0.3
Width	1.0
Window Length	20 – 40

Table 4.2 Comclusions about the sizes after the simulations

Range: 3.5μm – 3.8μm	*Values. Unit: μm*
Thickness	0.4
Width	1.5
Window Length	100 – 200

Table 4.1 and Table 4.2 show the rough decisions of the sizes for the waveguide for each wavelength range. This sizes selection leads to two sets of different structures and we decide to simplify the design and the fabrication, and next section will explain how we simplify the design in detail.

4.4 Final Simulations

From the results of the simulations above, the structures are going to be used for the two ranges will be different. Which means that each structure needs one set of masks to fabricate it. And because of

the different thickness, each structure has to be fabricated seperately. The reason for this is that different thicknesses of poly-silicon have to be deposited seperately.

In order to simplify the fabrication procedure and save masks, in this section, a set of 3D simulations which is carried out by Beamlab Toolbox in MATLAB will be introduced to see if there is common size of srtucture can be used for both wavelength ranges. That is to say, a common size of the structure should be found to be able to guide the two ranges of light.

A great advantage of this toolbox is that the light can be monitored when propagating, so that the reliability of the simulation and modes' mechanism can be judged by people intuitively.

This set of simulations are divided by different sizes and different modes up to the 3rd mode. After doing this, hopefully a common structure can be found. The basic priciple for the simulations is that the structure should only be working for single mode as was discussed in the previous chapter.

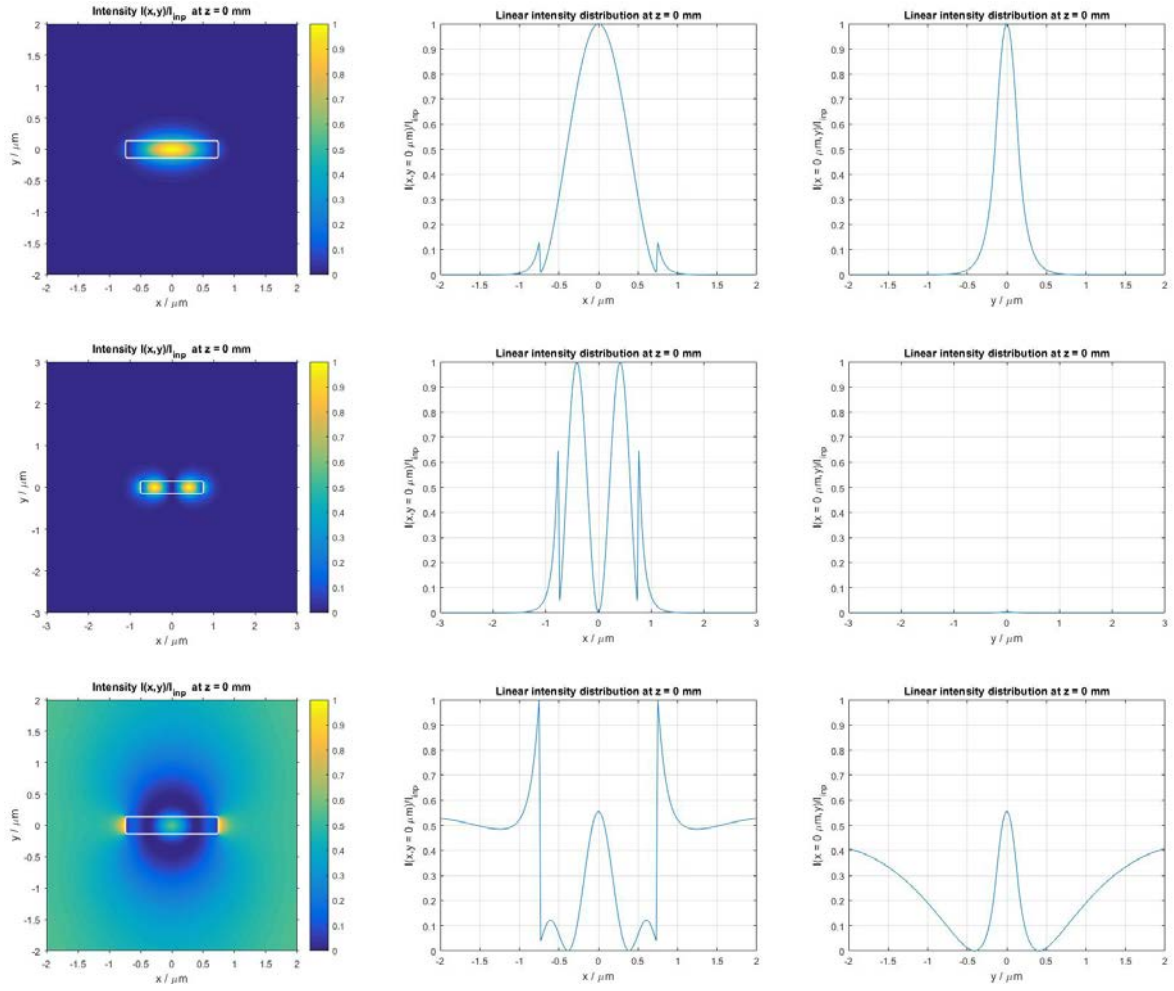

Figure 4.39 Beginning cross-section of TE0, TE1 and TE2 modes of 0.3μm * 1.5μm structure (2.8μm wavelength)

Figure 4.39, Figure 4.40 and Figure 4.41 give the examples of the simulation. The detailed setup of the simulation is that the structure size is set to 0.3μm * 1.5μm * 1000μm. As can be seen from the figures, under this set of sizes, the TE0 mode can propagate in the waveguide without any loss. In the same time, the TE1 is attenuating and the TE2 mode does not propagate at all. That is to say the waveguide with this set of sizes is sufficient for our application.

After analyzing the electrical field graphs at the end of the waveguide, we should be able to find a final structure to ba able to guide the two different wavlength range of light without loss. Also the common structure should be able to guide the basic mode light only.

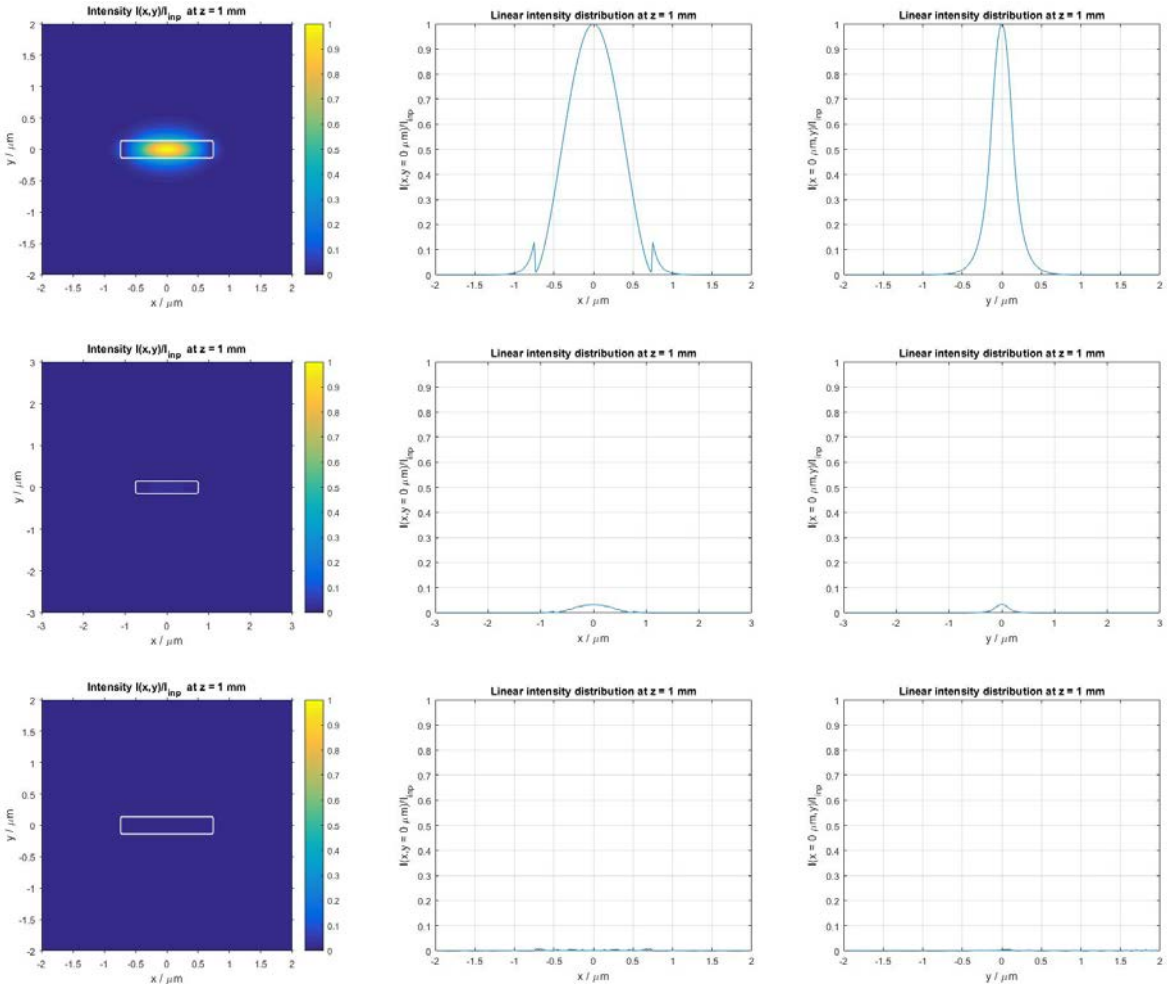

Figure 4.40 End cross-section of TE0, TE1 and TE2 modes of 0.3µm * 1.5µm structure (2.8µm wavelength)

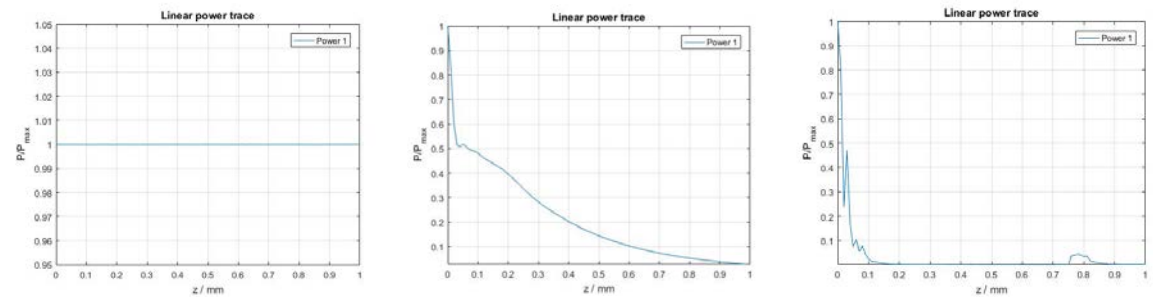

Figure 4.41 Power trace of TE0, TE1 and TE2 modes of 0.3µm * 1.5µm structure (2.8µm wavelength)

The purpose for the simulation is to find a set of structure sizes which is sufficient for both range of wavelength ranges. Which means only selected mode (basic mode) can propagate inside of the waveguide. From the simulation example given by Figure 4.39, Figure 4.40 and Figure 4.41, only TE0 mode light can propagete very steady but the TE1 and TE2 modes can not propagate well.

Then after this a set of simulations are accomplished to see the pattern of light's propagetion, and the thicknesses of the waveguide are set to 0.3μm, 0.35μm and 0.4μm. From Figure 4.42 to Figure 4.47, every small crosssection figure is the figure of electrical field distribution at the end of the waveguide. They show the propagation information of every mode and wavelength range.

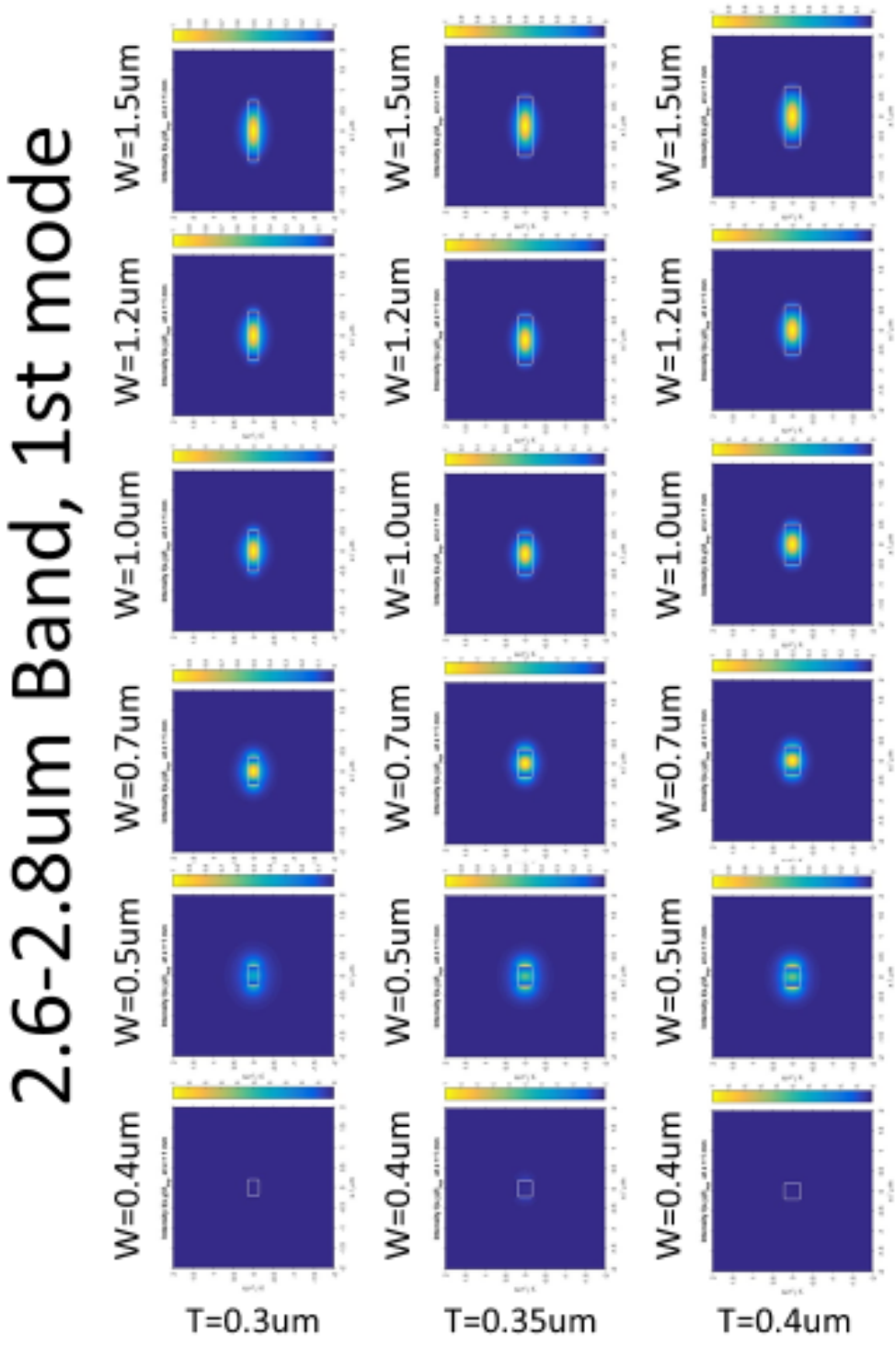

Figure 4.42 TE0 mode ending cross-sections (electrical field distribution)

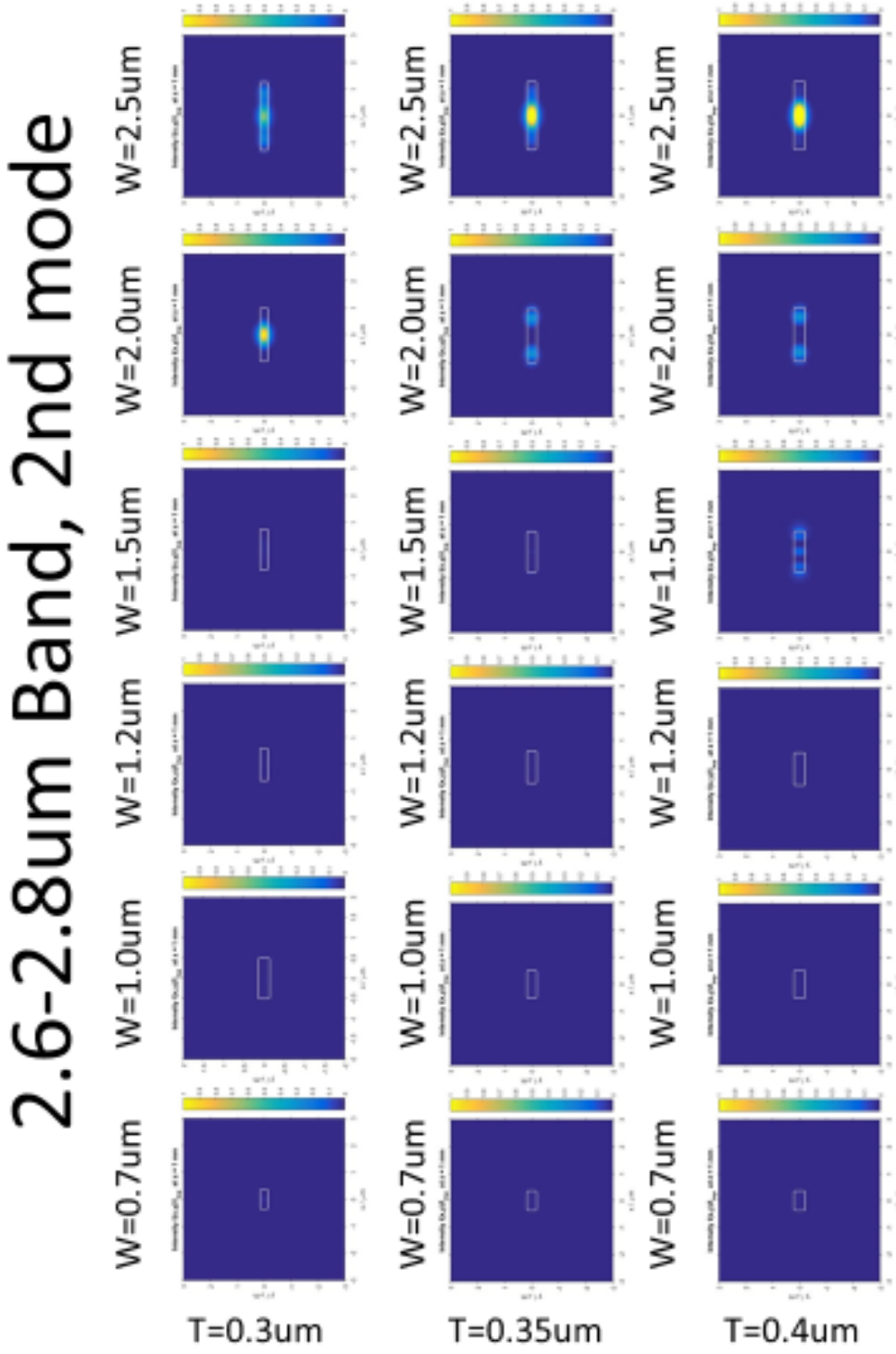

Figure 4.43 TE1 mode ending cross-sections (electrical field distribution)

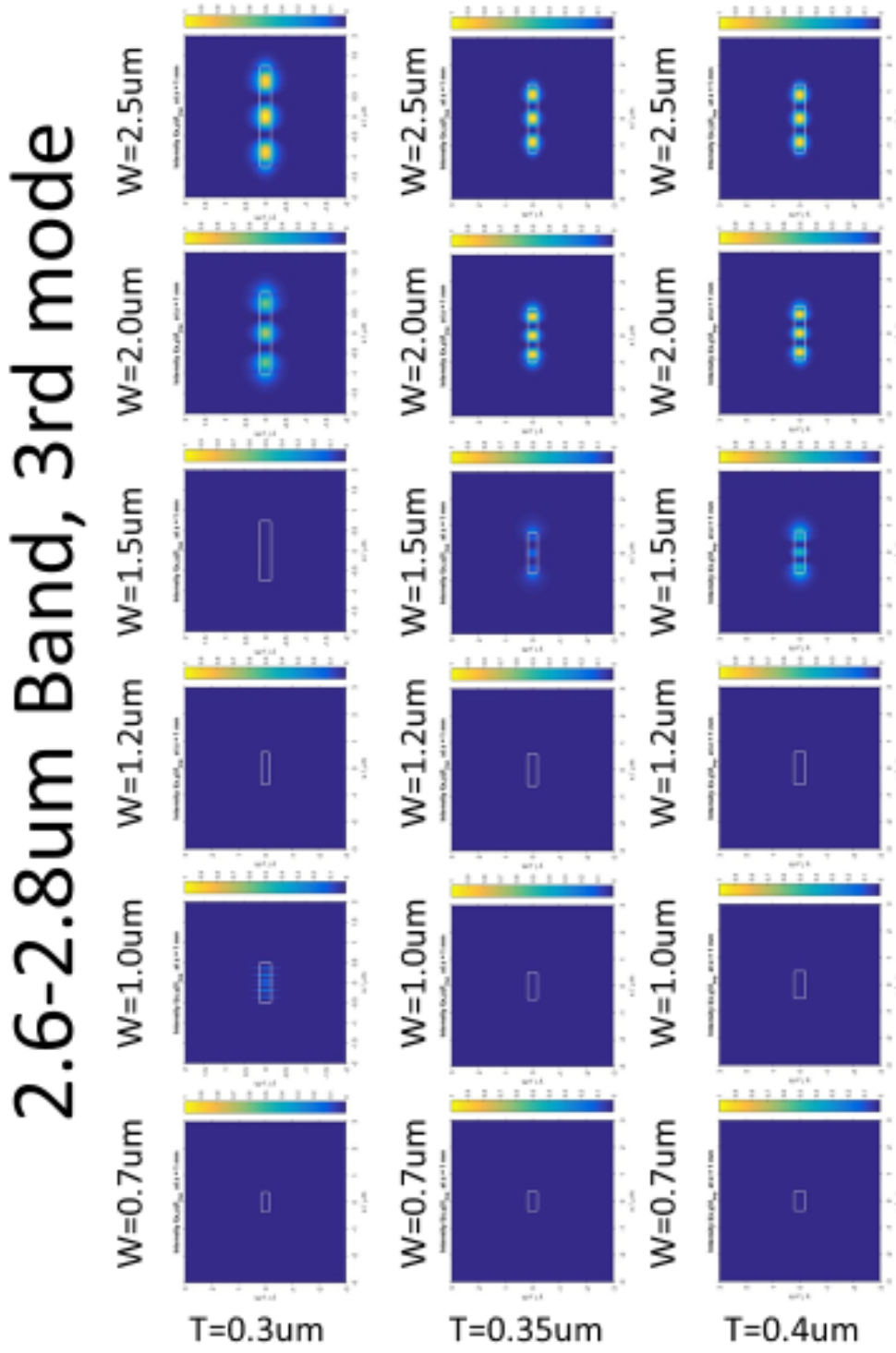

Figure 4.44 TE2 mode ending cross-sections (electrical field distribution)

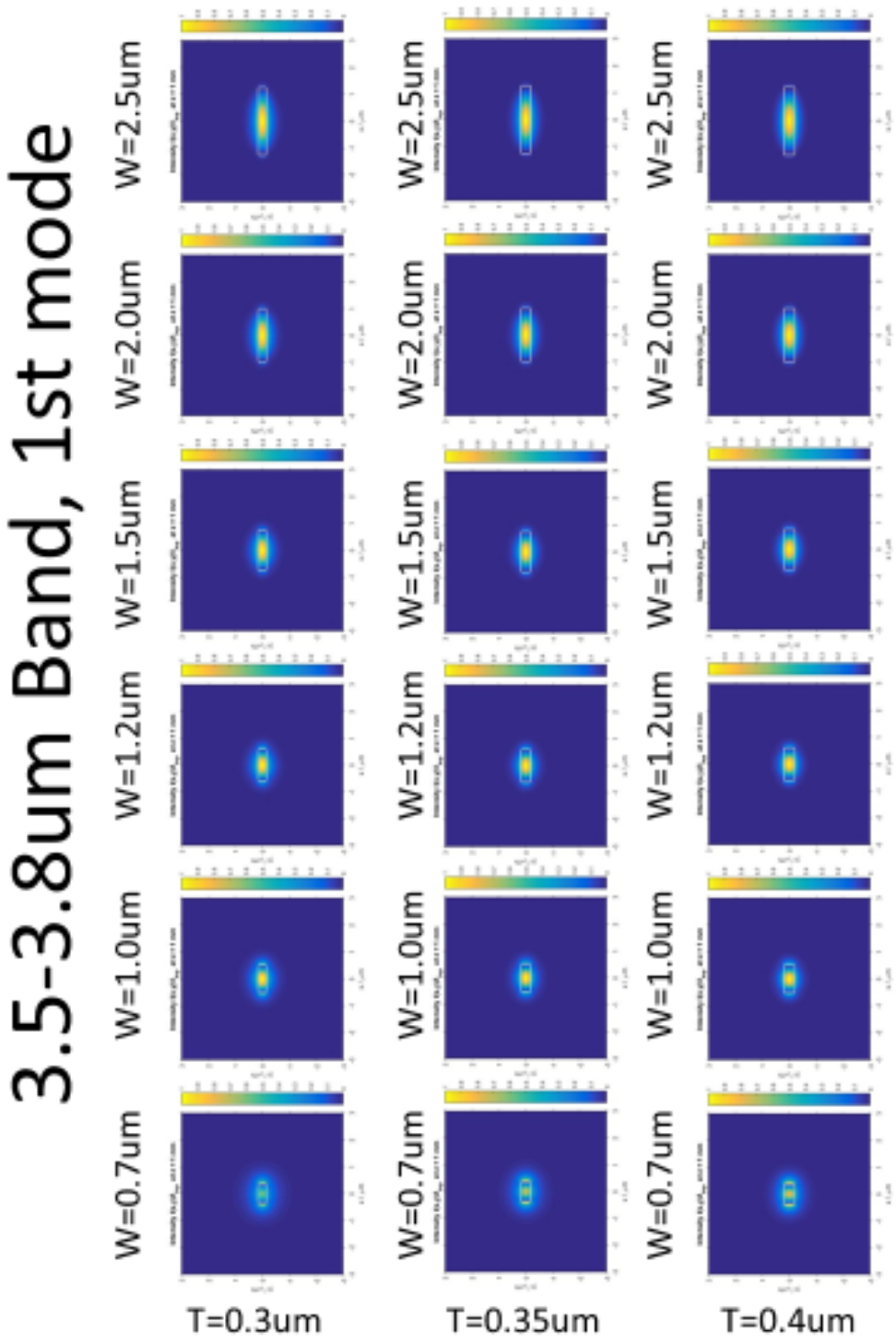

Figure 4.45 TE0 mode ending cross-sections (electrical field distribution)

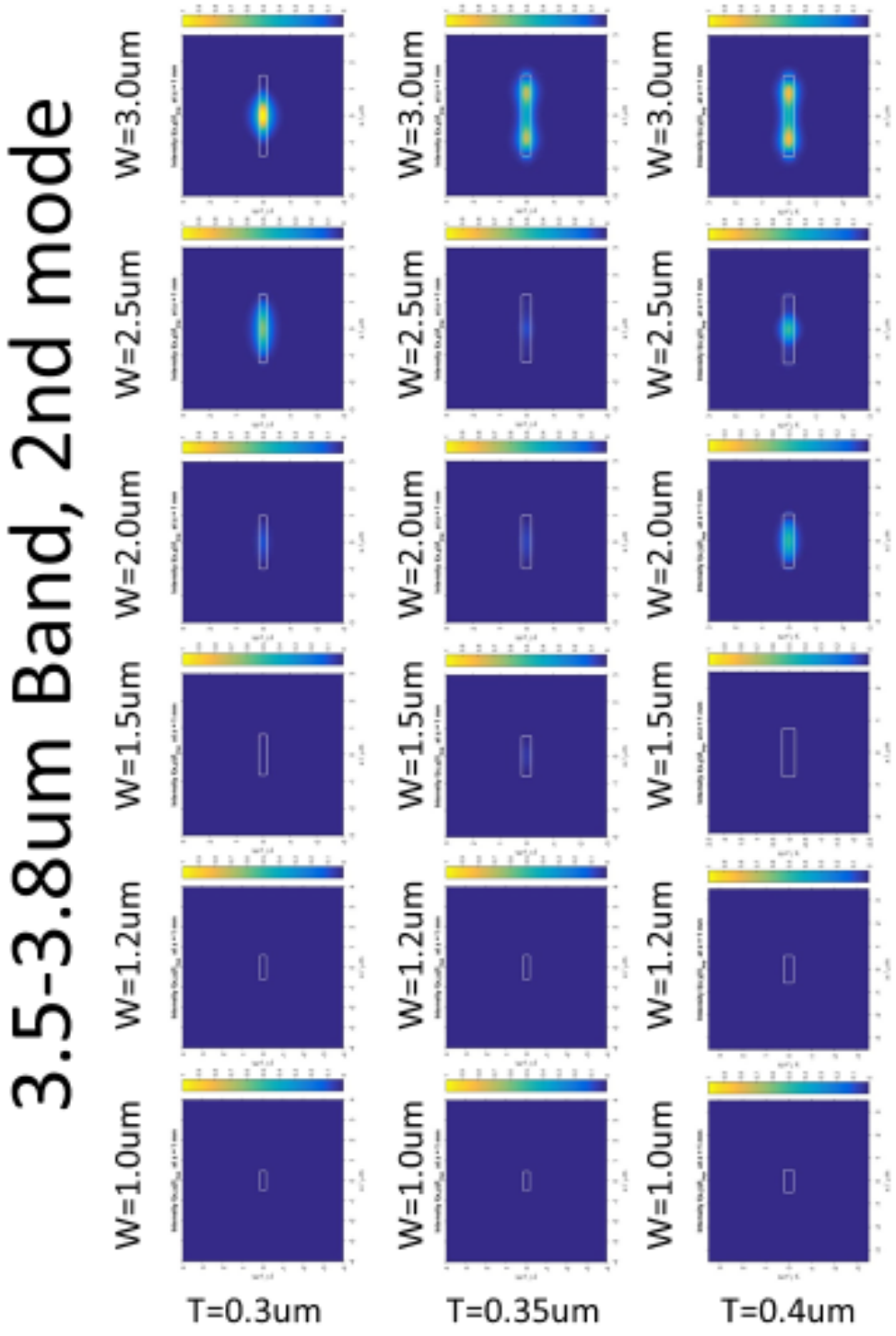

Figure 4.46 TE1 mode ending cross-sections (electrical field distribution)

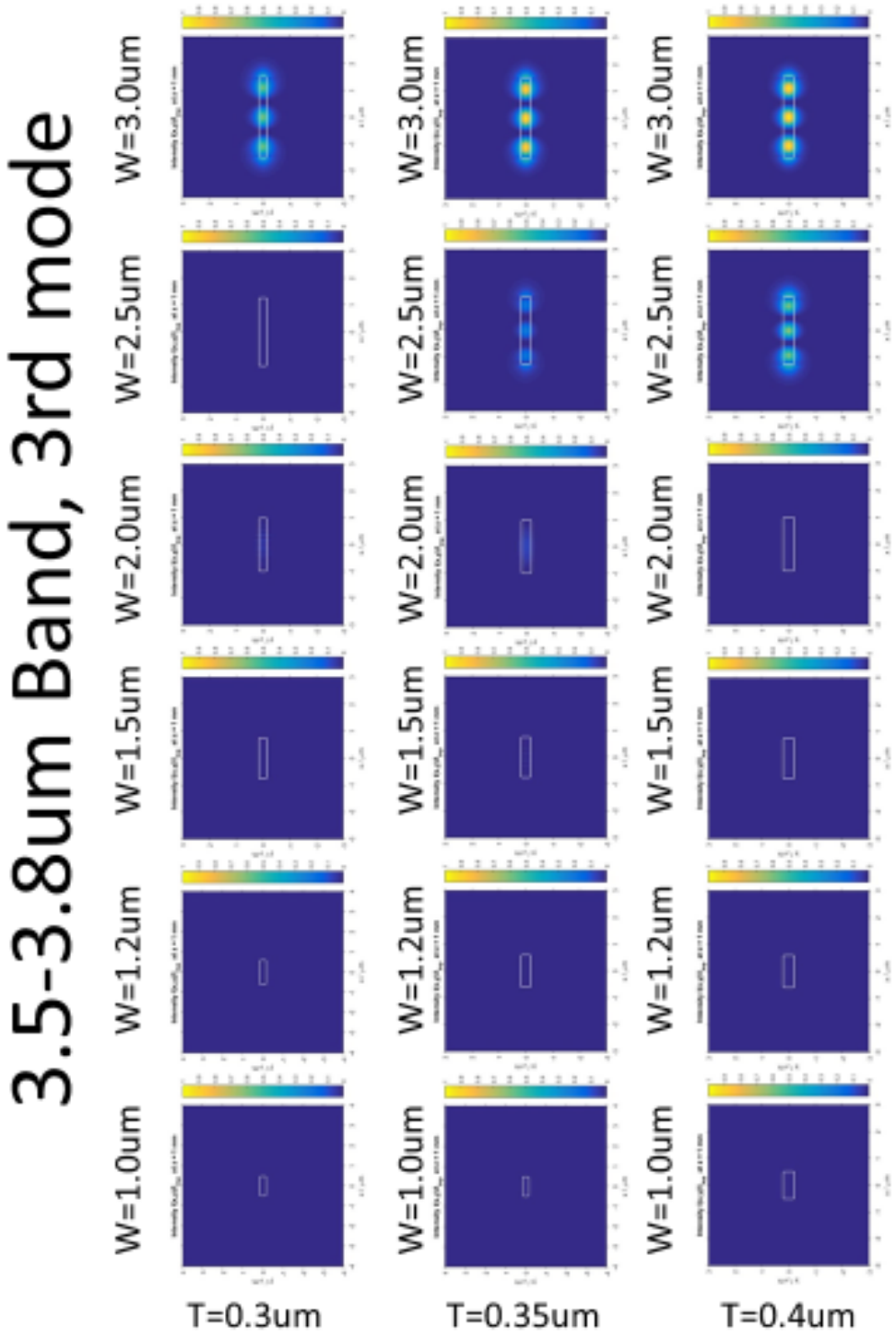

Figure 4.47 TE2 mode ending cross-sections (electrical field distribution)

As a conclusion drew from the figures above, for the first range of wavelength, the first mode is going be propagating steady from width of 0.7μm, the second mode and third mode light are going to propagate from width of 1.5μm. For the second range of wavelength, the first mode is going to

propagate steady from width of 1.0μm, the second mode and third mode light are going to propagate from width of 2.5μm. If a set of common size values can be found in between, the fabrication procedure will be simpified significantly.

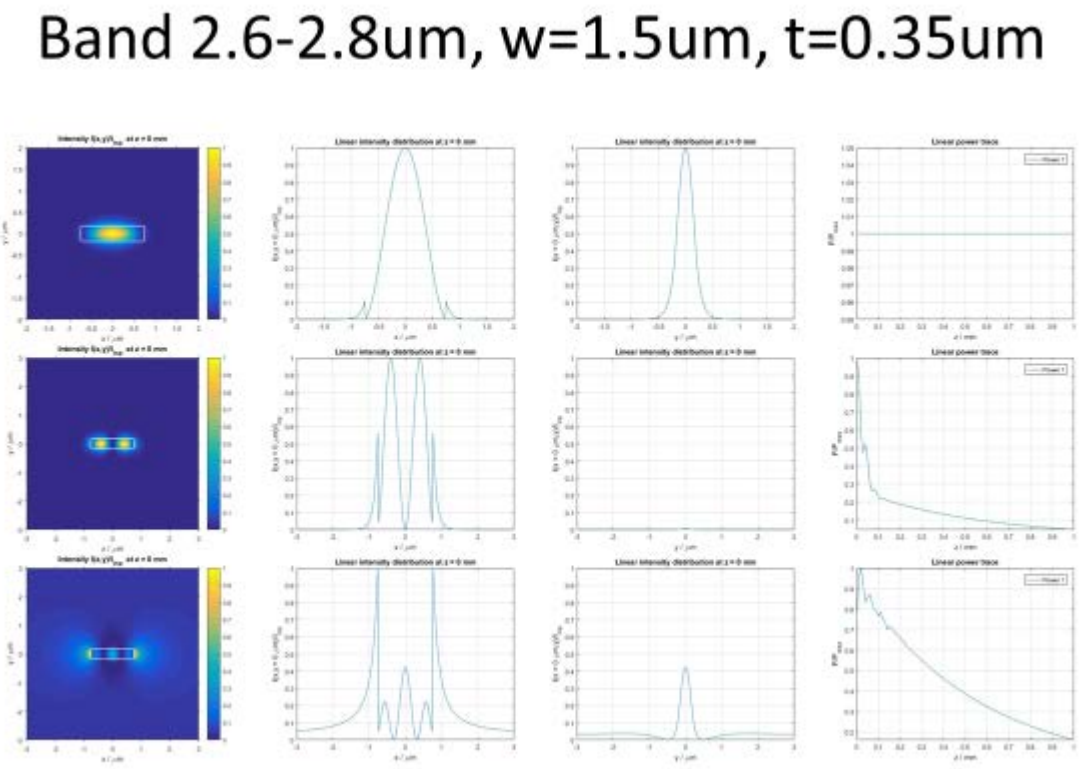

Figure 4.48 Beginning cross-sections (electrical field distribution) and power trace

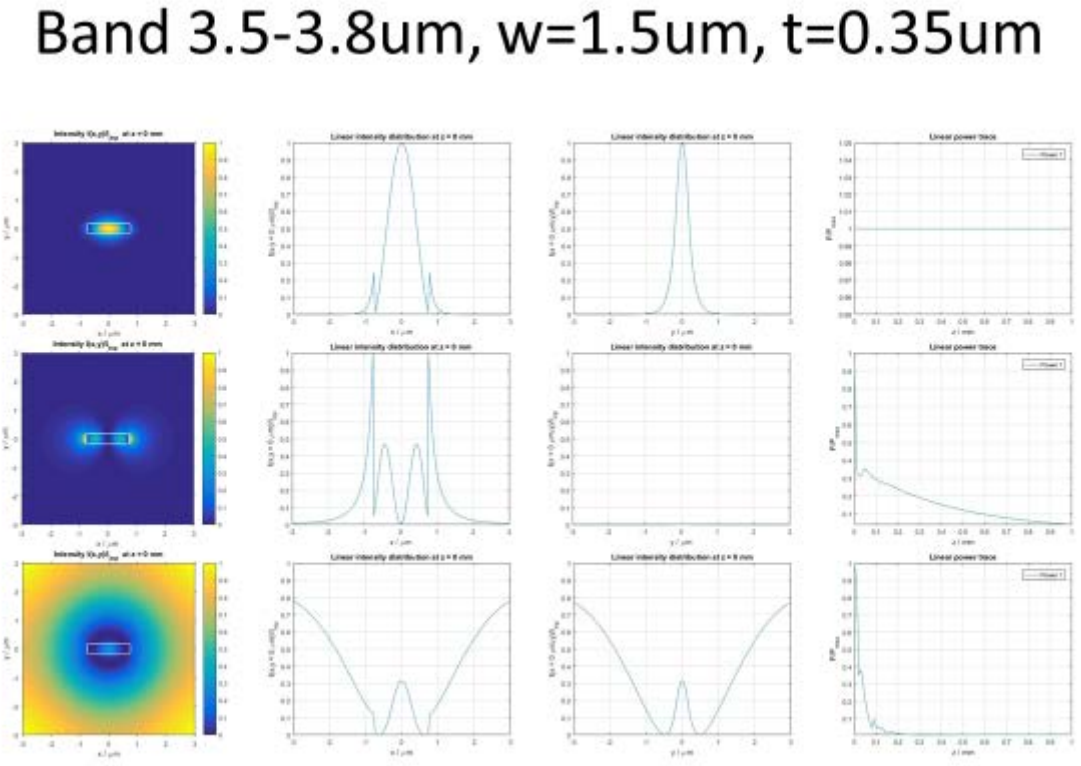

Figure 4.49 Beginning cross-sections (electrical field distribution) and power trace

From the information which is given by Figure 4.48 and Figure 4.49, only TE0 mode light can propagate well inside of the waveguide and higher order modes are not able to propagate.So we decided to select 0.35μm as the thickness value and 1.5μm as the width value. These values will be used to design the main structures. Some additional structures will be added to the chip and this will be explained in the next chapter.

4.5 Remaining Issues

This section will discuss around several possible practical problems. Some additional simulations will be added to explain why the structure like in Figure 3.30 will be used. The problems are:

- Why is a lateral waveguide structure chosen here but not a vertical one?

The reason for using a vertical shaped waveguide is to give more electrical field exposure to the sample, so that a higher absorptance rate can be reached and obviously it is not needed. Like is shown in section 4.3.3, the absorptance is already too high. If a vertical waveguide is applied, that is to say we need to reduce the window length. A smaller window length in practical situation means it is harder to make contact to the sample.

The second reason for not using a vertical structure is that an over 1μm height structure on a silicon oxide layer is hard to fabricate. We need to etch a 1μm wall with a smooth surface.

- Why are the rectangular waveguides of size 0.35μm * 1.5μm are chosen but not some square shaped like 0.3μm * 0.3μm or 1.5μm * 1.5μm?

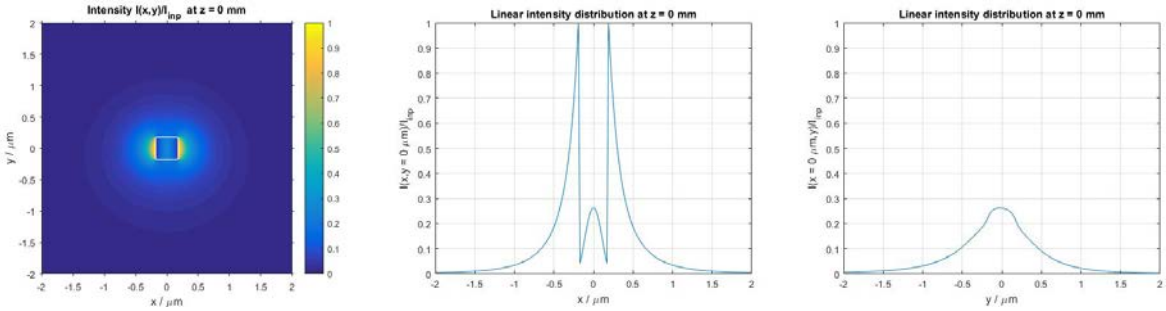

Figure 4.50 Mode shape of TE0, 0.35μm * 0.35μm structure

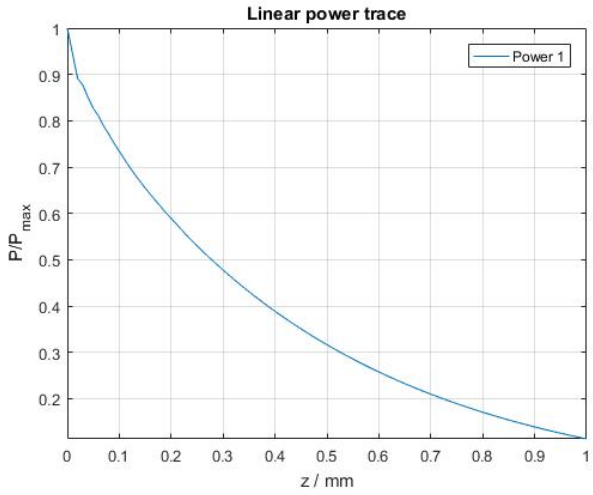

Figure 4.51 Power trace along 1000μm length, 0.35μm * 0.35μm structure

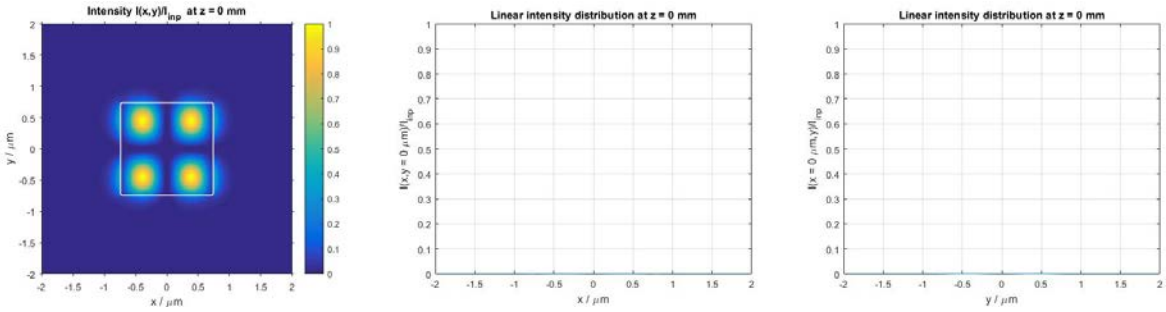

Figure 4.52 Mode shape of TE11, 0.35μm * 0.35μm structure

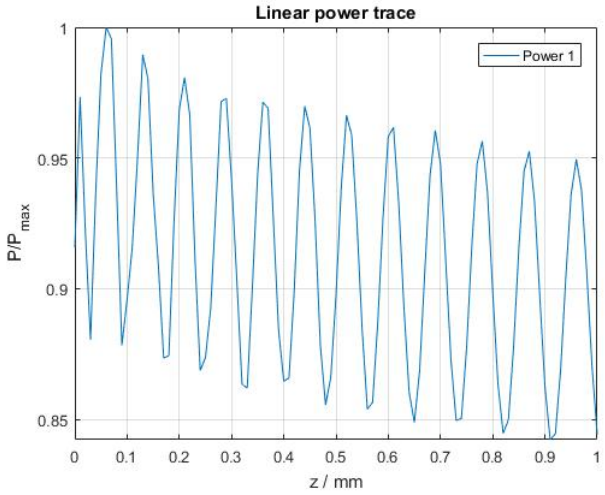

Figure 4.53 Power trace along 1000μm length, 1.5μm * 1.5μm structure

Figure 4.50 and Figure 4.51 show the power trace of the basic mode TE0. That indicates that such a small structure can not permit the basic mode light to propagate. However, meantime Figure 4.52 and Figure 4.53 show that in a 1.5μm * 1.5μm waveguide, the TE11 mode is propagating well.

That is to say firstly the thickness has to be limited to make it a planar waveguide. And then the width of the waveguide can be adjusted to make sure only the basic mode can be guided.

4.6 Coupler Simualtions

A tapered coupler is finally chosen for this application. And the angle for the taper has to be smaller than 1 degree. After a short calculation, the total length of the coupler has to be larger than 500μm. That is to say COMSOL is not capable to simulate this structure because this structure is too large. That will consume months to simulate it. So here the BeamLab toolbox will be used to simulate the coupler.

The coupler connects the waveguide with the fiber. The available commercial fibers which is used to guide single mode mid-infrared light have a core size around 10μm. The tapered coupler is actually acting as a mode size converter, as shown in Figure 4.54 to Figure 4.57, the mode size is converted to a smaller size after it goes through the coupler.

Note that all the simulations are set as: 10μm * 10μm (begin) to 0.35μm * 1.5μm (end). Only the length of the waveguide is changed.

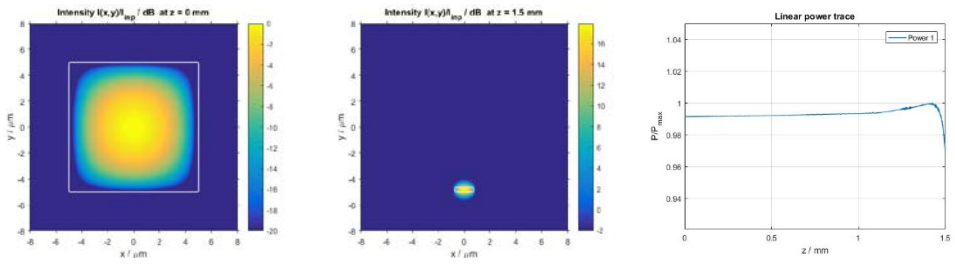

Figure 4.54 Begin and end of the coupler, and power trace (1500μm)

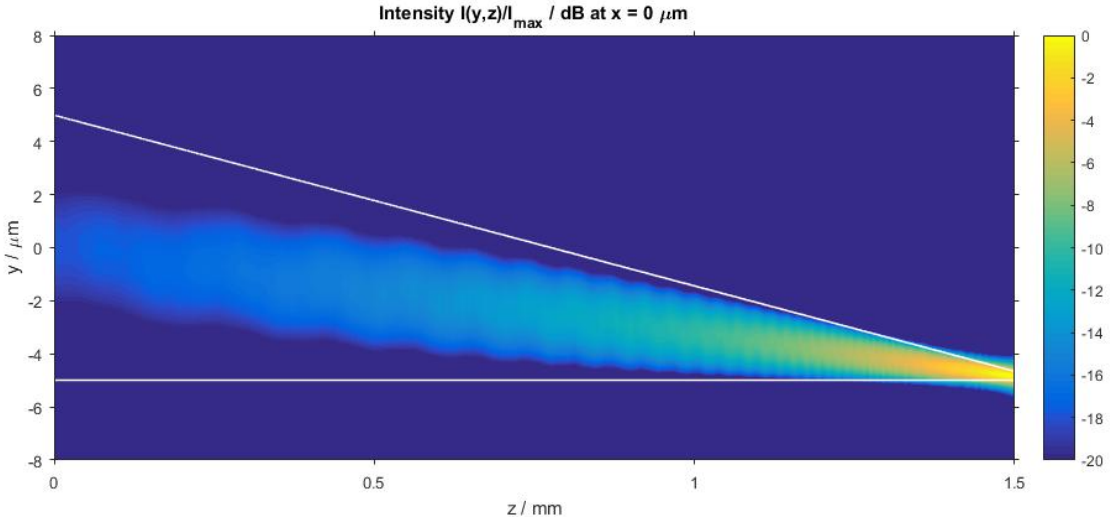

Figure 4.55 Side cross-section of the coupler (1500μm)

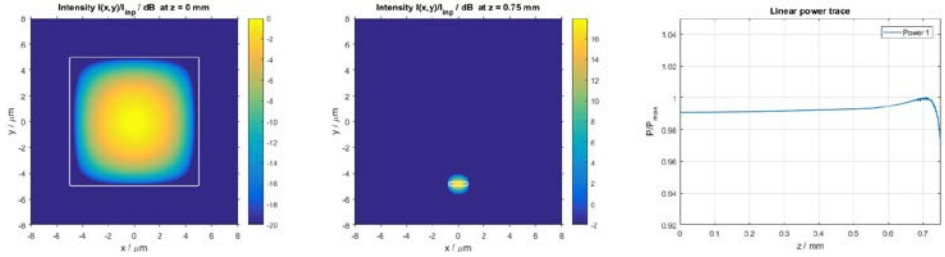

Figure 4.56 Begin and end of the coupler, and power trace (750μm)

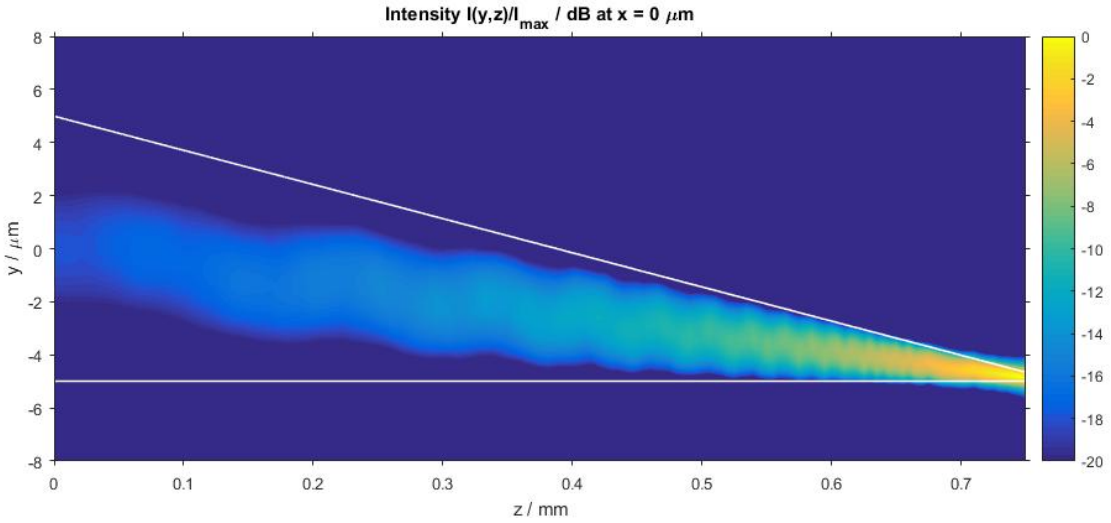

Figure 4.57 Side cross-section of the coupler (750μm)

Figure 4.58, Figure 4.59, Figure 4.60 and Figure 4.61 are the power trace and cross-sections of length of 100μm and 50μm. When the length of the coupler becomes shorter to 100μm or 50μm, the angle of the taper becomes larger. Then the coupling efficiency becomes lower.

The power trace figures in Figure 4.58 and Figure 4.60 show that at the end of the coupler, there is lot of light leaking. And Figure 4.59 and Figure 4.61 show the leaking of light more intuitively.

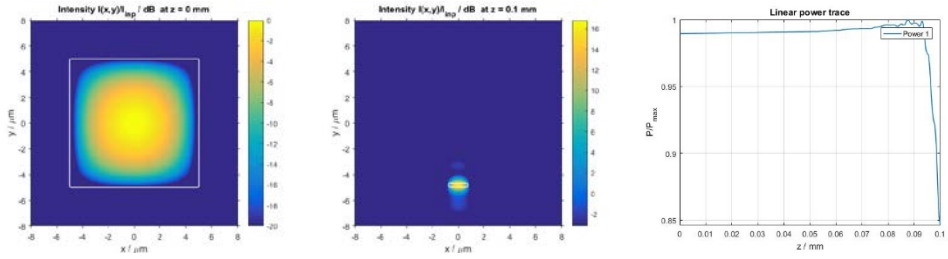

Figure 4.58 Begin and end of the coupler, and power trace (100µm)

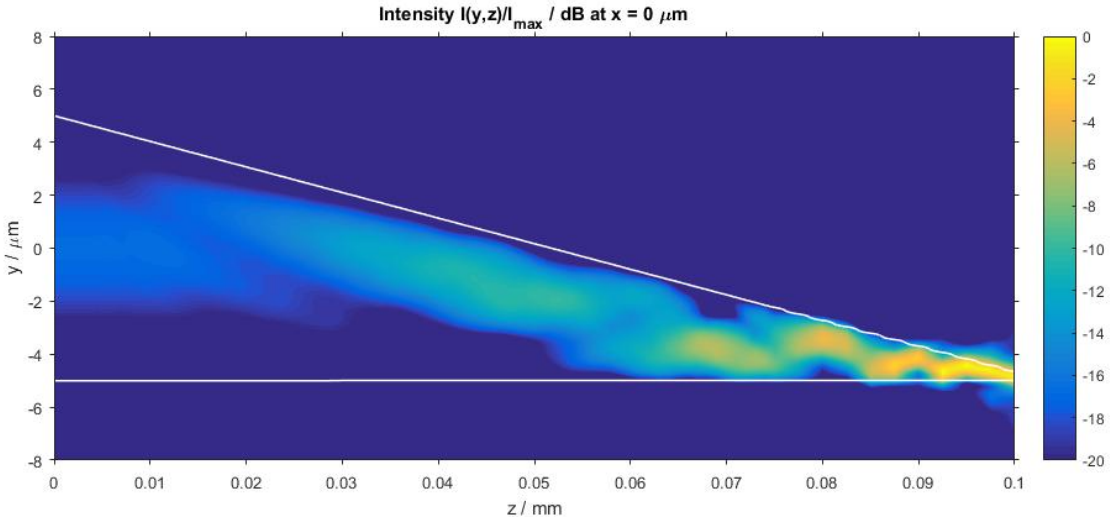

Figure 4.59 Side cross-section of the coupler (100µm)

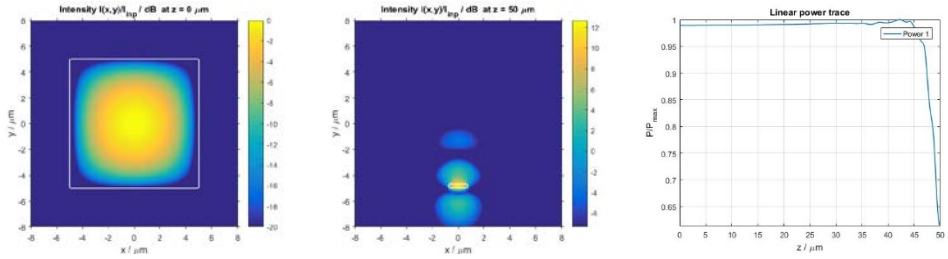

Figure 4.60 Begin and end of the coupler, and power trace (50µm)

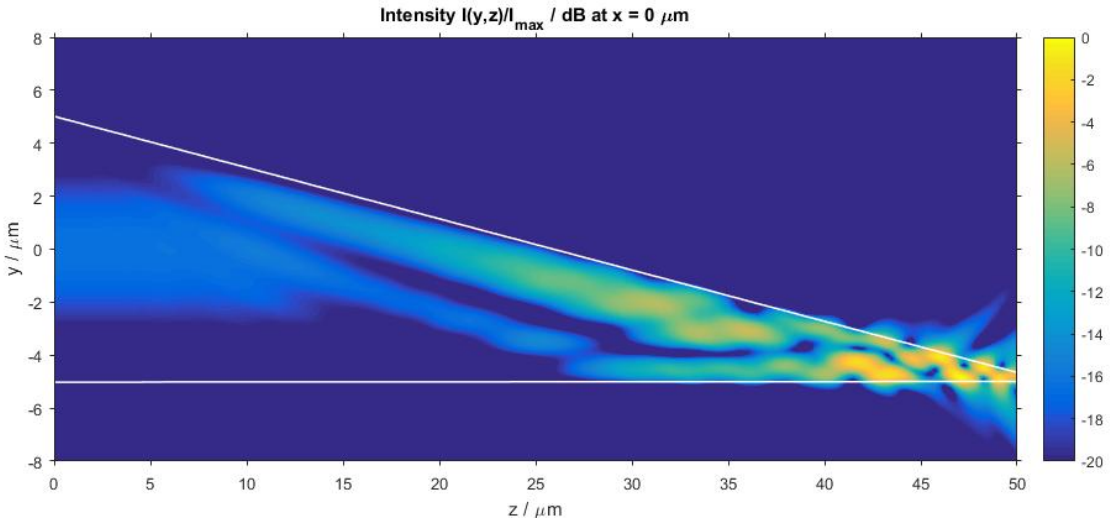

Figure 4.61 Side cross-section of the coupler (50μm)

In our application, we have enough chip area to build a large coupler. In order to gain a high coupling efficiency. We decided to used two kinds of coupler: 1500μm long and 750μm long.

4.7 Conclusion

After the final simulation, we found that we can use a single structure to guide two ranges of light. And the size of the wavelength core can be roughly confirmed as 1.5μm * 0.35μm at the cross-section. But some waveguides of other sizes are wtill needed because we want to see how the light will perform under different conditions.

Also the length of the tapered coupler is also simulated, we would like to try 1500μm and 750μm long coupler.

Chapter 5. Layout Design and Fabrication

Two sets of masks are designed for the two sets of structures. The masks are drawn with L-Edit.

5.1 Parameters Setups for the Structures and Layout

In the previous chapters, the waveguide itself has already been detailed discussed. The only thing we need to finalize the mask is the commercial fiber's size. After we get the size of the fiber, the size of the groove can be finalized.

In our design, the coupler is tapered in two directions, i.e. both the thickness and width of the coupler tapered over the length of the coupler. The initial cross-sectional area of the coupler is selected based on the available mid-infrared optical fiber on the market. After some search on the websites, we found that the single mode fibers to which can be used in the mid-infrared range all have a core size around 9μm.

For this application, a single mode ZrF4 Fiber Patch Cable (Thorlabs, P1-23Z-FC-1), with a transmission band over 2.3μm - 4.1μm range is selected. Figure 5.1 is the fiber's attenuation information. The fiber has a cladding size of 125μm which is reasonable to build a groove for it. This fiber has a core diameter of 9±0.5 μm and a total diameter of about 125μm. Therefore, an initial area coupler area of 10μm * 10μm was selected here.

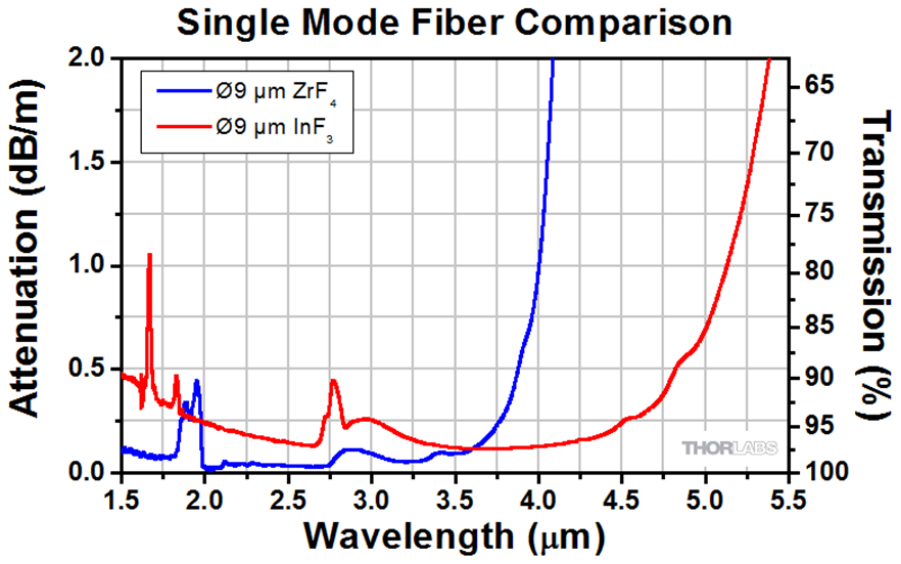

Figure 5.1 The transmission band of ZrF4 fiber (Thorlabs, P1-23Z-FC-1). The figure is adapted from Thorlabs.com

The masks can be devided into several parts: coupler, waveguide, the window on the waveguide and the grooves to contact the fiber. Based on the simulation results and also the size of the mask, the sizes of coupler and waveguide can be certained. The total area of the mask is 10mm * 10mm, and at

the two sides of the chip, a 2-mm-long groove area has to be saved. As a consequence, the total length of the waveguide itself is fixed as 6mm.

Two lengths of the coupler are designed as simulated in the previous chapter: 750μm and 1500μm. For each set of the sensor, a reference sensor is designed which means without a window on the waveguide. The tapered coupler is designed slightly larger than the fiber's core size as 10μm in case there might be some mismatch between the fiber and the coupler. Two additional sensors which are S shaped and U shaped are designed. For each range, ten structures in total are designed. For every coupler, a 400μm -length area is saved for the groove for calibration. As for the windows, 50μm, 100μm and 200μm windows in length are placed on the waveguide. Considering the issue of the contact efficiency between the liquid and the poly-silicon under the window, the width of the window are designed as 200μm which is relatively larger than the length. When designing the S shaped and U shaped waveguide, the semidiameter of the corner are designed as 50μm to make sure the light will propagate properly. As a summury, the masks can be designed as specified as from the table below:

Table 5.1 Layout sequence

Range 2.6μm – 2.8μm, W: width, L: length, H: height. Unit: μm

Sequence	Coupler begin, W*H	Coupler end, W*H	Coupler Length	Waveguide, W*L*H	Window, L*W
Set 1 Ref ①	10*10	1.5*0.35	750	1.5*4500*0.35	No_window
②	10*10	1.5*0.35	750	1.5*4500*0.35	100*200
③	10*10	1.5*0.35	750	1.5*4500*0.35	200*200
Ref ④	10*10	2.0*0.35	750	2.0*4500*0.35	No_window
⑤	10*10	2.0*0.35	750	2.0*4500*0.35	100*200
⑥	10*10	2.0*0.35	750	2.0*4500*0.35	200*200
Ref ⑦	10*10	1.2*0.35	750	1.2*4500*0.35	No_window
⑧	10*10	1.2*0.35	750	1.2*4500*0.35	50*200
⑨	10*10	1.2*0.35	750	1.2*4500*0.35	200*200
Set 2 Ref ①	10*10	1.5*0.35	1500	1.5*3000*0.35	No_window
②	10*10	1.5*0.35	1500	1.5*3000*0.35	100*200
③	10*10	1.5*0.35	1500	1.5*3000*0.35	200*200
Ref ④	10*10	2.0*0.35	1500	2.0*3000*0.35	No_window
⑤	10*10	2.0*0.35	1500	2.0*3000*0.35	100*200
⑥	10*10	2.0*0.35	1500	2.0*3000*0.35	200*200
Ref ⑦	10*10	1.2*0.35	1500	1.2*3000*0.35	No_window
⑧	10*10	1.2*0.35	1500	1.2*3000*0.35	50*200
⑨	10*10	1.2*0.35	1500	1.2*3000*0.35	200*200
S shaped	10*10	1.5*0.35	1500	1.5*3000*0.35	No_window
U shaped ①	10*10	1.5*0.35	1500	1.5*3000*0.35	No_window

U shaped ②	10*10	1.5*0.35	750	1.5*50*0.35	All_window

Notice that all the height values are the same things with the thickness values and have no influences on the masks. The thickness can be adjusted during the fabrication process. U shaped 2 structure with an all exposed waveguide is designed to test.

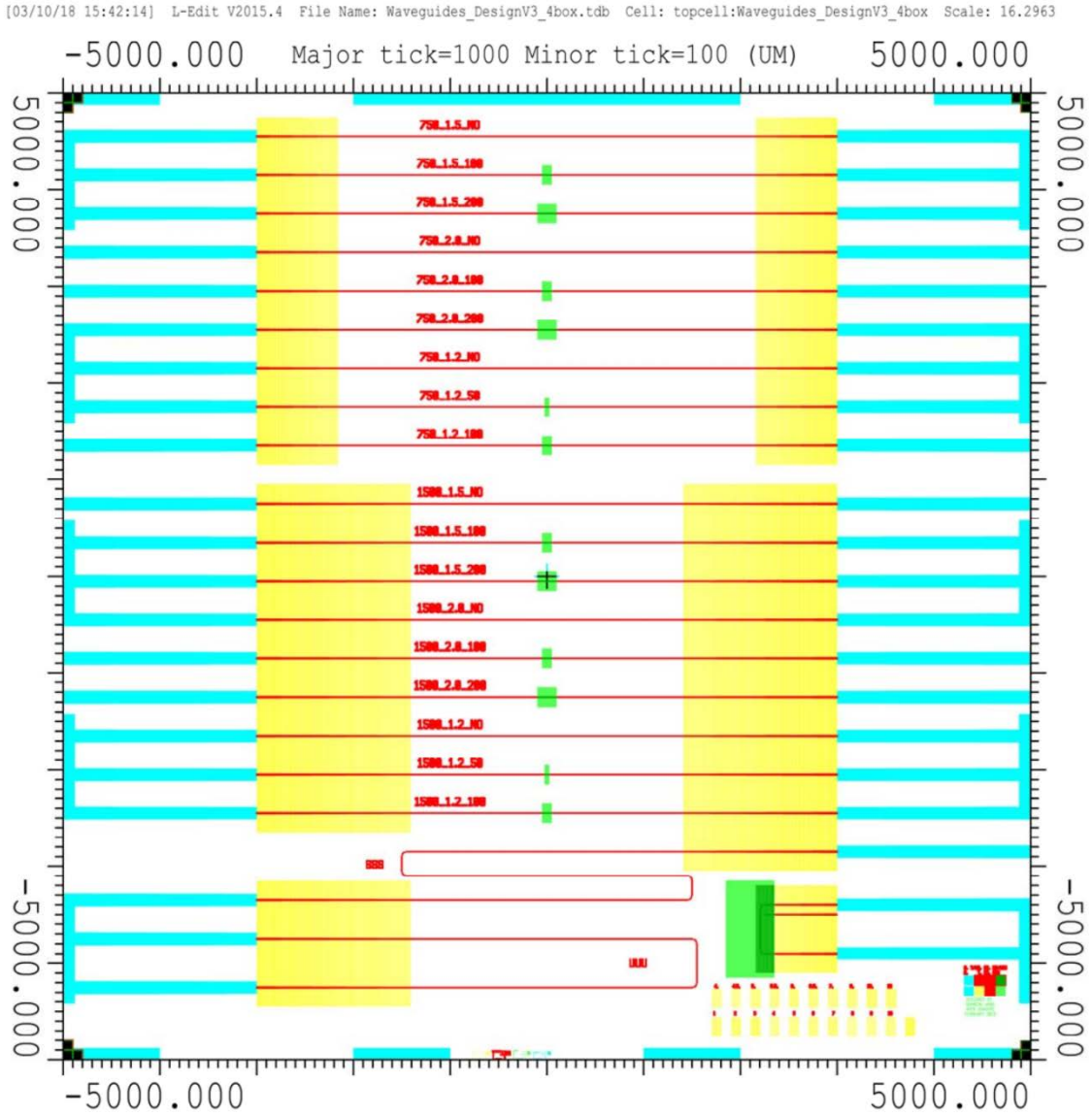

Figure 5.2 Layout of the masks

Figure 5.2 shows the layout of the masks, and there are four colours which stand for four different masks: red, blue, yellow and green. Red layer is for the waveguides and couplers. Blue layer is for the grooves to put the fiber in and the grooves to help us to tear the chips apart. Green layer is for the windows. And the yellow one is for the tapers. These will be explained in the next section.

5.2 Fabrication of the waveguide-based liquid sensors

The fabrication process of this evanescent waveguide sensors with integrated couplers (tapered coupler) was designed with a silicon-based surface micromachining technology. Silicon-based waveguides for infrared light are commonly fabricated on SOI (Silicon-on-Insulator) wafers, where the waveguide is fabricated in the top silicon layer. The buried oxide box acts as the bottom cladding for the waveguide. Furthermore, the crystalline silicon layer ensures a low propagation attenuation in the waveguide.

The coupler's beginning height is designed as 10μm, however, the end the coupler which will be connected to the waveguide is around 0.35μm height. These sizes ensure that the coupler will be contacted with the fiber with a lower lost and the light will be well coupled into the thin waveguide.

Although the top silicon layer provides an excellent platform for the waveguides, the fabrication of the integrated couplers with a thickness of about 28 times of that of the waveguide, as is required here, is challenging. A possible solution is to selectively grow silicon using epitaxy over the coupler area. We have used a polysilicon-based technology for the fabrication of the low-cost waveguides in this research. The longer operating wavelength in the mid-infrared waveguide decreases the propagation loss due to the scattering of the light at the grain boundaries of the polysilicon layer compared to the common near- and short-infrared waveguides. Therefore, polysilicon processing could be used as a suitable and low-cost substitute for the SOI wafers.

Prime silicon wafers (4-inch, p-type, 100) were used as the substrate for the fabrication of the waveguides, with the waveguide and couplers fabricated in an additive process. A thermal oxide layer with a thickness of 1μm is grown at 1100^{o}C as the bottom cladding, and 100 nm polysilicon layer is deposited using LPCVD (low-pressure chemical vapor deposition). This polysilicon layer acts as the seed layer for the epitaxial growth of the 10μm polysilicon layer. The thickness of this layer is selected equal to the thickness of the couplers. Figure 5.3 shows the schematic of the layers on the wafer top side. Note that here we do not show the layers on the wafer backside.

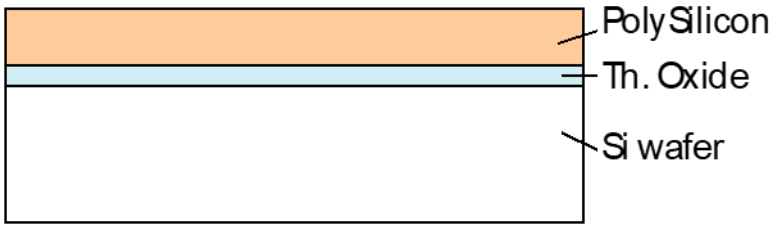

Figure 5.3 The layer stack grown on the silicon wafers used as the basis of the fabrication process

Tapering of the thickness of the coupler layer is achieved using resist reflow and transfer etch technique [1-3]. In this method, a specially patterned photoresist layer is produced and reflown in a thermal and chemical environment. Depending on the pattern, specifically the density of the trenches in the bulk photoresist, a smooth and patterned-controlled thickness variation of the photoresist layer is achieved. shows the schematic of the photoresist pattern, composed of an array of fixed-sized trenches in a resist layer, and the reflown structure. A layer of 9μm thick photoresist layer (AZ 9260) is spin-coated and an array of 4μm thick trenches is patterned using wafer stepper.

The reflow was done in PGMEA vapor at 70 °C for 1 hour. This results in a tapering of 9μm to 4μm over the length of the coupler, i.e. 750μm and 1500μm for the two different designs.

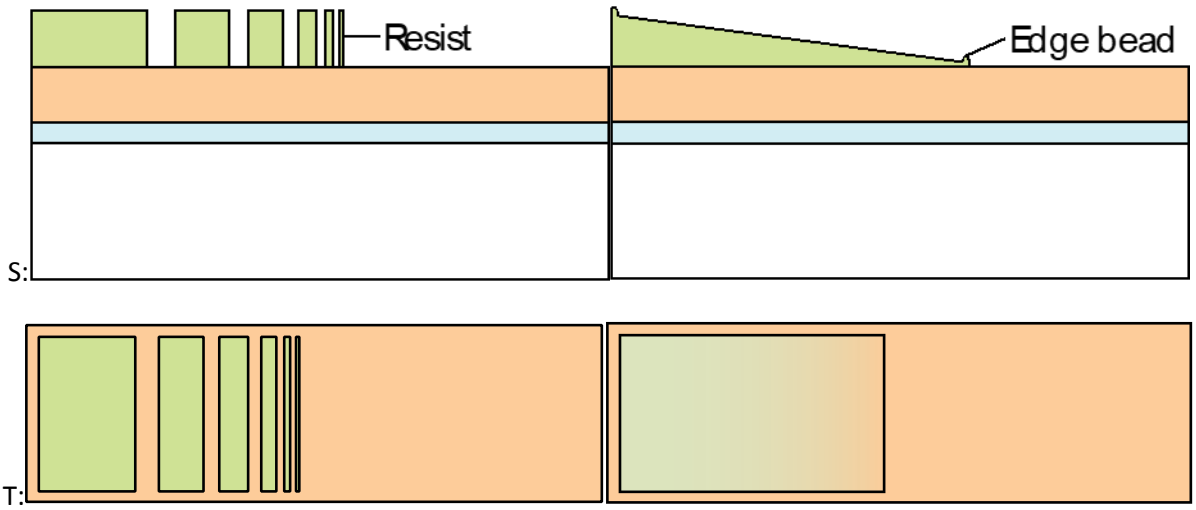

Figure 5.4 Side and top view of the patterned resist layer, and after reflow

The fabricated tapered layer is then transferred into the polysilicon layer using a specific etch rate ratio. Here we have used a 1:2 transfer ratio of resist to polysilicon to obtain the tapered polysilicon coupler. It should be noted that the reflown resist usually result in an edge bead at the corners of the structure, as shown in Figure 5.4. Therefore, the couplers were designed to be 100μm longer than the nominal design and an isotropic etch step with high selectivity to oxide is then used to decrease the effect of the edge bead. Figure 5.5 shows the structure after the transfer etch into the polysilicon layer. This will be explained further later.

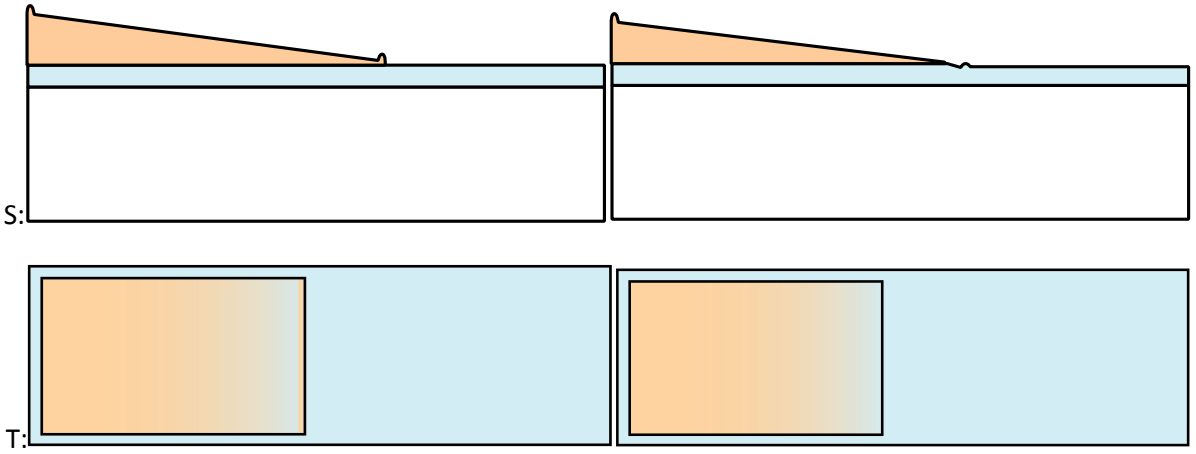

Figure 5.5 The transfer etching of the resist layer into polysilicon, and the isotropic etch step to remove the edge beads

In the next step, the waveguide layer is added. Any interface between the coupler and the waveguide results in reflectance at the coupler-waveguide interface and significantly reduces the coupling efficiency. Therefore, the wafers were cleaned using Marangoni cleaning to remove the native oxide on the polysilicon layer. Next, a polysilicon layer is deposited using LPCVD with a thickness of 400nm which is the thickness of the waveguide layer. Since the taper was also fabricated based on the polysilicon seed layer, the interface between the coupler and this secondary polysilicon layer is avoided. Therefore, the coupling loss between the coupler and waveguide reduces. Figure 5.6 shows

the schematics of this step, and Figure 5.7 shows a close-up of the junction between the waveguide and coupler. It can be seen that the bump caused by the photoresist edge bead can result in a non-ideal junction between the coupler and waveguide. This effect can be greatly suppressed by using a selective-enough isotropic etch step as was discussed above.

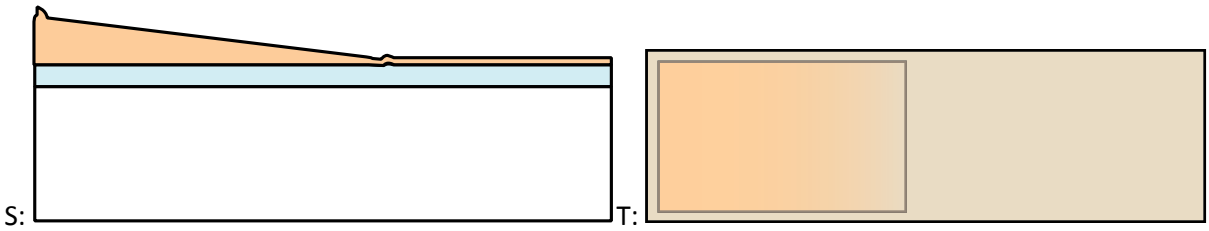

Figure 5.6 The schematics of the structure after the deposition of LPCVD polysilicon over the wafer

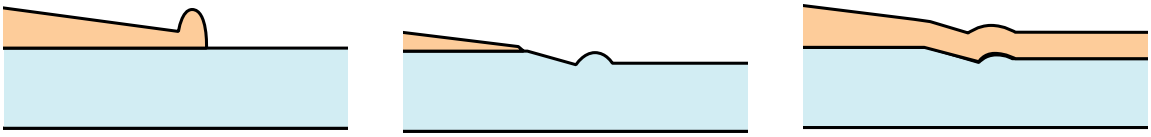

Figure 5.7 Close-up of the coupler to waveguide junction: The effect of the edge bead on the junction

In the next step, the coupler and waveguide are patterned in a single lithography step. This single patterning step eliminates any misalignment between the coupler and waveguide. In this step, the width of the waveguide is also tapered from 10μm down to the designed waveguide width. The large step height difference between 10μm thick tapered couplers and 0.35μm waveguides makes the coating and patterning of the photoresist layer cumbersome. In this step, a 4μm photoresist layer (AZ9260) is spray coated on the surface and patterned in wafer stepper with the focus on the waveguide layer to ensure that the waveguide width is achieved with the highest accuracy.

A selective and directional etch step is then required to etch both 10μm and 0.4μm polysilicon layer and land on the thermal oxide layer. This was achieved using a DRIE (deep reactive ion etching) recipe. The scalloping of the sides of the coupler and waveguide caused by DRIE etching could result in a high optical loss. Therefore, a very short etch duration per cycle was used to ensure sub-wavelength scallops at the sides of the taper. A scallop size, i.e. the etch depth per cycle, of less than $\lambda_{min}/20$~130 nm is expected to be small enough to ensure sufficient flatness of the sidewalls for this application. Figure 5.8 shows the schematic of the realized waveguide with the integrated coupler.

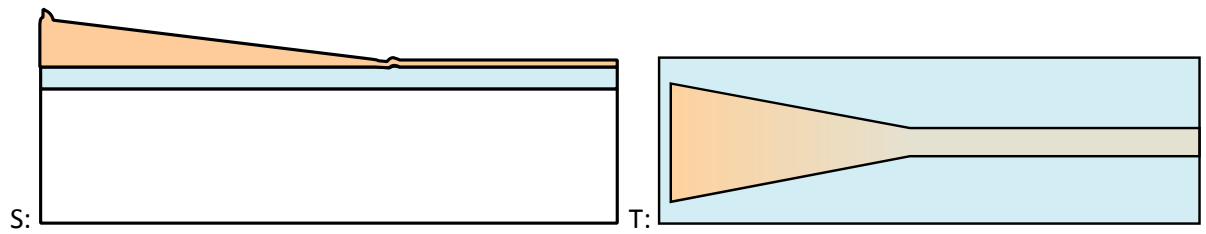

Figure 5.8 Patterning and etching of the coupler and waveguide structure

The next step in the fabrication of the waveguide sensor is the deposition of the cladding layer and patterning of the interaction window. PECVD SiO_2 is rather conformal and has a high deposition rate,

hence was selected as the cladding material. The thickness of this top cladding layer was selected as 1μm to obtain maximum confinement of the light within the covered length of the waveguide. Next, the layer is patterned with the interaction window design and etched in a BHF solution to selectively land on the polysilicon waveguide. A test wafer with PECVD oxide layer was used in the batch to obtain an accurate etch time using hydrophobicity test. Figure 5.9 shows the cross-section and top view of the realized structure.

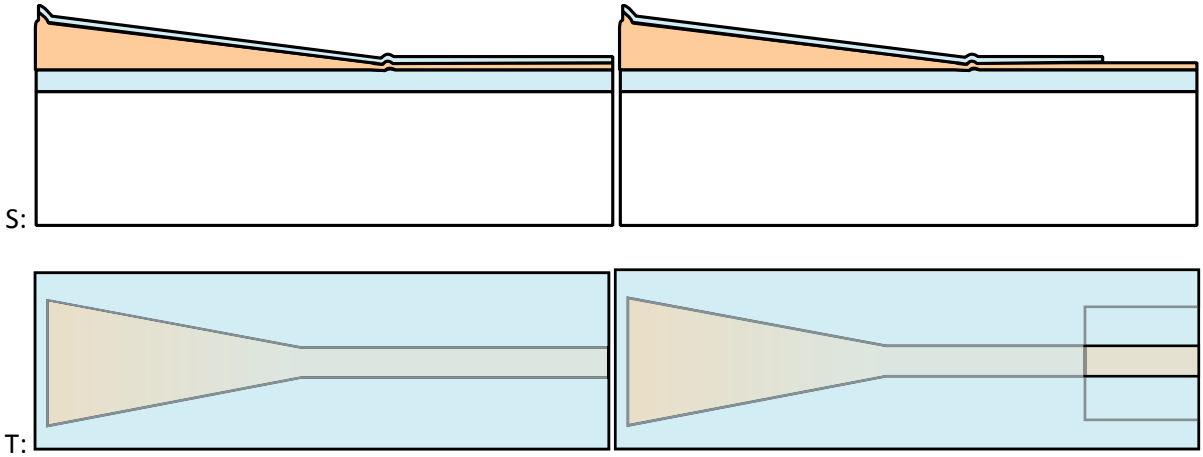

Figure 5.9 The realization of the top cladding and interaction window

The last step of the process is the realization of the grooves for installation of the fibers. The selected fiber has a cladding radius of 62.5μm thus a groove with the same depth must be etched into the silicon wafer such that the bottom of the fiber's core aligns with the bottom of the coupler. This was achieved in another spray coating of 4mm thick photoresist layer and selectively etching of the oxide cladding using RIE (reactive ion etching) and silicon wafer using DRIE. Figure 5.10 schematically shows the realized structure with the fiber placed in the groove.

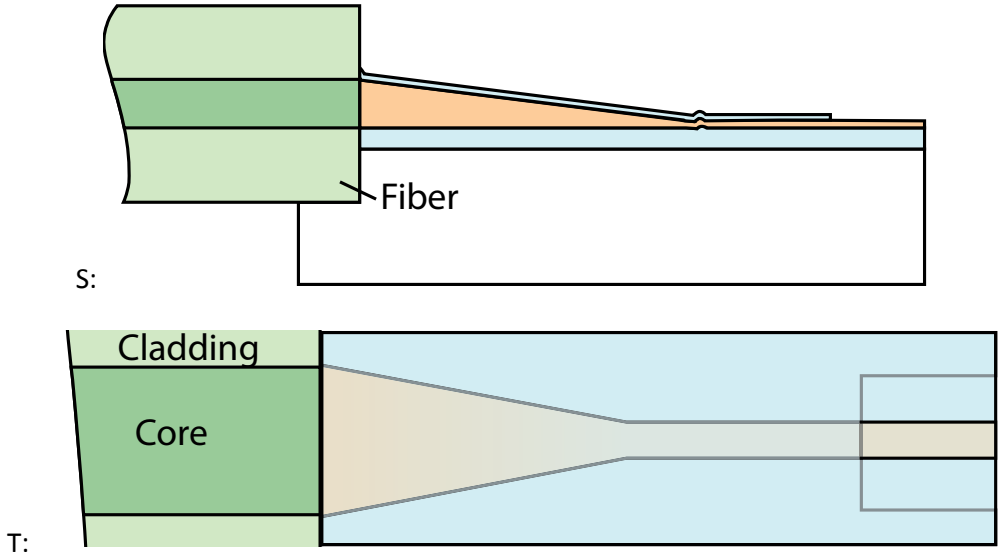

Figure 5.10 Schematics of the finalized device, with the fiber installed in the groove

After these fabrications steps, the devices with a very good quality are expected. The fabrication results are shown in the next section.

5.3 Fabrication Results

The chips after fabrication should be available at the middle of March. However, the machines in the Else Kooi Lab were down. And the chips' available time will be at 28th of March.

The delay for the chips has some irresistible reasons. And this cannot delay the thesis defense. The research will carry on after the chips are fabricated.

References

[1] B. C. Feng, "Resist reflow method for making submicron patterned resist masks," ed: Google Patents, 1977.

[2] M. Ghaderi *et al.*, "Design, fabrication and characterization of infrared LVOFs for measuring gas composition," *Journal of Micromechanics and Microengineering,* vol. 24, no. 8, p. 084001, 2014.

[3] A. Emadi, H. Wu, G. de Graaf, and R. Wolffenbuttel, "Design and implementation of a sub-nm resolution microspectrometer based on a Linear-Variable Optical Filter," *Optics express,* vol. 20, no. 1, pp. 489-507, 2012.

Chapter 6. Measurements

The fabrication process of the waveguide structure and the results were shown in Chapter 5.

After all the needed equipments were purchased, we can make our optical setups for the measurements. The whole setup for the measurements can be divided into three parts: light source, chip and detector. For the light source, we have several options: mid-infrared LEDs, mid-infrared laser or the light source in the VERTEX 70 machine, they will be explained later in this chapter. The LEDs and the laser are shown Figure 6.1.

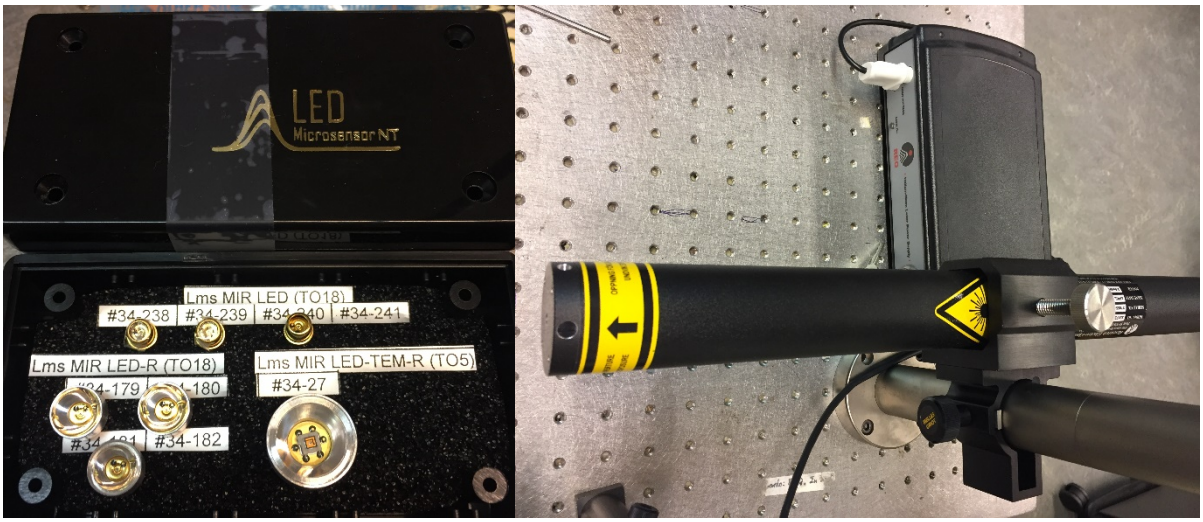

Figure 6.1 Mid-infrared LEDs and laser

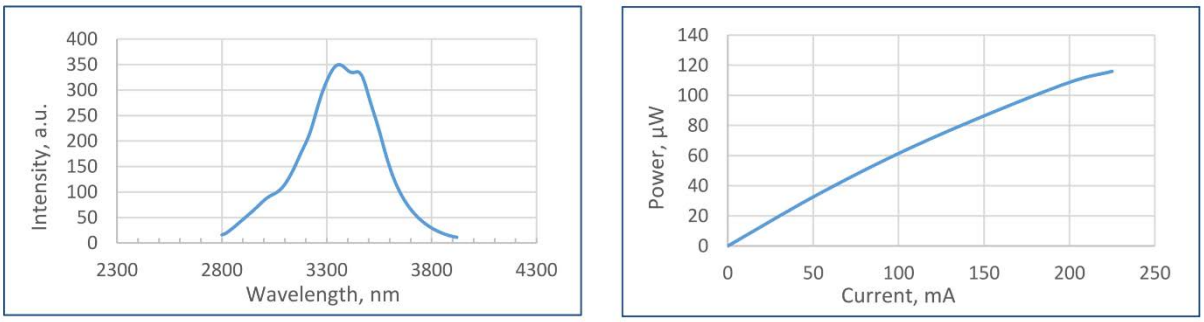

Figure 6.2 Light intensity and power for the LEDs

Figure 6.2 shows he wavelength information of the LEDs, these LEDs were bought from LED Microsensor NT. The wavelength centralizes at 3.4µm. The laser's wavelength is 3.392µm. These light source can be used in our application because we just want to test if the optical sensor is functional. Also at the wavelength of 3.4µm, there is a absorbance difference between water and ethanol as shown in Figure 2.6.

Another option is a high performance FT-IR spectrometers for demanding analytical and R&D application, it is one of the Bruker VERTEX Series as shown in Figure 6.3

Figure 6.3 VERTEX 70 spectrometers

For the detector, we currently have a light detector as shown in Figure 6.4. This detector has a detector array to sense the light and will turn the light signal to voltage signal. This voltage information can be transferred to a oscilloscope. Then the signal can be read.

Figure 6.4 Detector with gain options of 2 and 100

The ambient light is another interference for the detector. To solve this problem, we decided to use a chopper for the input light. The chopper can turn the input light into a cyclical optical signal and this will result a cyclical signal on the oscilloscope. Thus the optical signal which is caused by the light source will be distinguished from the ambient light. The chooper is shown in Figure 6.5, the hole on the left side of the plate is where the light comes through.

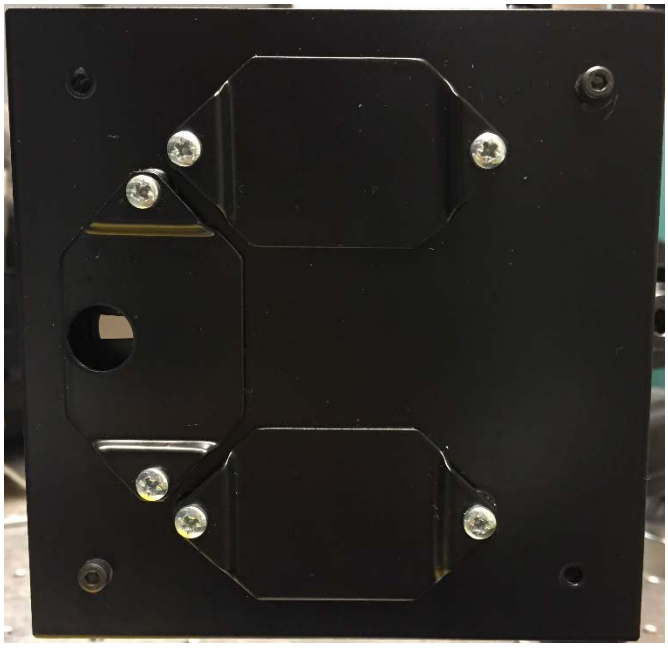

Figure 6.5 Infrared light chopper

This chopper's chopping frequency can be controlled by a controller, this controller is shown in

Figure 6.6 Chopping frequency controller

Also some lens used for focusing the light will be used in our application as shown in Figure 6.7. These lens are infrared light transparent. Some fiber holders will also be used as shown in Figure 6.8.

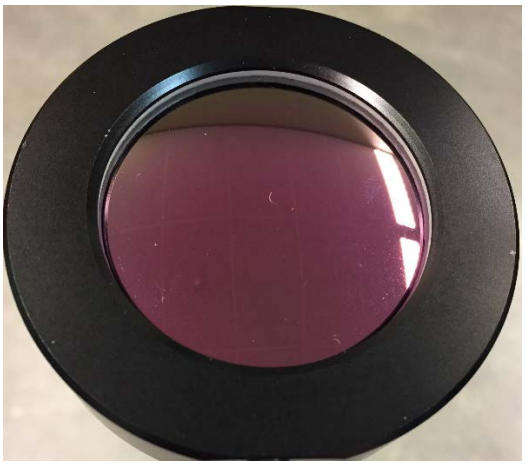

Figure 6.7 Infrared transparent lens

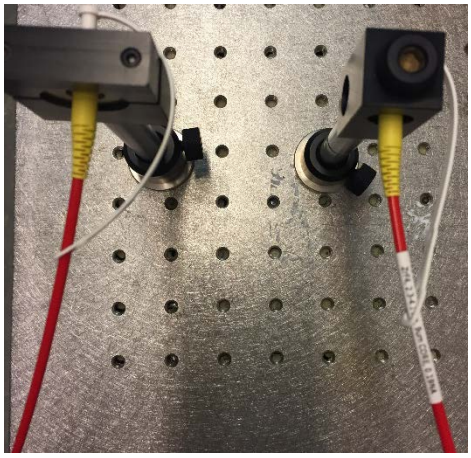

Figure 6.8 Mid-infrared fiber and fiber holders

For the chip itself, it will hold on a plate. This setup is similar with the one shown in Figure 6.9. In the middle of the picture, the chip is connected with the fibers without outer cladding at two ends.

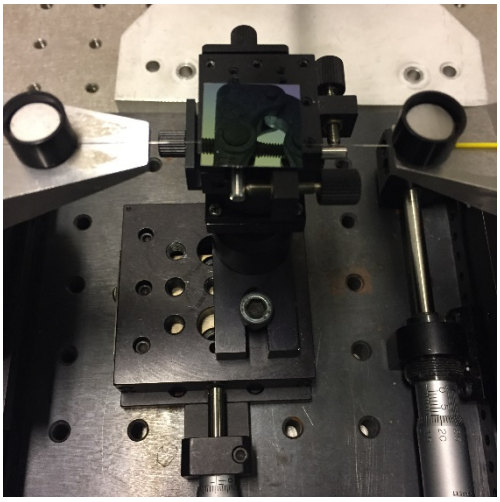

Figure 6.9 Chip holder and connected with fibers

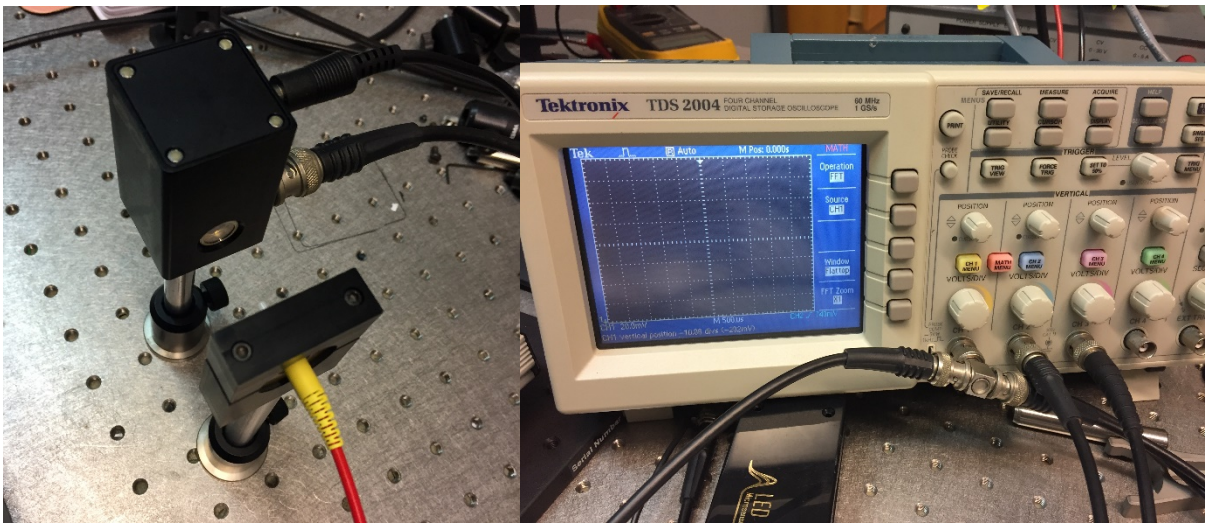

Figure 6.10 Setups for the output reading

The setups for the out put reading is shown in Figure 6.10, the end of the fiber is connected to the detector and the oscilloscope is connected with the detector. So we can directly read the signal from the oscilloscope.

We have several options for the optical input setup. One is to use the laser of wavelength of 3392nm as shown in Figure 6.11. The advantage of this setup is that the intensity of the light is as high as 1mW. Also the light is quite focused which means we do not have to do much optical calibration. But the disadvantage is very clear that the wavelength is as certain as 3392nm, and we can only observe the performance under this wavelength.

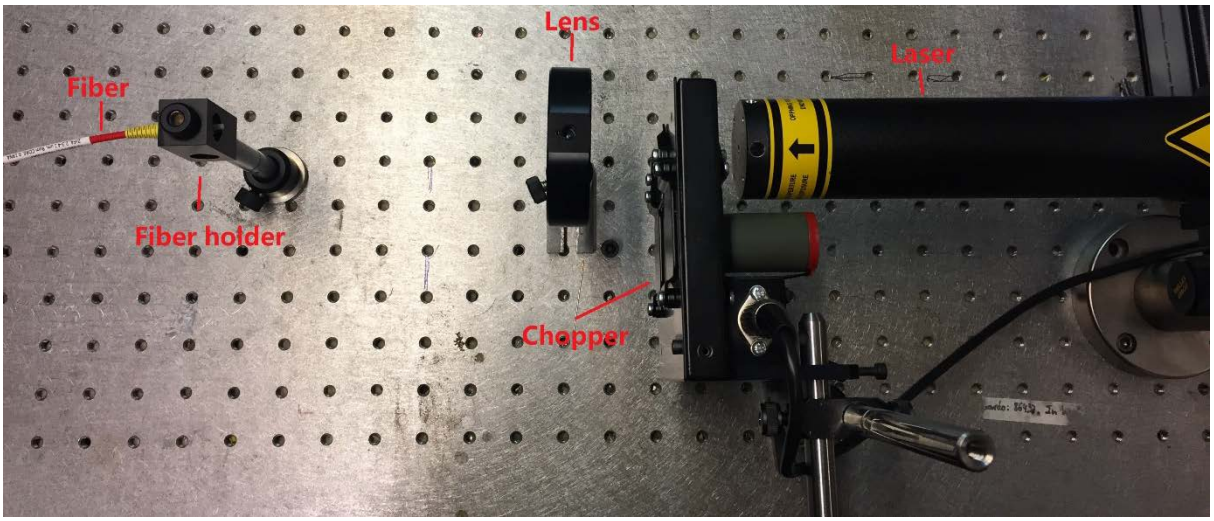

Figure 6.11 Laser optical input setup

The other method is to use the mid-infrared LED as light source. The input setup is shown in Figure 6.12. Two lens are needed here to build the setup because the light from LED is emanative. One lens is used to make the light to be parallel, and another one is focus the light. The chopper will be added into this setup if this setup do not perform well.

The advantage of the LED setup is that the light is not single wavelength. The band of the light includes the band of interests. However, the intensity of the light is quite low (on a micro-volt level) and a delicated optical calibration is needed..

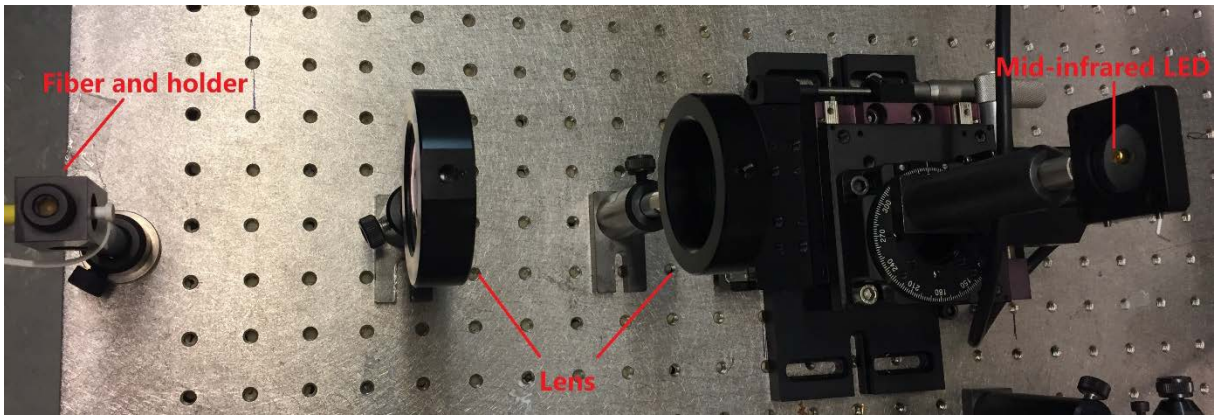

Figure 6.12 LED optical input setup

The last option for us is to use the FT-IR spectrometers. As shown in Figure 6.13, we can put the fibers at the two ends of the FT-IR spectrometers, and the fibers will be connected with the chip. The advantage of this setup is that the detector is integrated on this machine and the wavelength spectrum can be swept which means that the performance of the light can be seen by a matter of wavelength. However, the advantages are very obvious that a very delicated optical calibration is needed because the height and the place of the fiber is hard to adjust inside of this machine. Also the light intensity of the light source is quite low.

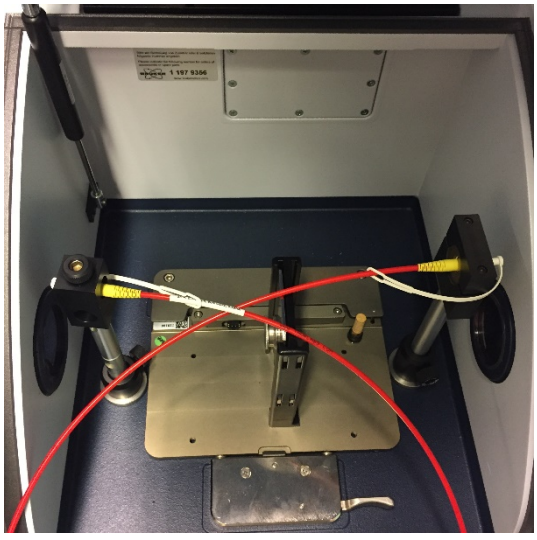

Figure 6.13 FT-IR spectrometers connected with fibers

As a conclusion, the laser is the most suitable light source in this application. And the measurements by using the laser should be carried on first.

Chapter 7. Conclusions and Future Work

7.1 Conclusions

In this thesis, a fuel sensor that is capable of determining the concentrations of the components of the water and ethanol has been presented. And the opration is based on mid-infrared spectroscopy.

The main design challenge is to make the light propagate well in the waveguide and the moding selecting property of the waveguide, and also the light mode converting. In reality how the light will be propagating is still uncertain, so several structures were designed on a single chip (including different taper lengths and different waveguide widths). However, from the simulation results, theoretically the devices are capable to give us the results that we want. And the sensor is capable to detect the concentrations of water and ethanol.

The main fabrication challenge is the taper. The edge bead at the end of the taper is inevitable by using our fabrication method. And also the surface of the waveguide and the taper is not extremely flat because of the DRIE etching method. How to reduce the influence of the edge bead and how to make the surface as flat as possible are the challenges of the fabrication.

7.2 Future Work

Improvements on the measurements and the measurements setup should be done in the future. All the structures and bands should be tested to verify the idea of optical spectroscopy. And also to combine with the UV sensor to detect the concentration of gasoline so that the ternary mixture problem can be solved.

In the future this sensor is possible to be applied on the issue of ethanol concentration monitoring during the ethanol production process. Because the target wavelength ranges are invisiable for the glucose.

Also a better coupling method has to be found in the future.